Adaptive Optics Telemetry

Estimation of turbulence parameters

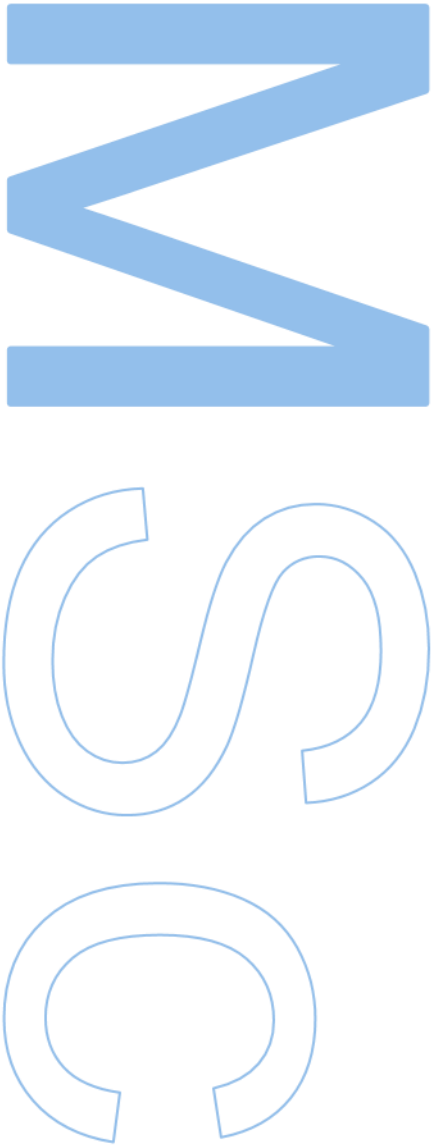

Nuno Morujão
Mestrado em Engenharia Física
Departamento de Física e Astronomia
2022

Supervisor
Prof. Paulo Garcia, Faculdade de Engenharia

Co-supervisor
Prof. Carlos Correia, Faculdade de Engenharia


U.PORTO
FEUP FACULDADE DE ENGENHARIA
UNIVERSIDADE DO PORTO


U.PORTO
FACULDADE DE CIÊNCIAS
UNIVERSIDADE DO PORTO

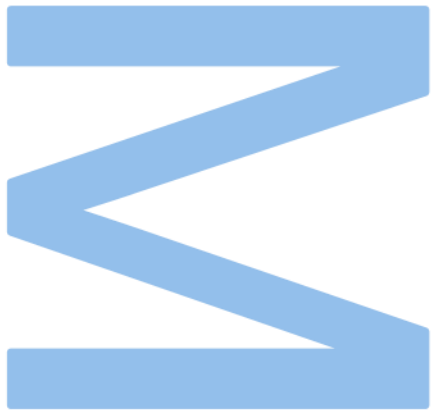

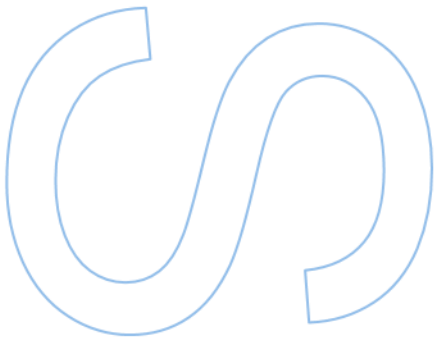

Sworn Statement

I, Nuno Miguel Cardoso Morujão, enrolled in the Master's Degree in Engineering Physics at the Faculty of Sciences of the University of Porto hereby declare, in accordance with the provisions of paragraph a) of Article 14 of the Code of Ethical Conduct of the University of Porto, that the content of this project reflects perspectives, research work and my own interpretations at the time of its submission.

By submitting this project, I also declare that it contains the results of my own research work and contributions that have not been previously submitted to this or any other institution.

I further declare that all references to other authors fully comply with the rules of attribution and are referenced in the text by citation and identified in the bibliographic references section. This project does not include any content whose reproduction is protected by copyright laws.

I am aware that the practice of plagiarism and self-plagiarism constitute a form of academic offense.

Nuno Miguel Cardoso Morujão

02/01/2023

Acknowledgements

Em primeiro lugar agradeço aos meus pais e irmãos pelo apoio incondicional durante toda os meus anos no ensino superior. Sem eles este documento nunca teria sido escrito.

Agradeço também aos meus orientadores, o Professor Paulo Garcia e o Doutor Carlos Correia, que me incentivaram a ser rigoroso na minha escrita e me ajudaram a explorar novas abordagens à tese. Agradeço à sua atitude acolhedora e a toda a gente que se juntou à nossa equipa de trabalho.

Agradeço em especial ao Paulo Andrade, que me ajudou sempre que tinha dúvidas e me explicou com paciência muitos dos conceitos que não percebia.

Agradeço também à equipa do sistema NAOMI por me fornecerem os dados de telemetria que permitiram este trabalho. Em especial agradeço ao Doutor Julien Woillez que se disponibilizou à avaliação desta tese dando feedback importante para criar a melhor versão da tese possível.

Finalmente agradeço aos meus amigos e a todos os que me ajudaram nesta etapa. Nada disto seria possível sem vocês!

UNIVERSIDADE DO PORTO

Abstract

Faculdade de Ciências da Universidade do Porto
Departamento de Física e Astronomia

MEng. Engineering Physics

Adaptive Optics Telemetry

by Nuno Morujão

The estimation of turbulence parameters is of importance to site characterisation, optimisation of adaptive optics systems and fringe trackers. The ubiquity of Shack-Hartmann wavefront sensors in modern observatories make them an ideal sensor for turbulence parameter estimation. We seek to estimate these turbulence parameters from wavefront sensor telemetry data produced from the adaptive optics system of the four Auxiliary Telescopes of the VLT, NAOMI. The low spacial resolution of this system (4×4 Shack-Hartmann wavefront sensor) makes it particularly challenging for this application.

In this dissertation we apply an iterative fitting algorithm to estimate turbulence parameters from adaptive optics telemetry data. The algorithm iteractively fits the Zernike polynomial variances to estimate the Fried parameter and the outer scale. It corrects for the measurement noise, aliasing and cross-talk present in the temporal variances of the modal coefficients. We formulate the algorithm as a χ^2 problem. We also propose a Monte Carlo method to calculate the uncertainty, providing confidence levels to our estimates.

Given the challenging nature of the NAOMI system, the algorithm was first validated, calibrated and optimised through the use of simulated data. It allowed us to define the ideal number of iterations, the minimum time horizon and the number of modes to be included in the fitted variances and cross-talk error estimation. After optimisation the algorithm was applied to a data sample of telemetry data from the NAOMI system collected from 2018 to 2020, containing a total of 36932 data samples. All results were compared to a reference (DIMM estimates).

Simulation results show that the Fried parameter converges for a (37 ± 5) s time horizon and that the χ^2 problem is convex. In simulation, using typical atmospheric conditions for

the Paranal Observatory, the optimised algorithm achieved sub-per cent precision in the estimation of the Fried parameter, showing the applicability of the algorithm in NAOMI telemetry data. On the other hand, without the correction of the measurement noise, aliasing and cross-talk provided by the algorithm the error in estimation of the Fried parameter was 5%. Study of the geometry of the wavefront sensor used in NAOMI showed the system to be insensitive to the outer scale, as such this parameter can't be fitted from the data generated from individual Auxiliary Telescopes.

On-sky data analysis showed a 1.2% uncertainty in the measurements. The noise estimation was analysed and found to be biased when compared to an estimation of the noise through auto-correlation of the data. Furthermore, an analysis of outlier seeing estimations found the defocus mode to still be affected by telescope vibrations. We found the DIMM and the algorithm estimates to have a correlation of 0.71, with our algorithm estimating $(12.35 \pm 0.04)\,\%$ smaller seeing conditions. The difference between seeing estimates was shown to increase with an increase of the wind speed. We found the seeing estimates between the four ATs to be the same, within the measurement uncertainty of $0.005\,''$. As such a rigorous analysis of the spacial distribution of the seeing wasn't possible. Finally we found seasonality in the seeing, with the seeing conditions worsening during Winter months, were the median seeing was $0.703\,''$, while the Summer months provided the best seeing conditions, with a median seeing of $0.584\,''$.

UNIVERSIDADE DO PORTO

Resumo

Faculdade de Ciências da Universidade do Porto

Departamento de Física e Astronomia

Mestrado Integrado em Engenharia Física

Telemetria de ótica adaptativa

por Nuno Morujão

A estimação de parâmetros de turbulência é de importância na caracterização de instalações, na optimização de sistema de ótica adaptativa e de *fringe trackers*. O uso ubíquo de sensores de frente onda de Shack-Hartmann tornam o o sensor ideal para a estimação de parâmetros de turbulência. Procuramos a estimação destes parâmetros a partir de dados de telemetria produzidos pelo sistema de ótica adaptativa dos Telescópios Auxiliares do VLT, NAOMI. A baixa resolução espacial do sistema (sensor de Shack-Hartmann 4×4) torna-o particularmente desafiante para esta aplicação.

Nesta dissertação aplicamos um algoritmo de ajuste iterativo para estimar os parâmetros de turbulência a partir de dados de telemetria produzidos a partir de sistemas de ótica adaptativa. O algoritmo ajusta iterativamente as variâncias dos polinómios de Zernike para estimar o parâmetro de Fried e a escala externa. O algoritmo corrige ruído de medição, *aliasing* e *cross-talk* presentes nas variâncias temporais dos coeficientes modais. Formulamos o algoritmo como um problema de χ^2. Finalmente propusemos um método de Monte Carlos para o calculo das incertezas, dando intervalos de confiança às nossas medições.

Dado a natureza desafiante do sistema NAOMI, o algoritmo foi primeiro validado, calibrado e optimizado a partir de dados de simulação. O que nos permitiu definir o número ideal de iterações, o horizonte temporal mínimo e o número de modos a incluir no ajuste de variâncias e na estimação de *cross-talk*.

Após a optimização o algoritmo foi aplicado a uma amostra de 36932 dados de telemetria gerados pelo NAOMI em operações que englobam os anos de 2018 a 2020. Todos os resultados foram comparados com estimativas de referência (estimativas de DIMM)

Resultados da simulação mostram que o parâmetro de Fried converge para horizontes temporais de $(37 \pm 5)\,\mathrm{s}$ e que o problem de χ^2 é convexo. A partir de simulações de

condições típicas do Observatório do Paranal o algoritmo optimizado alcançou estimativas com precisão inferior a 1%, indicando a aplicabilidade deste algoritmo em dados de telemetria do NAOMI. Por outro lado, sem a correção das componentes de erro a estimativa feito pelo algoritmo teve um erro de 5%. Estudos da geometria do sensor de frente de onda usado no NAOMI revelaram que o sistema é insensível à escala externa e como tal este parâmetro não pode ser estimado pelo algoritmo usando apenas os dados de um único Telescópio Auxiliar.

A análise de dados reais deu-nos uma incerteza do algoritmo de 1.2% nas medições. A estimativa do ruído foi analisada e encontram enviesamento quando comparado a uma estimação do ruído a partir de auto-correlação temporal. Para além disso, uma análise de pontos anómalos mostrou que o modo de defocus ainda é afetado pelas vibrações do telescópio. As estimações do algoritmo e do DIMM têm correlação de 0.71, com o antecedente a estimar condições de *seeing* $(12.35 \pm 0.04)\,\%$ inferiores ao DIMM. A diferença entre as estimativas de *seeing* aumentou com o aumento da velocidade do vento. Em último lugar a análise das estimativas dos 4 ATs mostrou que as suas estimativas de *seeing* foram iguais, dentro do intervalo de incerteza de $0.005''$. Como tal uma análise rigorosa da distribuição espacial do *seeing* não foi possível. A sazonalidade do *seeing* também foi verificada, tendo o mesmo deteriorado nos meses de inverno, nos quais o *seeing* mediano foi de $0.703''$, enquanto que nos meses de verão as condições de *seeing* melhoraram, com um *seeing* mediano de $0.584''$.

Contents

List of Figures

Chapter 1

Introduction

1.1 Context

The Earth's atmosphere is widely understood as a turbulent fluid producing local variations in the temperature, density and velocity of the air. These changes are translated into fluctuations of the refractive index of the air. The change in refractive index causes distortions in the electric and magnetic field. In strong turbulence we see fluctuation in both amplitude and phase of the electric field, leading to changes in the direction of the wave, this results in effects such as scintillation and blur. When the turbulence affects only the phase, we are in a low turbulence environment, this is the case for this work.

In the absence of atmospheric aberrations, the angular resolution of a point-source in the sky (e.g. a distant star) is given by the diffraction limit of of the telescope. The angular resolution of an object is then inversely proportional to the diameter (D) of the lens/mirror that observes it and directly dependent on the wavelength of the light (λ). The angular resolution will then be λ/D. The angular resolution is an important optical parameter that represents the angular distance between point-sources that the telescope can differentiate. The effect of the atmospheric aberrations depend on the lens/mirror diameter. For diameters larger than tens of centimetres, the effect is to limit the diameter of the point spread function, to a value that depends on the turbulence and not on the telescope diameter.

The distortion to the wave can be computed by making use of the turbulence parameters of an underlying turbulence model. These parameters are independent of the telescope and vary across the atmosphere, which can be stratified into a set of layers. For large telescope mirrors the angular resolution is dictated by the Fried parameter (r_0) and outer scale ($\mathcal{L}_0$).

On good observing sites the coherence length of the turbulence (the Fried parameter) is of the order of 10-20 cm at visible wavelengths. The resolution of larger apertures is reduced to this coherence length. The same concept is normally expressed through the seeing. The seeing directly corresponds to the angular resolution, opposed to a length. It's inversely proportional to the Fried parameter and directly proportional to the wavelength and it is usually in the range of 0.5-1.2 arc seconds. A large telescope is then limited in angular resolution. The outer scale serves as a saturation parameter of the turbulence effects expressed by the coherence length. This effect only becomes noticeable when we are outside of the inertial range of the turbulence (the outer scale typically varies between 10-100 m).

The atmosphere changes randomly with time and across space. As such a statistical approach is taken in the treatment of atmospheric effects. On account of its intrinsic randomness, descriptive models are statistical in nature where such concepts as statistical moments, (co-)variance and structure functions are used. The distortion effects are not affected by direction and orientation of the electric field (i.e. isotropic). Additionally, the variance of these effects on the electric field is assumed to not be locally dependent on their absolute position and time (i.e. stationary). The separation of two points in the atmosphere is sufficient to describe the distortion of the phase once the turbulence parameters are known.

Typically the effects of the distortion of the phase in Earth-based telescopes are corrected through the use of an adaptive optics (AO) system. The distorted wave is sensed and corrected. The system acts as a negative feedback control loop and the real-time signals can be used to generate telemetry data. The telemetry data contains information on the phase sensed by the wavefront sensor. It also has information on the deformable mirror configuration used to correct the electric field phase. If this data is generated we can post-process it in order to evaluate the turbulence parameters. The telemetry data is obtained from long data-sets of short exposures, allowing the study of the temporal variance of the phase.

The temporal variances are then obtain by undoing the control loop, which allows us to obtain the pseudo open loop modes. The pseudo open loop modes are used to reconstruct the variance of the modes. Several effects impede a perfect reconstruction of the modal coefficients. Noise in the measurement affects the variance of the results. Aliasing can be seen due to the finite number of samples collected by the sensor. When using the

Shack-Hartmann wavefront sensor to track the atmosphere there is also the introduction of cross-talk effects into the measurement.

In order to estimate the turbulence parameters we use an algorithm to fit the temporal variance of the reconstructed modal coefficients. By comparing their variance to the one expected from turbulence models a fit can be performed by minimising the difference between the two.

Since noise, aliasing and cross-talk affect the variances, our algorithm uses special profiling techniques to estimate these contributions and remove them from the variances. Since knowledge of the turbulence parameters is needed for the cross-talk estimation, an iterative approach is taken.

1.2 Research Goals

Previously an iterative algorithm for the estimation of turbulence parameters has been developed and applied solely to simulation data (Andrade et al., 2019). As such its application to on-sky data is the next logical way to validate the algorithm. This is done through the application of the estimation algorithm to telemetry data generated from the new adaptive optics module of the Very Large Telescope Interferometer (VLTI), NAOMI.

Due to being a low order system (4×4 Shack-Hartmann wavefront sensor), NAOMI provides a challenging scenario for the estimation algorithm. Due to the sensor architecture we have a mixing of cross-talk effects with aliasing, with only low order variances being available for the fit. These two additional complications will affect the estimation of the turbulence parameters and their effect on the estimation is not yet understood, not having been assessed by previous research.

A methodological optimisation of the algorithm is of interest to answer an open set of questions:

- can the algorithm be optimised for low-order systems?
- can the turbulence parameters be estimated from generated data?
- if estimation is possible, what is the ideal number of iterations of the algorithm?
- what is the minimum time horizon needed for the estimation of turbulence parameters?

- what is the optimum number of modes to be included in the fit and cross-talk estimation?

The study of real telemetry data allows us to estimate the turbulence parameters seen in the Paranal Observatory. More concretely it can help us answer:

- what's the performance of the algorithm in the estimation of the turbulence parameters for real data;
- what's the distribution of the seeing across the mountain;
- what's the temporal evolution of the seeing;
- what are the effects of wind-speed on the seeing estimation;
- how does the algorithm compare with currently employed seeing trackers;
- what is the outer scale at Paranal;

1.3 Document Structure

In this chapter we gave a brief motivation and context to the work developed in this dissertation, its research goals and the structure of the document. In the State of the art chapter a literature revision of current research in turbulence parameters estimation is performed. In this chapter the base concepts of turbulence are also discussed. The Methods chapter presents some of the theoretical models used in adaptive optics and the algorithm developed for the estimation of turbulence parameters in this thesis. In the NAOMI system chapter we introduce the NAOMI system itself and optimise the algorithm parameters through the use of a simulation pipeline. In the Results chapter we analyse and discuss the estimations performed by our algorithm when applied to real telemetry data. In this chapter we also discuss both how the telemetry data was curated and how the algorithm compares to reference estimations. Finally, we conclude our work with the key lessons learned in the development of this dissertation and recommend further avenues of exploration.

Chapter 2

State of the Art

We must first understand the causes, magnitude and behaviour of the atmosphere that contribute to the degradation of angular resolution in imaging systems before we correctly implement an adaptive optics system in a telescope. Therefore there is an increased need for the estimation of the turbulence parameters in the Paranal Observatory if future instruments hope to work at their projected angular resolution.

As such, during this chapter a brief overview of the origin of turbulence and the efforts to model these effects is included. Following an introduction to the models of turbulence currently in use a discussion of current turbulence profiling techniques is done in order to weave a full picture of the possible approaches to turbulence monitoring. Lastly we place focus on the estimation of turbulence parameters from adaptive optics telemetry data since it's the type of estimation method used in this work.

2.1 Atmospheric turbulence

2.1.1 Parametric models

In a viscous fluid, such as the atmosphere, once the viscosity of the medium is overshadowed by the velocity and dimension of the flow we see a rise in what is known as turbulent motion. This regime is characterised by a high Reynolds number ($10^5 - 10^6$), which is defined as a function of the viscosity, ν, flow speed, u, and characteristic flow length , L

$$\mathrm{Re} = \frac{uL}{\nu}. \tag{2.1}$$

In turbulent motion, random secondary flows, known as turbulent eddies, are present. Energy is transferred from large to small scale eddies in a cascade process. This process

results in inhomogeneities in the fluid that will cause temperature fluctuations and as a consequence a fluctuation in the refractive index of the medium, disturbing the phase and amplitude of the transmitted wavefront.

The Kolmogorov model of turbulence (Kolmogorov, 1941) serves as a descriptive model of the energy spectrum of turbulence and consequently provides a description of the fluctuation of the refractive index.

It's important to emphasise some key assumptions of the model. The assumed statistical homogeneity of the random velocity field implies that random fluctuations in the field depend only on their vector separation, thus being independent of their absolute position. The isotropic nature of the velocity field allows us to extend this independence to the direction of the vector. Thus the energy spectrum of the Kolmogorov model will depend solely on the magnitude of the separation of two points in the field.

The turbulence model will then describe the average phase difference between two points in space separated by a distance, ρ,

$$D_\phi(\rho, t) = \langle |\phi(\mathbf{r}, t) - \phi(\mathbf{r} + \rho, t)|^2 \rangle_\phi \tag{2.2}$$

$$D_\phi(\mathbf{r}, \tau) = \langle |\phi(\mathbf{r}, t) - \phi(\mathbf{r}, t + \tau)|^2 \rangle_\phi, \tag{2.3}$$

where ϕ represents the phase. Equation (2.2) and (2.3) describe the ensemble average of fluctuations of the field in respects to space and time respectively. These averages are known as the phase structure functions, D_ϕ. The statistical nature of the model is of note, as the instantaneous value of these quantities can't be accurately modelled.

A successor to the Kolmogorov model, the von Kármán model, presents expanded agreement between the observed, experimental, seeing and the one projected by the turbulence model (Tokovinin et al., 2007). Modern adaptive optics correction systems mainly use this widely tested model (Avila, 2021; Doelman, 2020; Andrade et al., 2019; Fétick et al., 2018) described by:

- the Fried parameter, r_0 - a coherence scale defined by the aperture diameter that contains an average of one radian root mean square phase aberration;
- the outer scale, $\mathcal{L}_0$ - an additional structure function saturation parameter that represents the outer boundary in which two points in space are spatially correlated;

These parameters in conjunction with the recording of various others such as the wind-speed and humidity can map the expected seeing conditions for an observatory. This can be used for both selecting sites of small seeing conditions, which in turn need smaller corrections, and the estimation of the operational necessities of present systems.

Strong turbulence affects both the phase and amplitude of the incoming wave. It is in the high turbulence regime that the scintillation phenomena is observed.

In the weak turbulence regime we can assume the amplitude to be static, while the phase fluctuates. Since the amplitude of the turbulence is fixed we don't consider changes in direction along the wavefront. It is in the context of weak turbulence that we assume our calculations to hold physical relevance. Our interest in the low turbulence domain drives us to depict and treat wavefront phase. The representation of the wavefront phase is presented in chapter 3.

2.1.2 Turbulence Parameters

2.1.2.1 The Seeing

The seeing reflects the effects of earth's atmosphere on the image of a point-like source. The seeing can be expressed as the angular size, α, of a point-like source. A simple equation relates the seeing with the Fried parameter (Fried, 1965)

$$\alpha = 0.976\frac{\lambda}{r_0}. \tag{2.4}$$

If the seeing is smaller than the diffraction limited image we can then say that the instrument is diffraction limited. This is common in small telescopes. Assuming the median seeing of the Paranal Observatory any telescope with a diameter smaller than 14 cm at a wavelength of 500 nm can be assumed to be diffraction limited as

$$\frac{\lambda}{D} > 0.976\frac{\lambda}{r_0}, \tag{2.5}$$

For any larger telescope we can use the seeing to reflect the observational conditions of a point-like source in the sky.

Equation (2.4) follows the Kolmogorov model and is used by the DIMM. However, studies by Martinez et al. (Martinez et al., 2010) showed that the seeing estimation can be further improved by incorporating the outer scale

$$\alpha_{vK} \approx \alpha\sqrt{1 - 2.183(r_0/L_0)^{0.356}}. \tag{2.6}$$

However, we chose to utilise equation (2.4) in seeing estimates. As our results are compared to the DIMM in the real data analysis section and that system utilises the former convention. Additionally, the NAOMI system will be shown to be insensitive to the outer scale in chapter 4, as such we can't apply equation (2.6).

2.1.2.2 The Fried Parameter

The Fried parameter (Fried, 1965), r_o, is commonly referred to as a coherence length. Over a circular aperture of diameter, D, the Fried parameter will inform us of the mean square wavefront phase distortion through

$$\sigma^2 = 1.03(D/r_0)^{5/3}. \tag{2.7}$$

This parameter is thus a characteristic parameter that specifies the separation at which there exists, on average, one radian of root mean square phase aberration. It characterises the effect of the seeing in the wavefront distortion at a given wavelength

$$r_0 = \left[0.423k^2(\cos\gamma)^{-1}\int_0^\infty C_n^2(h)dh\right]^{-\frac{3}{5}} \propto k^2\int_0^\infty C_n^2(h)dh, \tag{2.8}$$

where the r_0 is both a function of the wave number ($k = 2\pi/\lambda$), the angular distance of the source from the zenith (γ) and the index structure coefficient, C_n. This coefficient is measured along the atmosphere, represented through the integration across h, which itself corresponds to the height from the observatory to the layer of the atmosphere we are observing. A layer will correspond to a bounded vertical region of the atmosphere, at a particular height, h, in which it's assumed that the turbulence parameters are constant. These layers are visible in Figure 2.1 where C_n^2 is represented as a function of the height. $(\cos\gamma)^{-1}$ is known as the air mass and the standard wavelength is 500 nm for the presentation of atmospheric parameters, corresponding to the visible wavelength.

On a practical aspect, we cannot differentiate between layers at different heights when we estimate the Fried parameter from adaptive optics telemetry data generated from Shack-Hartmann sensors.

The Fried parameter is a widely tracked parameter. For the Paranal Observatory we see variations between 8-20 cm, with a median Fried parameter of 14 cm (Figure 2.2). Since

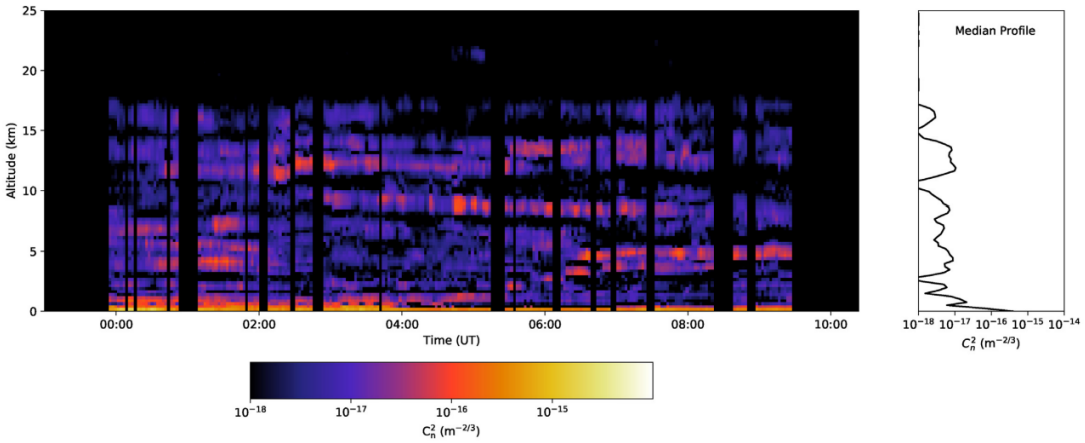

Figure 2.1: Stratified profile of the atmospheric turbulence extracted from (Osborn et al., 2018).

the data analysed in this work comes from the Very Large Telescope Auxiliary Telescopes, present at the Observatory, this provides values that we will later expect in its estimation.

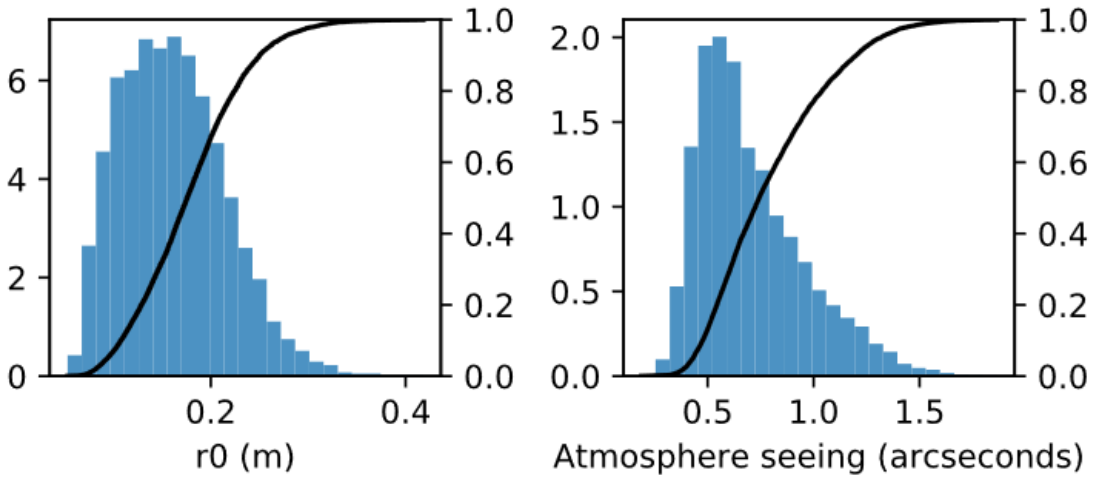

Figure 2.2: Distribution of the Fried parameter and seeing for the Paranal Observatory. Extracted from Osborn et al. (2018)

2.1.2.3 The outer scale

The Kolmogorov model is valid only in the inertial range of turbulence. The outer scale, $\mathcal{L}_0$, is added to the modelisation as a way to correct for discrepancies between the expected structure function and the one predicted from the Kolmogorov model. In that respect it serves as a saturation term when the separation increases beyond the outer scale. Additionally, a finite outer scale bounds the energy of the Kolmogorov model, which has infinite energy.

As is seen in Figure 2.3 this parameter can vary from one to hundreds of meters. It can be largely ignored when separation of two points in the atmosphere is smaller. However, when we approach a distance of the order of the outer scale we see a significant difference between models. This can be observed in the refractive-index structure functions of Figure 2.4 when the distance between two points nears the outer scale.

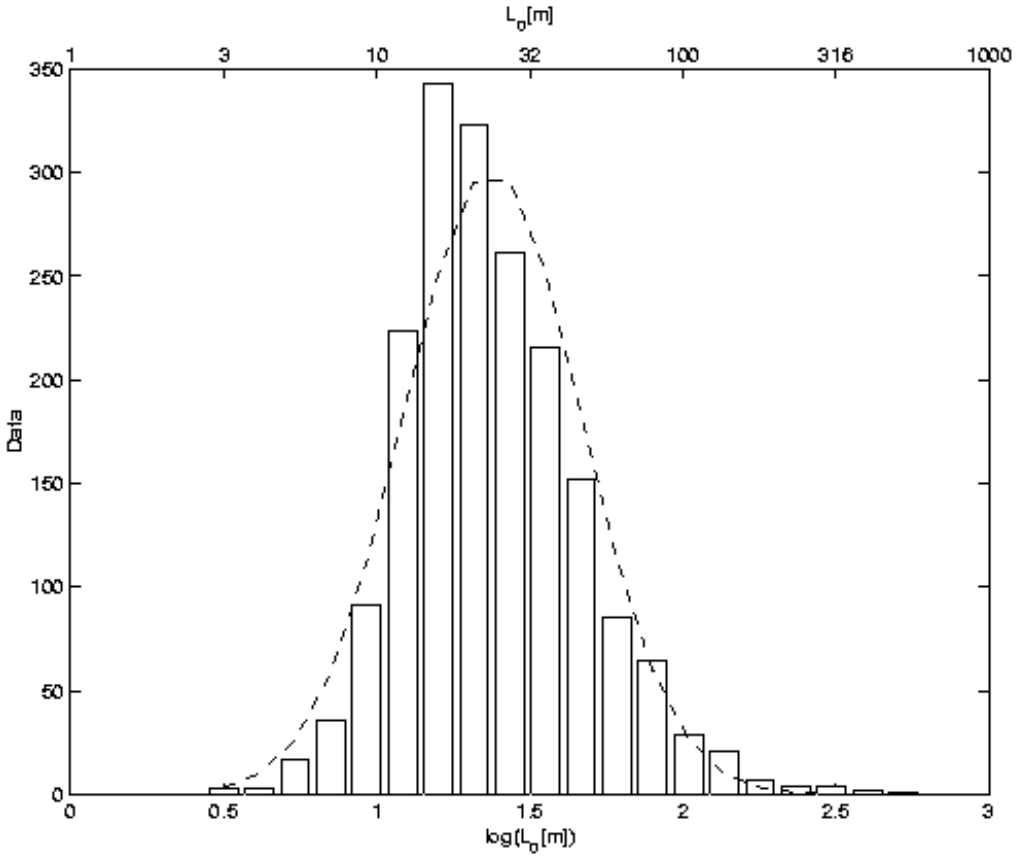

FIGURE 2.3: Outer scale values for the GSM at the Paranal Observatory. Extracted from (Martin et al., 2000)

This difference at larger diameters shows its relevance for the new generation of telescopes. As the maximum distance between two points in a telescope will correspond to its diameter we can estimate the difference between the models. Exemplifying, the factor between the diameter of the future ELT (D = 39m) and the outer scale is in the the order of the unity, showing a great disparity between von Kármán and Kolmogorov model. This

points to an increased need for the inclusion of this additional turbulence parameter in future site testing.

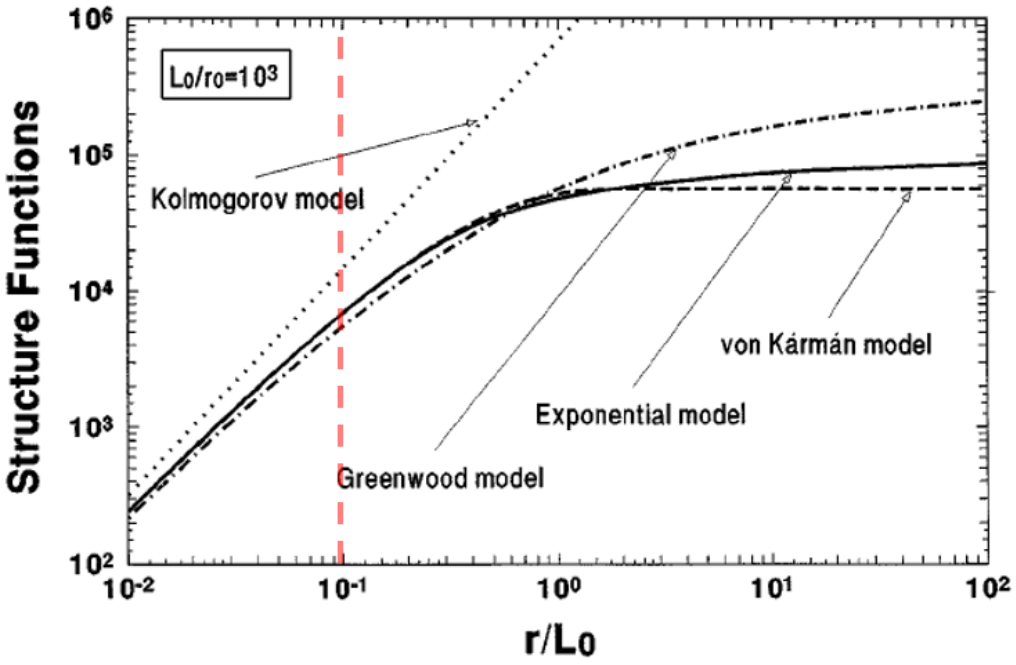

Figure 2.4: Structure function of the von Kármán distribution. L_0 represents the outer scale and r_0 represents the Fried parameter. As the distance between two points in the atmosphere (r in the graph) increases, the projected difference between the structure function of the von Kármán and Kolmogorov model also increases, as the separation goes beyond the inertial range and becomes equal to or greater then the outer scale. Extracted from Voitsekhovich (1995)

2.1.2.4 Coherence time, τ_0

Evaluating the error associated with this time delay, τ,

$$\sigma_t^2(\tau) = 6.88(\bar{v}\tau/r_0)^{5/3}, \tag{2.9}$$

where $\bar{v}$ represents the average wind speed. The coherence time then denotes the minimum time delay acceptable for the control loop. To achieve a radian rms error smaller than 1 radian we must impose

$$\tau_0 = (6.88)^{-3/5}\frac{r_0}{\bar{v}}. \tag{2.10}$$

Typical values of this quantity are of the order of milliseconds, for visible wavelength.

2.2 Turbulence parameter estimation techniques

The Fried parameter and the outer scale are needed in order for a complete description of the von Kármán model. Several techniques are discussed in the following section for the determination of turbulence parameters.

In order to broaden the spectrum of techniques discussed, we will present two types of techniques:

1. Integral parameter techniques: measure the turbulence parameters through integration of the full atmospheric contributions;

2. Profile parameter techniques: describe the index structure coefficient, $C_n^2(h)$, permitting the stratification of the atmosphere, given in the integral term of equation (2.8);

2.2.1 The Differential Image Motion Monitor (DIMM)

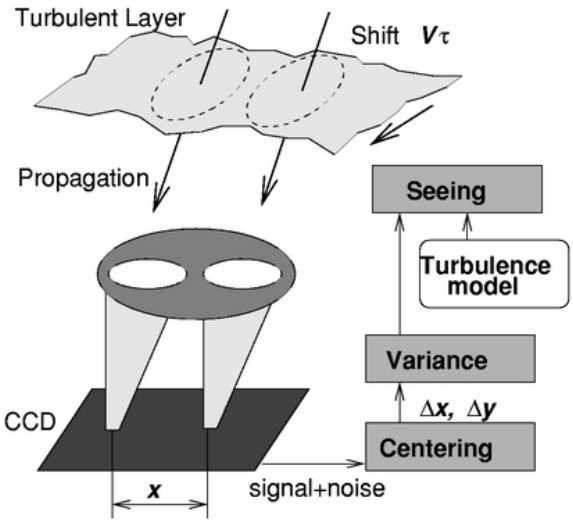

FIGURE 2.5: DIMM schematic Extracted from (Tokovinin, 2002)

A DIMM system is composed from a masked telescope mirror with two sub-apertures that monitor the seeing through the measurement of the image in each sub-aperture (Figure 2.5). The difference between these two images is known as the differential image motion, d. The two images will move inside their sub-aperture as the atmosphere evolves, leaving the trackers to record the shift in the x and y direction. Since both sub-apertures of the DIMM are mounted in the same lens the system is robust and largely immune to shake and tracking errors.

Through the use of temporal variances of the displacements a fit to the turbulence model can be obtained. This results in a prediction of the seeing from the estimated turbulence parameters associated with the model.

The Fried parameter is estimated as a function of the variance of the differential image motion, σ_d^2, at a particular wavelength, λ, through (Roddier, 1999)

$$r_0^{-5/3} = C \frac{\sigma_d^2}{\lambda^2 D^{-1/3}}, \tag{2.11}$$

where C is a numerical constant that depends on the ratio of aperture separation to their diameter, D. One interesting result of this relation is the achromatic nature of the differential image motion. The Fried parameter term in the equation is proportional to the inverse square of the wavelength, thus cancelling the contributions of wavelength (Tokovinin, 2002).

The turbulence estimations of the current DIMM at Paranal are limited to the Fried parameter as the system is insensitive to the outer scale parameter. Consequently it suffers from over estimations of the seeing for large diameter telescopes (Voitsekhovich, 1995). Additionally the DIMM doesn't provide a stratified index structure coefficient, as the system averages over the entire atmospheric contributions.

Present at the Paranal Observatory, coupled with a MASS system (described in the next section), the DIMM has long been running and as such acts as a comparative term for any other Fried parameter estimates. Our data is recent (the oldest data being from 2018), as such all our DIMM comparative estimates come from the new DIMM site. Installed in 2016 at the top of a 7 meter tower located to the North of UT4, it provides more accurate measurements of the seeing when compared to the old version, due to the removal of the back flow contributions seen in the old site. The telescope in which this new DIMM was installed has a diameter of 0.28 meters (Southern et al., 2015).

The system itself is still in common use for site testing and seeing monitoring (Tillayev et al., 2021; Liu et al., 2020; Masciadri et al., 2014).

2.2.2 Multi Aperture Scintillation Sensor - MASS

Strong turbulence leads to fluctuations in the refractive index of the air, which distort the phase of the wavefront. If the distortion is large enough they result in interference effects as the wavefront propagates through the atmosphere, resulting in fluctuations of the amplitude of the wavefront (Little, 1951; Roy and Clarke, 1977; Dravins et al., 1997).

The spacial scale of the scintillation phenomena speckle is of the order of $\sqrt{z\lambda}$ (maximum radius of the first Fresnel zone at a distance z). The distance directly relates to the altitude of the atmosphere we are probing (Roddier, 1981). Isolation of these altitudes can be achieved by the use of filters. This is done through the use of different disks of different aperture, as they reflect a differing diameter, D. Through an overlapping of disks, each with a different radius, we can obtain a discrete altitude profile of the scintillation.

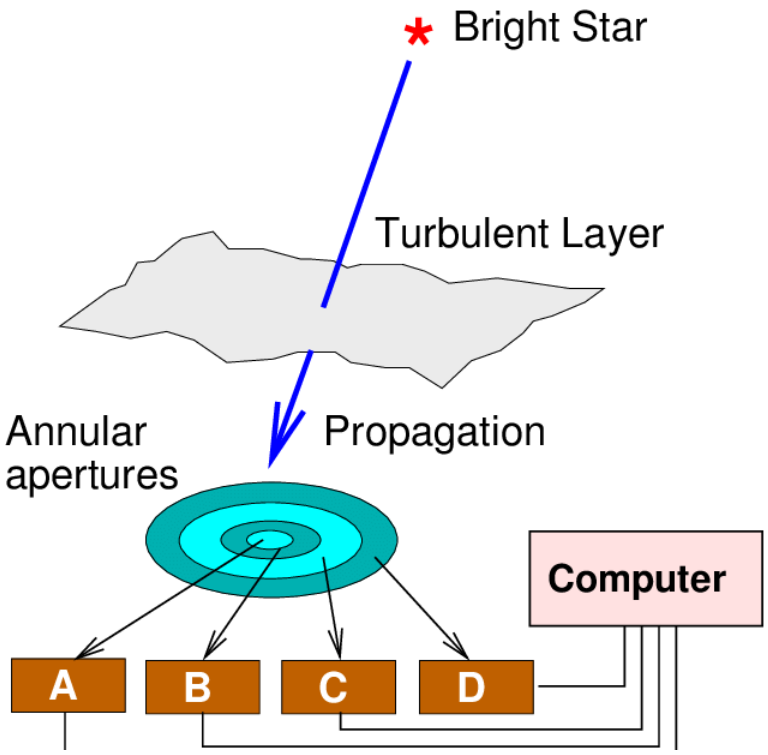

FIGURE 2.6: MASS working principle. Extracted from (Tokovinin, 2007)

The scintillation can then be associated with the turbulence profile through the use of differential scintillation between 2 different disks. The number of layers reached will then be limited by the number of apertures we are testing (typically 7 layers), these can be used to probe the high atmosphere, up to 16 km (Kornilov et al., 2007). Figure 2.6 represents the working principle of the system, in this implementation, the disks are overlapped and the measurements are differential.

A common application of the MASS is its coupling with the DIMM system at the inner aperture, in what is known as a MASS-DIMM system. This provides the improvement of the DIMM system since it is an integral system and doesn't provide a turbulence profile, which is increasingly needed for a correct monitoring and assessment of the atmospheric conditions, allowing for the monitoring of the ground atmosphere that is unavailable to the MASS system (Ogane et al., 2021; Lyman et al., 2020).

Future implementations of the MASS system are going to be able to monitor the ground-layer through the use of low-noise solid-state detectors, in what is known as a FASS (Full Aperture Scintillation Sensor) (Guesalaga et al., 2021), resulting in better layer resolution and a full profile of the atmosphere.

2.2.3 Balloon borne profilers

Balloon borne profilers are equipped with multiple sensors in order to delineate temperature, humidity, wind-speed and wind direction maps *in situ*. Through conversion mechanisms, the height profile of the structure constant of the temperature can be converted into the refractive index structure constant, C_n^2, through the additional height profile of pressure, $P(h)$, and temperature, $T(h)$

$$C_n^2 = \left(79 \times 10^{-6} \frac{P(h)}{T(h)^2}\right)^2 C_T^2(r,h), \tag{2.12}$$

where C_T^2 represents the temperature structure constant. From the measured refractive index constant profile one can obtain the Fried parameter, coherence time and through the coupling of the wind-speed profile one can also obtain the average wind velocity of the turbulence (Rogatto et al., 1993).

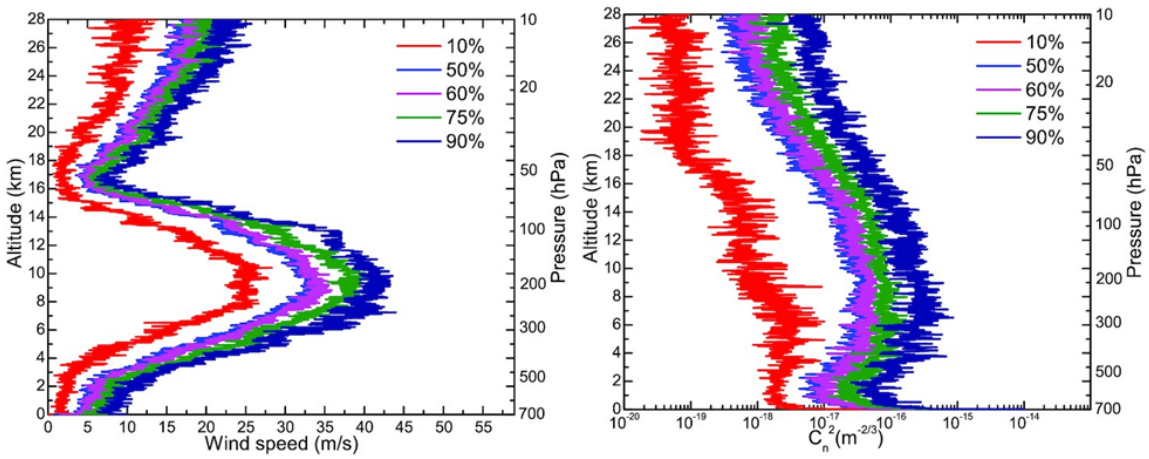

(a) Probability distribution of wind speed profiles.

(b) Probability distribution of $C_n^2(h)$ profiles.

Figure 2.7: Index structure measurements from the site testing campaign at the Tibetan Plateau. Extracted from (Qing et al., 2021)

Contrary to the DIMM technique, the balloon borne profiles give us insight into the distribution of the structure index above the observatory, as is seen in Figure 2.7.

This technique suffers from drift, as an ascending balloon can take 85 minutes to probe up to 25 km of atmosphere. This leads to lateral movement due to wind-sheers and a profile that doesn't trace a line between the zenith and observatory (Osborn et al., 2017).

2.2.4 The Lunar Scintillometer (LuSci)

Weak scintillation of extended bodies, such as the Moon, is mostly produced in the surface layer atmosphere (Seykora, 1993) and as such allows the probing of low atmosphere turbulence profiles (up to 100's of m) (Tokovinin et al., 2010).

A lunar scintillometer consists of an array of six small photondiodes that monitor the fluctuations in intensity of the light reflected by the Moon. Figure 2.8 illustrates the working principle. The six photodiodes track the changes in intensity of the light reflected by the moon, I_i, in a linear configuration. At a close distance the light cones don't overlap, remaining uncorrelated. At larger distances the cones overlap, resulting in a shared turbulence contribution and correlated signals. Considering pairs of photodiodes their covariance is calculated through

$$B_{i,j} = \frac{1}{K}\sum_{k=1}^{K}(\xi_i\xi_j)_k, \tag{2.13}$$

where K is the number of samples collected during the accumulation time and $\xi_i = I_i/\langle I_i\rangle - 1$ is the normalised photo-current measured in the various sensors.

From the calculated covariances between diodes a correspondence is drawn with the structure profile which can be used to provide information on the seeing

$$B(\mathbf{r}) = \int_0^\infty dz W(\mathbf{r}, z) C_n^2(z), \tag{2.14}$$

where $W(\mathbf{r}, z)$ is a weighting function adapted to the instrument and $\mathbf{r}$ corresponds to the transverse coordinates spanning the moon.

It is well suited for site testing and calibration of different monitoring systems, without the need for large towers that might add to the surface layer turbulence in excellent seeing condition sites (Hickson et al., 2020; Surendran et al., 2018). It is however not ideal for long surface atmosphere tracking, as the moon needs to be visible above the horizon and as such cannot be utilised constantly.

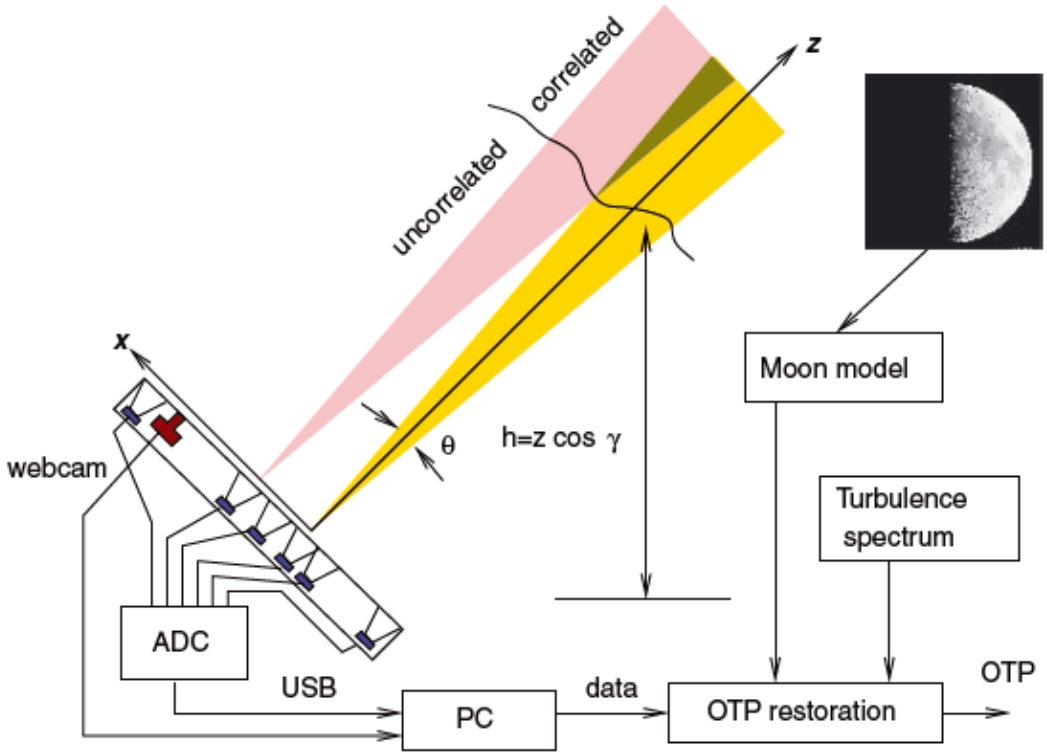

Figure 2.8: The Lunar Scintillometer working principle. Extracted from (Tokovinin et al., 2010)

2.2.5 Slope Detection and Ranging (SLODAR)

SLODAR and SL-SLODAR (surface layer monitoring dedicated system) operates from the study of cross-correlation of overlapped wavefronts, resulting from the monitoring of binary star systems.

A binary star with angular separation θ is observed by the Shack-Hartmann wavefront sensor (discussed later in this Chapter), which measures slopes. These slopes are used to reconstruct the incoming wavefront. As can be seen in Figure 2.9 an atmospheric layer at altitude h produced shifted copies of the aberrated wavefront at the ground where the separation of the copies, S, is given by

$$S = h\theta. \tag{2.15}$$

When spacial cross-correlation of these two copies is performed, there will be a peak in S. This allows for the probing of different altitudes, as the cross-correlation peaks correspond to the height in the atmosphere, h. Since the sensors possess a lenslet array

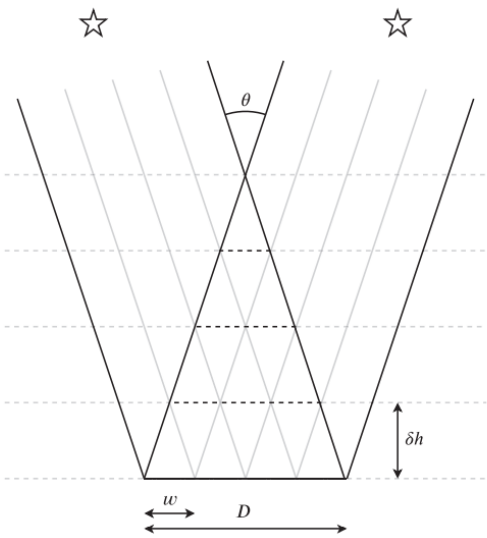

FIGURE 2.9: Shared turbulence patches between two stars observed by a SH sensor with lenslets of diameter w. As the angular distance between the stars increases, the resolution of the technique increases. The highest probed altitude will decrease with the increase in angular resolution. Extracted from (Butterley et al., 2020).

we can think of the sensor as a multiple subaperture sensor, where each lenslet acts as an individual imaging system. Each lenslet possesses a characteristic diameter, d, that will dictate the vertical resolution of the system (Butterley et al., 2020)

$$\delta h = \frac{d}{\theta}. \tag{2.16}$$

For N lenslet sensor we will obtain a resolution of N atmospheric layers that can be measured, it's then an important parameter for the resolution of the system.

The maximum achieved altitude will also increased with the proximity in stars, θ. As such, for a surface layer monitoring system the distance between stars is increased (close to the 10 arcmin range) while a regular SLODAR set-up utilises separations in the order of 1 arcmin. As the separation between stars increases high turbulence layer contributions become decorrelated between the two cones of light, as there is no overlap. The maximum sampling altitude, h_{max}, is then given by

$$h_{max} = n_{\text{sub}} \frac{d}{\theta} \tag{2.17}$$

where n_{sub} is the number of subapertures in the sensor.

Calculation of the optical turbulence profile is done through deconvolution of the cross-correlation, C, between subapertures and auto-correlation of the individual subapertures

$$C_n^2(h) \propto F^{-1}[F(C)/F(A)], \tag{2.18}$$

where F is the Fourier transform operator (Laidlaw et al., 2020; Ono et al., 2017; Butterley et al., 2020).

2.2.6 Scintillation Detection and Ranging (SCIDAR)

Here the complete profile from 0-20 km (Tokovinin et al., 2005) is provided through the cross-correlation of scintillation between a binary system of bright stars through a single sensor, in what is known as a generalised SCIDAR. The working principle is close to that of the SLODAR, but unlike the SLODAR technique it utilises scintillation speckles in order to obtain cross-correlations. It should be noted that the resolution of the SCIDAR is superior to that of the SLODAR, as the Fresnel radius, $\sqrt{z\lambda}$, is much smaller than the smallest lenslets present in a SH sensor.

A two sensor system is also utilised in what is known as Stereo-SCIDAR, it trades off a more complex mechanical design for access to both auto-correlation on each camera and cross-correlations between cameras. Each sensor monitors a star in the binary system, resulting in higher contrast on covariance measurements (Shepherd et al., 2014).

The high resolution nature of the SCIDAR turbulence profiles (presented in Figure 2.10) is useful in tomographic adaptive optics systems (Farley et al., 2020), allowing for the reconstruction of the phase aberrations along any line of sight.

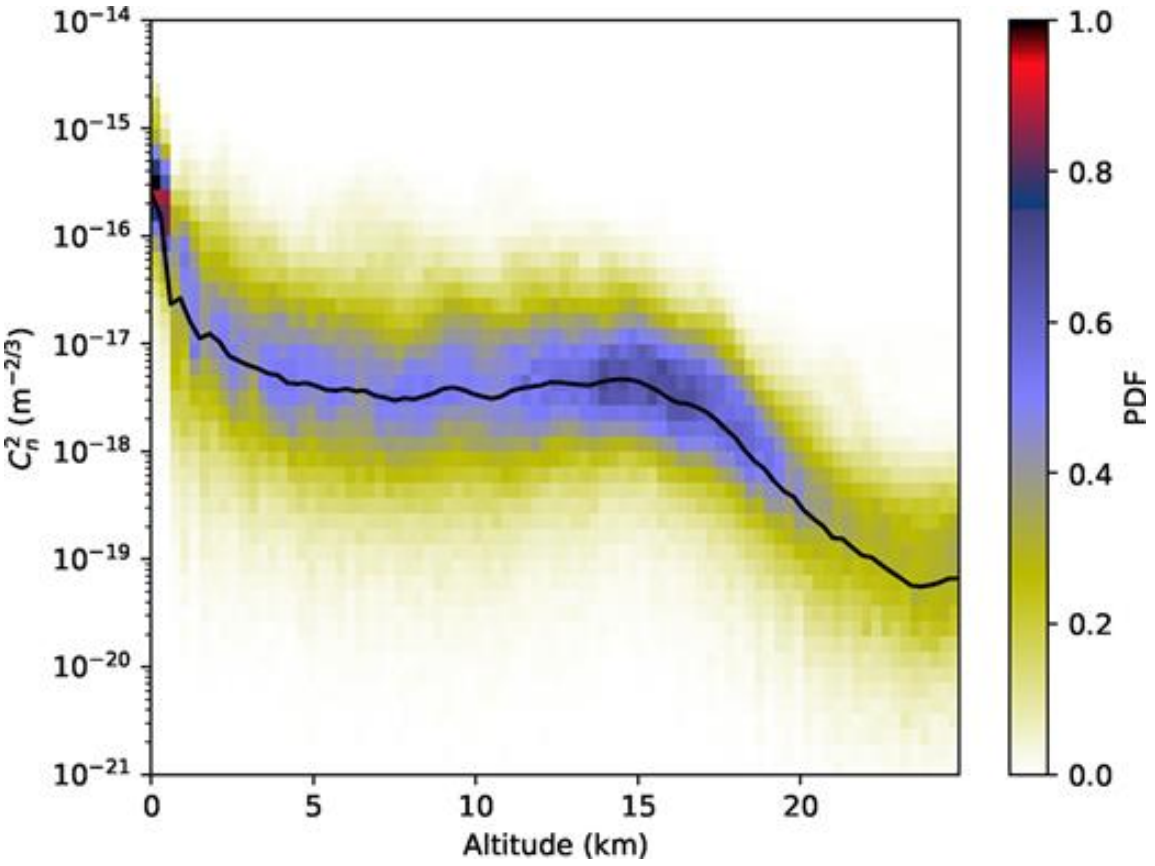

FIGURE 2.10: Turbulence profile obtained from SCIDAR measurements, extracted from (Osborn et al., 2018)

2.3 Turbulence parameter estimation from adaptive optics telemetry data

The estimation of turbulence parameters using adaptive optics telemetry data is now discussed. It is the method employed in this work to estimate the turbulence parameters, as such it's deserving of individual focus.

2.3.1 Adaptive optics operation principle

In broad terms an adaptive optics system aims to correct the effects of the distorted wavefront through the use of a wavefront sensor coupled with a deformable mirror. While the wavefront sensor tracks changes in the atmosphere, the deformable mirror corrects for the fluctuations in the measured wavefront.

Figure 2.11 provides the functioning of the system. It corrects the wavefront through the use of a negative control feedback loop, which is needed due to the temporal evolution of the turbulence. If the AO loop frequency falls under the $1/\tau_0$ threshold, only minor

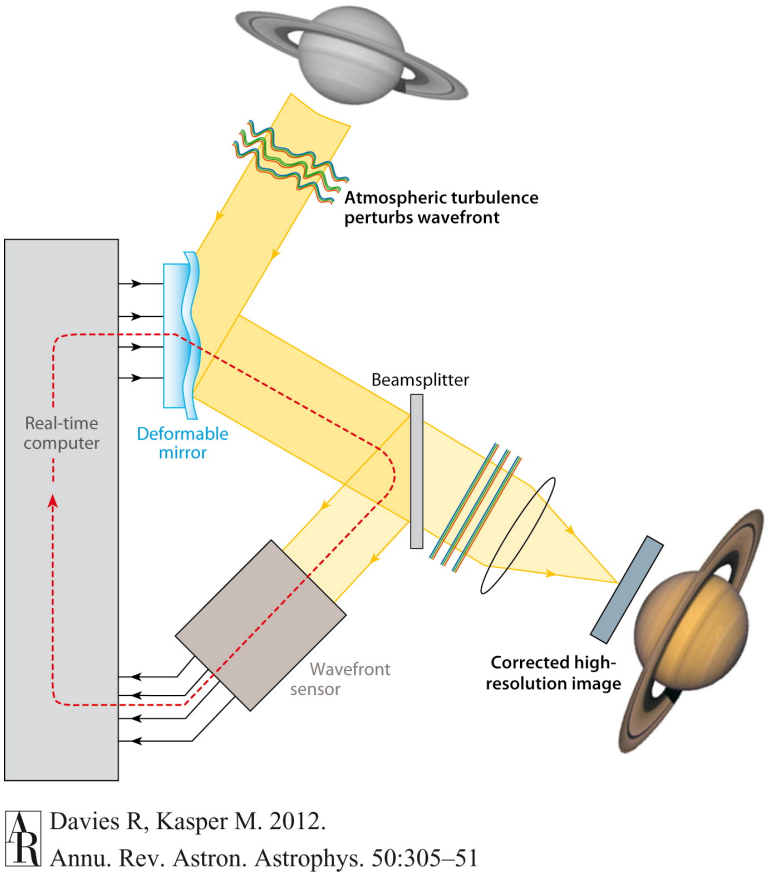

Figure 2.11: Adaptive optics closed loop working principle. Extracted from (Davies and Kasper, 2012)

changes in the wavefront are present, in what we shall refer to as a residual wavefront. When a mirror and sensor are coupled we are working in a closed loop configuration.

2.3.2 Wavefront sensors

We now explore the measurement of the wavefront. Various sensors can be employed in this measurement, such as the curvature sensor and the Pyramid sensor (Ragazzoni, 1996). In this dissertation we will be using measurements from the Shack-Hartmann sensor.

2.3.2.1 The Shack-Hartmann

It is a slope sensor made up of two elements, a lenslet array and a CCD array placed in the focal plane of the lenslet array. Following Figure 2.12 two cases are observed:

- (a) - when a plane, undisturbed, wave-front propagates through the lenslet array point-like images are formed in the focal plane of the lenslets, creating an evenly spaced mesh-grid pattern;

- (b) - when a disturbed wave-front propagates through the lenslet array the images are shifted from the reference positions seen in case (a);

For each lenslet on the array we will decompose the deviation/slope in its x and y components, thus from a single wave-front measurement we will obtain $2M$ measurements, where M is the number of lenslets.

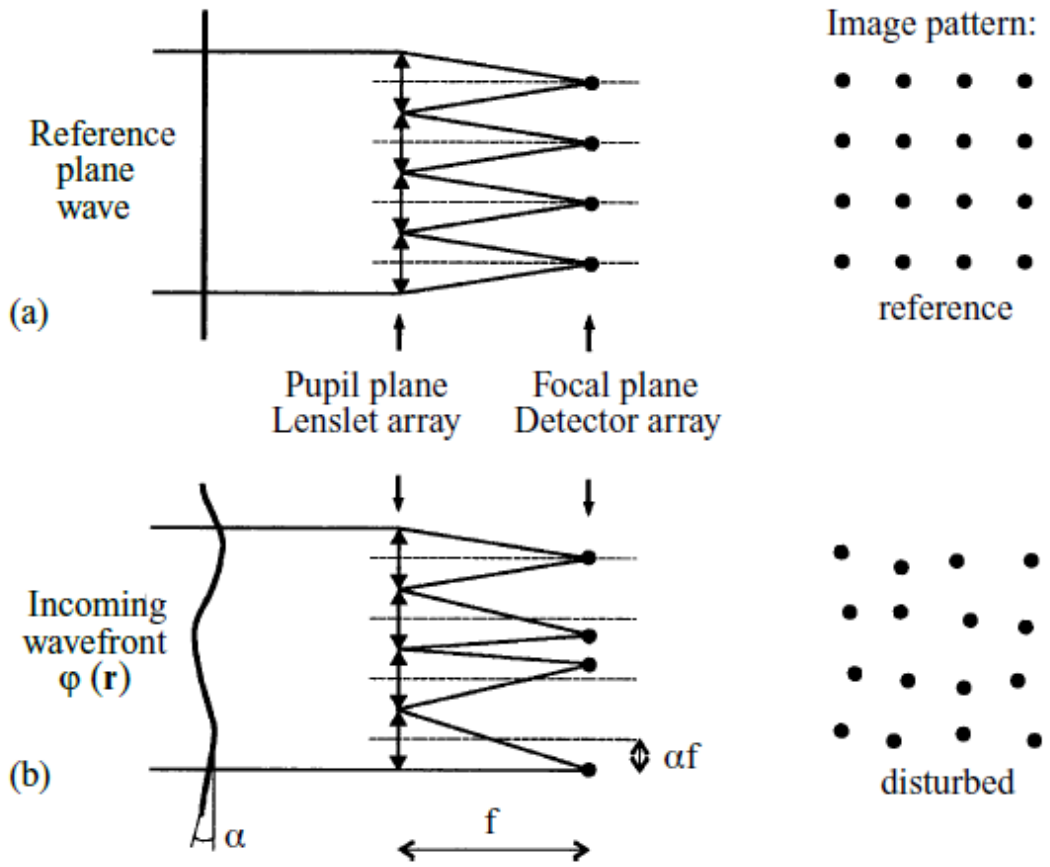

FIGURE 2.12: Working principle of the SH sensor. Extracted from (Roddier, 1999).

From the slope measurements we can perform a basis change, thus translating the slopes measured into a proper modal wavefront basis. The representation of the wavefront in a modal basis is done in this work through the use of Zernike polynomials. The concept of wavefront representation is further described in chapter 3.

As the sensors are limited in resolution, finite reconstruction effects are seen in the form of aliasing. Additionally the Zernike basis used to describe the wavefront phase don't have orthogonal derivatives. Since the SH-sensor measures these derivatives, we will see the presence of what is known as cross-talk effects (ming Dai, 1996). These effects are further described in chapter 3.

2.3.3 Correcting the wavefront

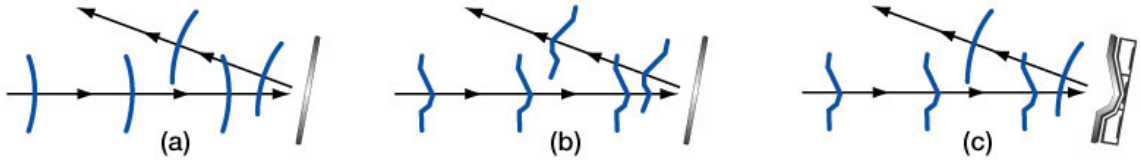

Figure 2.13: Deformable mirror working principle. Extracted from ThorLabs (THO).

Once the wavefront shape is known the correction of the wavefront using a deformable mirror can be achieved.

Several architectures are available (Roddier, 1999), but the working principle remains the same. The mirror can deform locally, thus being able to change its shape. Through the use of a sensor and a control unit, the wavefront shape is mapped into the deformable mirror by way of a control matrix that translates the measured slopes into mirror commands. The deformed mirror will then change the incoming wavefront in order to reverse the effects of the atmosphere, reducing the wavefront to an approximate plane wave.

2.3.4 Telemetry data

Telemetry data is generated from the real time signals associated with the correction. We have two sets of data. One for the sensor data, capturing the wavefront during the loop execution. Following, we have the mirror positions, or voltages, that describe the mirror commands.

From the telemetry data the control loop can be undone in order to obtain pseudo-open modes. From these modes we can obtain the modal temporal variance. This process is formally described in chapter 3.

2.3.5 Turbulence parameter estimation

Adaptive optics systems are ubiquitous in current and future generation telescopes, thus estimation of turbulence parameters from telemetry data has the advantage of using already implemented infrastructure. At the same time, this estimation shares the same turbulence path, thus matching the turbulence parameters to the telescope used for the generation of the telemetry data.

The use of adaptive optics telemetry data for atmospheric sensing and the estimation of turbulence parameters has precedent. Both turbulence sensing from single sensor data

(Schöck et al., 2003; Fusco et al., 2004; Jolissaint et al., 2018; Andrade et al., 2019) and multiple sensors (Guesalaga et al., 2017; Ono et al., 2017) have been achieved.

Measurement noise can be estimated through through temporal auto-correlation (Fusco et al., 2004). It can also be estimated through fitting of theoretical variances (Andrade et al., 2019). The cross-talk estimation is a novel correction proposed by Andrade et al. (2019) and this thesis follows the same approach.

The approach used in this dissertation uses a fitting algorithm to obtain the turbulence parameters. The modal temporal variances are compared to theoretical models and the difference between the two is minimised. Since the temporal variances are affected by measurement noise, aliasing and cross-talk the algorithm estimates their contributions and corrects the modal coefficient variances. Since the modelling of these remaining errors requires knowledge on the turbulence parameters an iterative approach must be used. The full estimation process is described in chapter 3.

Chapter 3

Methods

3.1 Zernike mode decomposition

A representation of a random wavefront can be done multiple ways (Roddier (1999)).

In this work the representation of a wavefront was done through the use of a modal coefficient decomposition associated with a set of basis functions. Each coefficient (a_j) is associated with a function known as a mode. The chosen modal basis is composed of Zernike polynomials, Z_j (Figure 3.1).

In a modal representation any wavefront phase, ϕ, is represented through the sum of the contributions of each mode

$$\phi(r,\theta) = \sum_{j}^{N=\infty} a_j Z_j(r,\theta), \tag{3.1}$$

where the phase is represented in a polar coordinate system (r,θ) and N is the number of modes considered in the reconstruction.

The Zernike modes, $Z_j(r,\theta)$, are defined in a unit circle by simple analytical expressions and thus are easily implemented. They are the result of an angular function coupled with a radial polynomial,

$$Z_n^m(r,\theta) = \sqrt{n+1}R_n^m(r) \begin{cases} \sqrt{2}\cos(m\theta) & m \text{ is even} \\ \sqrt{2}\sin(m\theta) & m \text{ is odd} \\ 1 & (m=1) \end{cases}. \tag{3.2}$$

The n-th term is the radial degree while the m-th is the azimuthal frequency. The radial polynomial, R, is given by

$$R_n^m(r) = \sum_{s=0}^{(n-m)/2} \frac{(-1)^s (n-s)!}{s![(n+m)/2-s]![(n-m)/2-s]!} r^{n-2s}. \tag{3.3}$$

The polynomials are orthogonal in a unit circle since they satisfy the condition

$$\int_0^1 W(r) Z_j Z_{j'} d^2 r = \partial_{jj'}, \tag{3.4}$$

where $W(r)$ defines the unit circle

$$W(r) = \begin{cases} 1/\pi & r \leq 1 \\ 0 & r > 1 \end{cases}. \tag{3.5}$$

Finally the coefficients in equation (3.1), a_j, are expressed as

$$a_j = \int_0^1 W(\rho) \phi(R\rho, \theta) Z_j(\rho, \theta) d^2 \rho. \tag{3.6}$$

Here a scaled radial vector, $\rho = r/R$, was introduced in order to allow for aperture of varying radius.

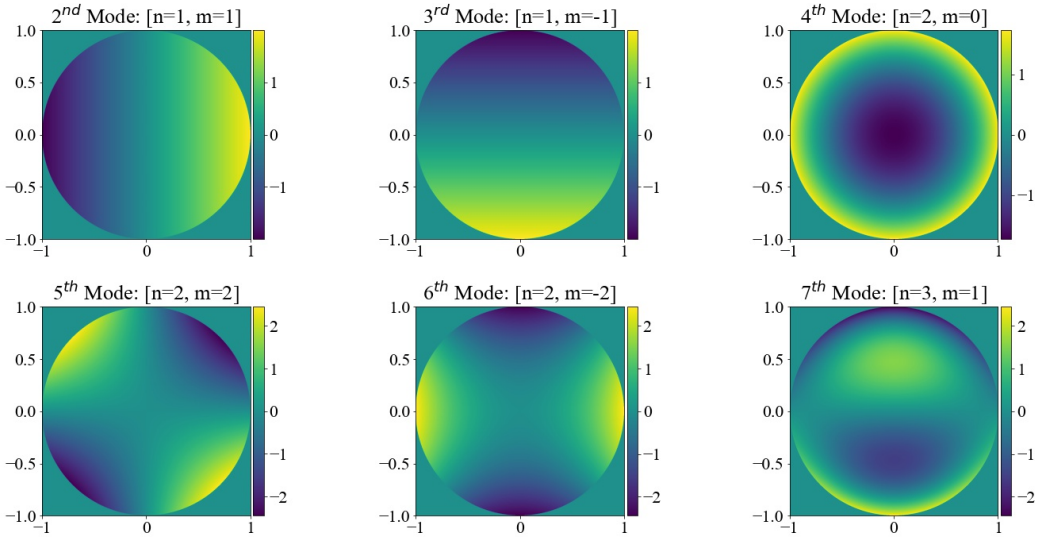

FIGURE 3.1: A representation of the Zernike modes in a circular aperture gives us some indication of their radial and angular dependence. One such example is the fourth mode, corresponding to the defocus aberration, in which there is a radial dependence of the mode, but no azimuthal one.

Other basis, such as the Karhunen-Loève modes, can also be used for a representation of the wavefront. This basis is obtained from the Zernike basis by the diagonalisation of the Zernike covariance matrix and results in statistically independent modes. They are

constructed in this way as the turbulence is modelled statistically. However, because they lack analytic functions they are more difficult to implement in our context.

3.2 Statistical representation

Atmospheric turbulence parameters are statistical terms, as such a single instantaneous value of the coefficients isn't sufficient. The statistical properties of the wavefront depend on the fluctuations of the phase, described by the (co-)variance terms, $\langle a_i a_j \rangle$. The (co-)variance between two coefficients is set by the von Kármán model and was studied by Takato and Yamaguchi (1995). Both variance and covariance are represented in Figure 3.2 and 3.3. These terms are dependent on both the Fried parameter and outer scale.*

In the particular case of a base constructed from Zernike polynomials the covariance matrix is non-diagonal. The non-diagonal terms in the matrix are associated with reconstruction errors of the measured variances, as will be later explained in this chapter. The Karhunen-Loève modes reduce (but don't eliminate) the error in the reconstruction by diagonalising the covariance matrix (ming Dai, 1996).

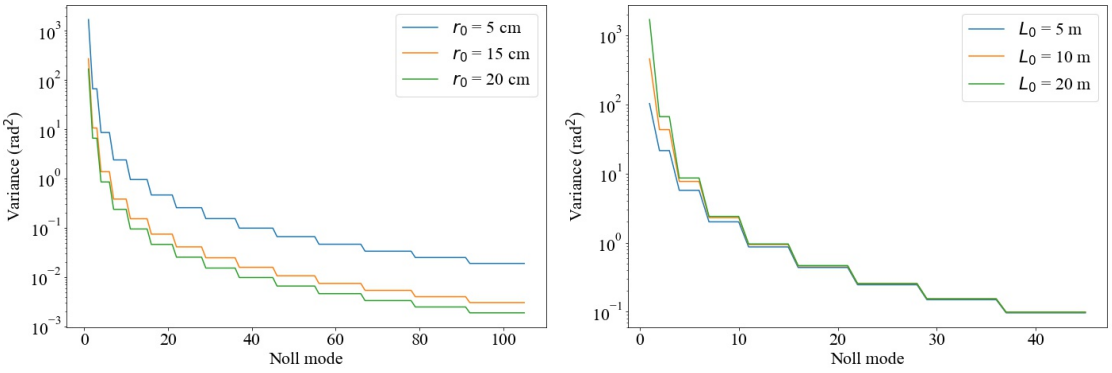

Figure 3.2: As we can see modes with the same radial degree possess the same variance, as the modes in the same radial order vary only in angular terms, θ, and these don't affect the variance. As can be observed in both figures, a dependence is observed in both the Fried parameter (left) and the outer scale (right). The dependence in the outer scale is most pronounced in the lower modes, which possess the highest variance.

*The precise equations used are available in the Appendix.

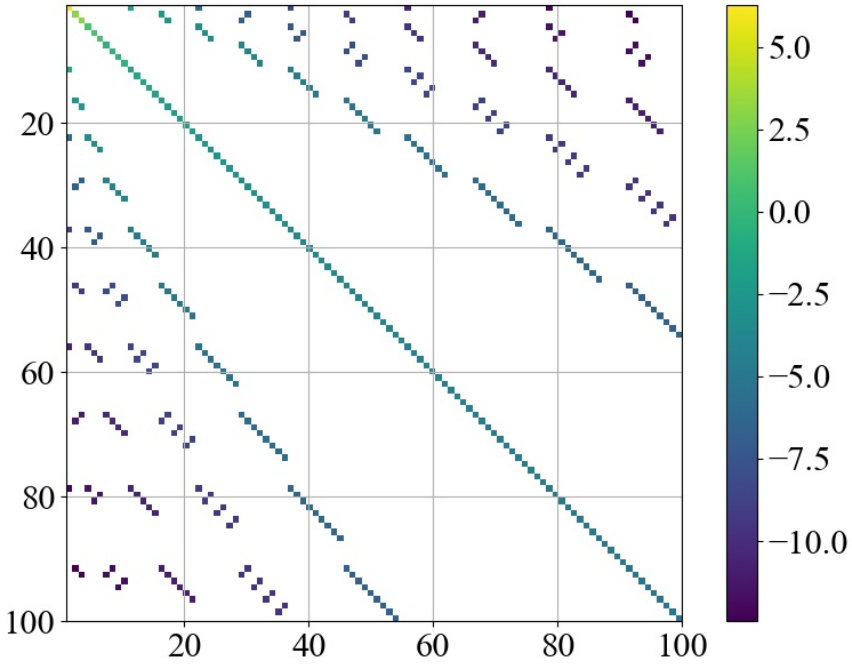

FIGURE 3.3: Covariance of Zernike modes (log scale). Unlike the Karhunen-Loève basis the covariance matrix remains non-diagonal.

3.3 Reconstruction of Zernike Coefficients

The reconstruction of Zernike coefficients from telemetry data is now explored.

Shack-Hartmann wavefront sensors are employed on the Auxiliary Telescopes of the VLT. An in depth analysis of the inner workings of the auxiliary telescope adaptive optics system, NAOMI, was given by Woillez et al. (2019).

Various approaches to the determination of the x and y slopes have been proposed (Tokovinin (2002)), but, regardless of the algorithm selected for the determination of the deviations, we will obtain a final measurement of the slopes

$$\mathbf{s} = \left[s_{x,1},\ s_{x,2},\ ...,\ s_{x,M},\ s_{y,1},\ s_{y,2},\ ...,\ s_{y,M}\right]^{\mathrm{T}}, \tag{3.7}$$

where s_x and s_y are the x and y slopes respectively. A M lenslet sensor is considered in equation (3.7).

A toy model for the measured slopes can be constructed through geometric optics. An incoming wavefront with a tilt given by θ_1, and a position p_1 is assumed. The propagation

of the wave through a lenslet of the Shack-Hartmann is modelled through the use of the thin lens matrix with a focal length of f,

$$\begin{bmatrix} 1 & 0 \\ -\frac{1}{f} & 1 \end{bmatrix} \times \begin{bmatrix} p_1 \\ \theta_1 \end{bmatrix} = \begin{bmatrix} p_2 \\ \theta_2 \end{bmatrix}. \tag{3.8}$$

Now assuming the CCD screen is located in the focal plane of the lenslet array the final position of the wavefront is given by a translation matrix,

$$\begin{bmatrix} 1 & f \\ 0 & 1 \end{bmatrix} \times \begin{bmatrix} p_2 \\ \theta_2 \end{bmatrix} = \begin{bmatrix} p_f \\ \theta_f \end{bmatrix}, \tag{3.9}$$

where the final point can be simplified to

$$\begin{bmatrix} p_f \\ \theta_f \end{bmatrix} = \begin{bmatrix} f\theta_1 \\ -\frac{p_1}{f} + \theta_1 \end{bmatrix}. \tag{3.10}$$

The position of the ray on the CCD has a shift of $f\theta_1$ from the centre of the screen. This is of course a small angle approximation, where the tangent is taken to be equal to the angle.

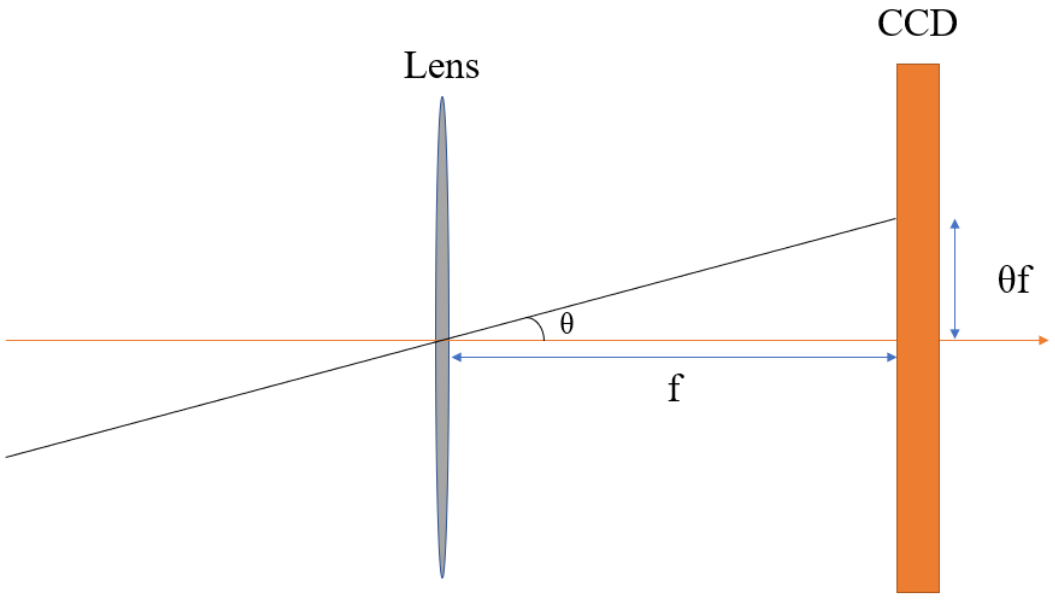

Figure 3.4: Ray propagation for a ray interacting single Shack-Hartmann lenslet. The initial disturbance θ results in the shift from the centre of the screen.

The initial angle, θ_1, in the sensor can be separated into its x and y components (θ_x and θ_y) and related to the phase through

$$\theta_x = \frac{1}{k}\frac{\partial \phi}{\partial x} \tag{3.11}$$

and

$$\theta_y = \frac{1}{k}\frac{\partial \phi}{\partial y}, \tag{3.12}$$

where ϕ represents the phase of the wavefront and k represents the wave vector.

The final position, p_f, in equation (3.10) gives the slope, $\mathbf{s}$, when compared to the reference position in the screen

$$\mathbf{s} = p_f - p_{ref}, \tag{3.13}$$

where we assume the reference position to be the centre and equal to 0.

The slope can be decomposed into its x and y components (s_x and s_y). The slopes and phase can then be related using the phase relations of equation (3.11) and (3.12)

$$\begin{bmatrix} \theta_x \\ \theta_y \end{bmatrix} = \frac{1}{f}\begin{bmatrix} s_x \\ s_y \end{bmatrix} = \frac{1}{k}\begin{bmatrix} \frac{\partial \phi}{\partial x} \\ \frac{\partial \phi}{\partial y} \end{bmatrix}. \tag{3.14}$$

The wavefront phase is then related to the measured slopes. The measured slope will correspond to the derivative of the sensor in a first approximation. From the measured derivatives we have a direct relationship to the Zernike polynomials

$$\frac{\partial \phi(R\mathbf{r})}{\partial x} = \sum_{i}^{N=\infty} a_i \frac{\partial Z_i(\mathbf{r})}{\partial x} \tag{3.15}$$

$$\frac{\partial \phi(R\mathbf{r})}{\partial y} = \sum_{i}^{N=\infty} a_i \frac{\partial Z_i(\mathbf{r})}{\partial y}. \tag{3.16}$$

The previous equation can be put in matrix form

$$\mathbf{s} = \mathbf{G}\mathbf{a}, \tag{3.17}$$

where the gradient matrix, $\mathbf{G}$, is equal to

$$\mathbf{G} = \frac{f}{k}\begin{bmatrix} \sum_i^{N=\infty} \frac{\partial Z_i(\mathbf{r})}{\partial x} \\ \sum_i^{N=\infty} \frac{\partial Z_i(\mathbf{r})}{\partial y} \end{bmatrix}. \tag{3.18}$$

The gradient matrix is known as an interaction matrix, as it translates modes into slopes. Inversely, a matrix that translates slopes into modes is known as a control matrix.

3.3.1 Pseudo-open loop slopes

The proposed estimation algorithm needs to study atmospheric statistics. In a closed-loop adaptive optics system the slope measurements of the Shack-Hartmann sensor are made after correction by the deformable mirror and will correspond to residual slopes. Residual slopes don't represent the full atmospheric statistic and as such pseudo-open slopes must be constructed.

Pseudo-open modes result from the open-loop slope measurements that are reconstructed from the residual Shack-Hartmann slopes and previous deformable mirror states,

$$\mathbf{b}_{\text{atm}}(t) = \mathbf{b}_{\text{DM}}(t) + \mathbf{b}_{\text{SH}}(t-\tau), \tag{3.19}$$

where the reconstructed pseudo-open coefficients are represented by $\mathbf{b}_{\text{atm}}$. Here the wavefront is simply the sum of the mode coefficients from both the Shack-Hartmann sensor, $\mathbf{b}_{\text{SH}}$, and the deformable mirror, $\mathbf{b}_{\text{DM}}$. To account for the response time between the sensor and the deformable mirror a delay time, τ, is introduced. The delay varies between adaptive optics systems, for the NAOMI system the full loop delay is 4.6 ms.

$\mathbf{b}_{\text{atm}}$ represents a real measurement of Zernike coefficients by the system and its difference from a_j coefficients will be explored at a later stage.

The rightmost term in equation (3.19) is obtained from the control matrix response to the slopes data, $\mathbf{s}_{\text{SH}}$. The control matrix, $\mathbf{CM}$, corresponds to the response of the sensor to each Zernike mode, allowing for a conversion of slopes to modes

$$\mathbf{b}_{\text{SH}}(t-\tau) = \mathbf{CM} \times \mathbf{s}_{\text{SH}}(t-\tau). \tag{3.20}$$

The leftmost term is reconstructed by matrix vector multiplication of the deformable mirror commands, $\mathbf{v}_{\text{DM}}$, by the matrix that translates the response of the deformable mirror into mode coefficients, $\mathbf{DM2M}$,

$$\mathbf{b}_{\text{DM}}(t) = \mathbf{DM2M} \times \mathbf{v}_{\text{DM}}(t). \tag{3.21}$$

3.3.2 Fundamental limitations in wavefront reconstruction

Equation (3.1) is an exact representation of the wavefront as it extends its sum over all possible modes ($N = \infty$). However a real Shack-Hartmann sensor is limited in its measurements, only being able to perform $2M$ measurements. This will inevitably lead to

limitations in the reconstruction of an infinite sum by way of finite measurements.

The standard approach to the conversion of the $\mathbf{s}$ vector to a finite Zernike coefficient vector was studied by Dai in 1996 (ming Dai, 1996).

Due to the finite resolution in the Shack-Hartmann sensor, the estimation is truncated to the first L modes. These modes are chosen to be modes that don't contain aliasing, in the context of the NAOMI system all controlled modes comply to this condition.

The exact coefficients representing the wavefront, $\mathbf{a}$, are then separated into the fitted L modes, $\mathbf{a_f}$, and remaining high-order modes, $\mathbf{a_r}$. The slopes, $\mathbf{s}$, are re-written as

$$\mathbf{s} = \mathbf{G}\begin{bmatrix} \mathbf{a_f} \\ \mathbf{a_r} \end{bmatrix} = \mathbf{G_f a_f} + \mathbf{G_r a_r}, \tag{3.22}$$

where $\mathbf{G}$ is defined as

$$\mathbf{G} = \frac{f}{k}\begin{bmatrix} \frac{\partial Z_1|_1}{\partial x} & \frac{\partial Z_2|_1}{\partial x} & \cdots & \frac{\partial Z_N|_1}{\partial x} \\ \frac{\partial Z_1|_1}{\partial y} & \frac{\partial Z_2|_1}{\partial y} & \cdots & \frac{\partial Z_N|_1}{\partial y} \\ \vdots & \vdots & \ddots & \vdots \\ \frac{\partial Z_1|_M}{\partial x} & \frac{\partial Z_2|_M}{\partial x} & \cdots & \frac{\partial Z_N|_M}{\partial x} \\ \frac{\partial Z_1|_M}{\partial y} & \frac{\partial Z_2|_M}{\partial y} & \cdots & \frac{\partial Z_N|_M}{\partial y} \end{bmatrix}, \tag{3.23}$$

and is obtained by extending the single lenslet equation (3.18) to M lenslets. $\mathbf{G_f}$ is the matrix containing the first L columns of $\mathbf{G}$ and $\mathbf{G_r}$ is constructed from the remaining high-order columns.

The least-squares solution of equation (3.22) is given by inverting the $\mathbf{G_f}$ matrix

$$\mathbf{b} = \mathbf{G_f^+ s}, \tag{3.24}$$

where $\mathbf{G_f^+}$ is the general inverse matrix of $\mathbf{G_f}$

$$\mathbf{G_f^+} = (\mathbf{G_f^t G_f^{-1}})\mathbf{G_f^t} \tag{3.25}$$

and is known as the reconstruction matrix (represented in Figure 3.5).

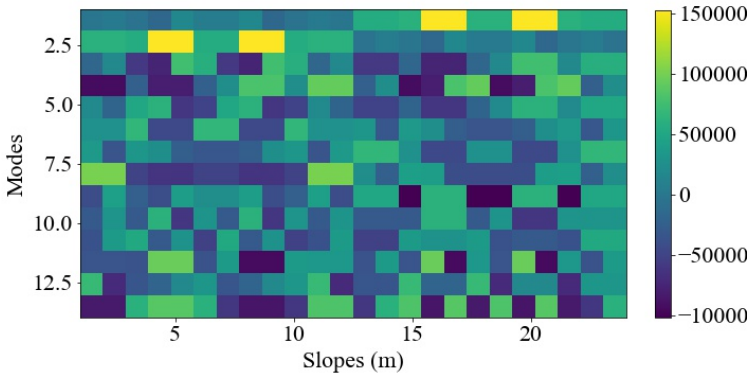

Figure 3.5: Representation of the $\mathbf{G}_{\mathbf{f}}^{+}$ matrix for the first 14 Noll modes.

3.3.2.1 Aliasing

The finite resolution of the wavefront sensor is now contemplated. The wavefront can only be measured by the adaptive optics system below a cutoff spatial frequency f_c because of limited sampling in the wavefront sensor or in the deformable mirror. The critical frequency is expressed as half of the sampling frequency of the system, f_s, i.e. for a given frequency, f, to be detected a $2f$ sampling frequency must be achieved. The Nyquist–Shannon sampling theorem gives us the cutoff frequency,

$$f_c = \frac{f_s}{2}. \tag{3.26}$$

Any frequency above the cutoff frequency is considered to be aliased.

Aliasing adds high-order modal contributions to low-order modes. Numerically aliasing is described as a low order of the Gradient matrix, $\widehat{G_N}$, being composed of a linear combination of low and high order modes

$$\widehat{G_N} = G_N + \sum_{i=N+1}^{V=\infty} c_i G_i. \tag{3.27}$$

The sampling frequency of a Shack-Hartmann is related to its optical design, through the diameter of the array, D, and the number of lenslets

$$f_s = \frac{M}{D}. \tag{3.28}$$

Thus the maximum detectable frequency will be

$$f_M = \frac{M}{2D}. \tag{3.29}$$

An equivalence to the approximate maximum non-aliased radial order, r_M, can be formed by way of (Conan et al., 1995)

$$r_M \sim 3.3(M-1). \tag{3.30}$$

Any columns of the gradient matrix, $\mathbf{G}$, above the r_M radial order will possess a dependence on high-order radial modes.

The minimum measurable frequency of the system is given by the total diameter of the array,

$$f_m = \frac{1}{D}. \tag{3.31}$$

3.3.2.2 Cross-Talk Effects

Substituting equation (3.17) into equation (3.24) shows

$$\mathbf{b} = \mathbf{G_f^+ G a}. \tag{3.32}$$

By splitting the gradient matrix into fitted and remaining modes it is possible to separate the contributions

$$\begin{aligned} \mathbf{b} &= \mathbf{G_f^+}(\mathbf{G_f a}_f + \mathbf{G}_r \mathbf{a}_r) \\ &= \mathbf{a_f} + \mathbf{G_f^+ G_r a_r}. \end{aligned} \tag{3.33}$$

There is now an explicit term for the dependence on higher order modes resulting from the truncation of the $\mathbf{G}$ matrix. The second term of the equation indicates how $\mathbf{b}$ is affected by the high-order terms not present in the reconstruction matrix, $\mathbf{G_f^+}$. This dependence is known as the cross coupling effect and is dictated by the cross-talk matrix

$$\mathbf{C} = \mathbf{G_f^+ G_r}. \tag{3.34}$$

This cross coupling effect is present since the used sensor measures derivatives of the wavefront phase and the derivatives of the Zernike basis aren't orthogonal. The same truncation of the Gradient matrix for a basis with orthogonal derivatives will yield a null cross-talk effect (Herrmann, 1981).

3.3.2.3 Measurement Noise

Random noise is introduced in the sensor due to several effects (McLean, 2008). These effects will appear in equation (3.22) through a noise term

$$\widehat{\mathbf{s}} = \mathbf{s} + \mathbf{e} \tag{3.35}$$

where $\widehat{\mathbf{s}}$ represents the slopes with added noise, $\mathbf{e}$ represents the noise contributions and $\mathbf{s}$ represents the previously seen noiseless slopes. Following the same approach from the previous sections the reconstructed coefficients with noise, $\widehat{\mathbf{b}}$, can now be expressed as

$$\begin{aligned} \widehat{\mathbf{b}} &= \mathbf{G}_\mathbf{f}^{+}(\mathbf{G}_\mathbf{f}\mathbf{a}_f + \mathbf{G}_r\mathbf{a}_r + \mathbf{e}) \\ &= \mathbf{a_f} + \mathbf{G}_\mathbf{f}^{+}\mathbf{G_r}\mathbf{a_r} + \mathbf{G}_\mathbf{f}^{+}\mathbf{e}. \end{aligned} \tag{3.36}$$

3.3.3 Measured variances

The variances are now evaluated through equation (3.36). Considering the effects of the cross-talk matrix and the error on the variance of the measured coefficients, $\widehat{\mathbf{b}}$:

$$\langle \widehat{\mathbf{b}}\widehat{\mathbf{b}}^\mathbf{t} \rangle = \langle \mathbf{a_f}\mathbf{a}_\mathbf{f}^\mathbf{t} \rangle + \mathbf{C}\langle \mathbf{a_r}\mathbf{a}_\mathbf{r}^\mathbf{t} \rangle \mathbf{C}^\mathbf{t} + 2\mathbf{C}\langle \mathbf{a_r}\mathbf{a}_\mathbf{f}^\mathbf{t} \rangle + \mathbf{G}_\mathbf{f}^{+}\langle \mathbf{e}\mathbf{e}^\mathbf{t} \rangle (\mathbf{G}_\mathbf{f}^{+})^\mathbf{t} \tag{3.37}$$

The measurement noise is assumed to be uncorrelated between measurements, $\langle \mathbf{e}\mathbf{a}_\mathbf{r}^\mathbf{t} \rangle = 0$ and $\langle \mathbf{e}\mathbf{a}_\mathbf{f}^\mathbf{t} \rangle = 0$. The variance of a single reconstructed coefficient is then obtained from

$$\langle \widehat{b}_i^2 \rangle = \langle a_{f,i}^2 \rangle + T_{cc,i} + \sigma_{n,i}^2, \tag{3.38}$$

where the error of the reconstruction associated with the cross-talk is

$$T_{cc,i} = \sum_{j=L+1}^{\infty} \sum_{j'=L+1}^{\infty} c_{ij} \langle a_{r,j} a_{r,j'} \rangle c_{j'i}^t + 2 \sum_{j=L+1}^{\infty} c_{ij} \langle a_{f,i} a_{r,j} \rangle \tag{3.39}$$

.

Additionally, since assumed that errors in the measurement were equal and uncorrelated between measurements

$$\langle \mathbf{e}\mathbf{e}^\mathbf{t} \rangle = \sigma_0^2, \tag{3.40}$$

where the σ_0^2 is the error of a single measurement. Thus the total noise contribution sums over all $2M$ lenslet measurements

$$\sigma^2_{n,i} = \sum_{j=1}^{2M} \sum_{j'=1}^{2M} g^+_{f,ij} \sigma^2_0 (g^+)^t_{f,j'i}. \tag{3.41}$$

where g^+_f are entries of the reconstruction matrix.

Analysing a real set of variances, the cross-talk is estimated and presented in Figure 3.6. The presence of negatives terms illustrates the reason for the cross-talk terms not being thought as a σ^2 term.

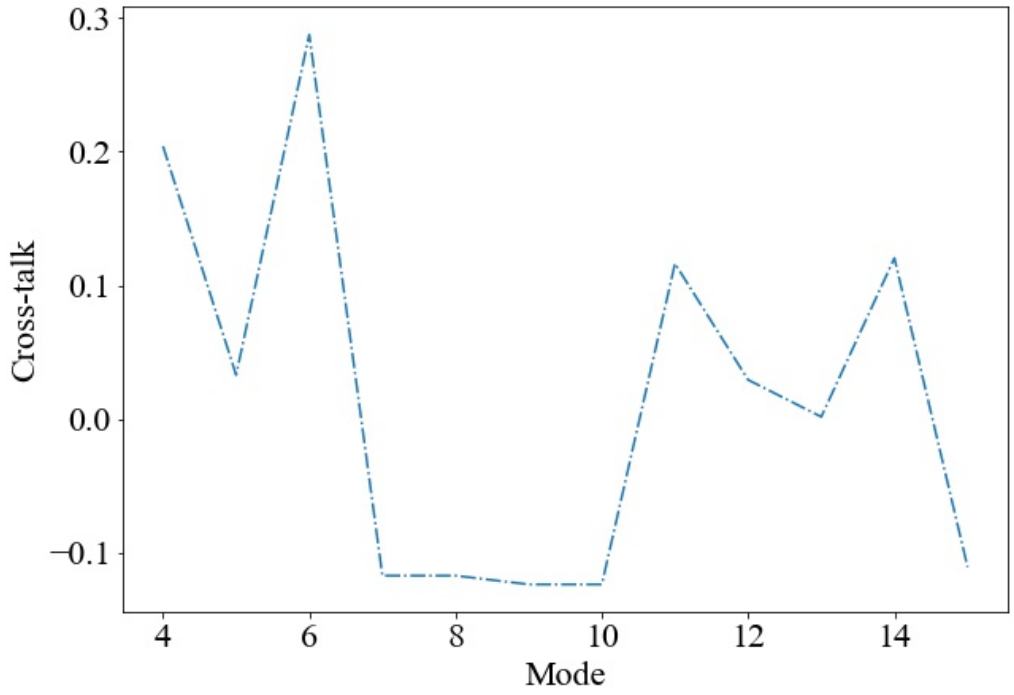

FIGURE 3.6: Example of cross-talk terms for a typical variance at Paranal.

3.4 Turbulence parameter estimation

The correction algorithm proposed by Andrade et al. (2019) takes into account the effects of the cross-talk and measurement noise. Both the Fried parameter and outer scale are obtained from the fit of the reconstructed temporal variances, $\langle \widehat{\mathbf{b}}^{\mathbf{2}}_{\mathbf{i}} \rangle$. These are compared to the theoretical variances of the von Kármán distribution, $\langle a^2_{f,i} \rangle_{vK}$,

$$f(\mathbf{p}) = (\langle a^2_{f,i} \rangle_{vK} + \sigma^2_{n,i})(\mathbf{p}), \tag{3.42}$$

which acts as a fitting function. The left term of the fitting function represents the model variances, following the theoretical spectra. The rightmost term represents an included noise term, allowing for the simultaneous fitting of noise and the turbulence parameters. As such the fitting parameter, $\mathbf{p}$, is a function of

$$\mathbf{p} = [r_0, \mathcal{L}_0, \sigma_0^2]. \tag{3.43}$$

The fitted parameters are then determined by minimum difference between fitting function and reconstructed variances

$$\mathbf{p^k} = \arg\min_{\mathbf{p}} \sum_{i=4}^{J(r)} \left\{ \log\left[\langle \widehat{b}_i^2 \rangle\right] - \log\left[f(\mathbf{p})\right] \right\}^2, \tag{3.44}$$

where $\mathbf{p^k}$ represents the fitting parameters of the k iteration. $J(r)$ represents the number of Noll modes considered in a reconstruction up to the radial order, r. Since wind-shake and vibrations greatly affect the tip/tilt modes (i.e. the second and third Noll modes) these are not included in the fit, as they won't follow the expected turbulence spectra. The logarithmic transformation of the variances is used to normalise the residuals of the function.

The cross-talk estimation is handled with a different approach. The error provoked by cross-coupling is removed from the fitted variances

$$\langle b_{i,cc}^2 \rangle = \langle \widehat{b}_i^2 \rangle - T_{cc,i}(r_0, \mathcal{L}_0) \tag{3.45}$$

The error of the cross-talk is estimated using equation (3.39), where the cross-talk matrix is calculated from the gradient matrix associated with the adaptive optics system and the theoretical co-variances are computed using Takato and Yamaguchi's formulation (Takato and Yamaguchi, 1995). The co-variance expressions are functions of both the Fried parameter and the outer scale.

The fitting algorithm will then take the form of

$$\mathbf{p^k} = \arg\min_{\mathbf{p}} \sum_{i=4}^{J(r)} \left\{ \log\left[\langle \widehat{b}_i^2 \rangle - T_{cc,i}(\mathbf{p^{k-1}})\right] - \log\left[f(\mathbf{p})\right] \right\}^2, \tag{3.46}$$

where the turbulence parameters used for the cross-error error are based on the last iteration. Since this error depends on the turbulence parameters a iterative approach is taken. With each iteration, k, the algorithm uses the previous fit to recalculate the cross-talk. Convergence is observed for the turbulence parameters as the algorithm iterates.

Since the first iteration ($k = 0$) doesn't have a previous iteration , $k - 1$, the cross-talk error estimation can't be performed. As such in the first iteration the cross-talk error is not considered, using uncorrected variances instead, as is illustrated by equation (3.44).

3.4.1 Innovations to the Andrade algorithm

The Andrade method was further expanded by removing the logarithmic transformation in favour of a χ^2 method with a variable standard deviation (Bevington and Robinson, 2003)

$$\mathbf{p^k} = \arg\min_{\mathbf{p}} \sum_{i=4}^{J(r)} \left\{ \frac{\left[\langle \widehat{b}_i^2 \rangle - T_{cc,i}(\mathbf{p^{k-1}})\right]}{\sigma_{r,i}} - \frac{[f(\mathbf{p})]}{\sigma_{r,i}} \right\}^2 , \tag{3.47}$$

where $\sigma_{r,i}$ is the standard deviation of the mean of the radial order. Each radial order has a singular modal variance, shared between azimuthal orders, and as such any deviation from this variance can be seen as deviation to the mean. A standard deviation is used since we are assuming a normal distribution of the azimuthal orders around a the mean value of the radial order.

The χ^2 is a statistic that characterises the dispersion of an observed frequency from the expected frequency. In the algorithm the minimisation of the χ^2 is being used as a fitting function for the turbulence parameters by changing the values of the turbulence parameters in the fitting function, $f(\mathbf{p})$.

This alteration allows us to apply known statistical methods to our estimated data, as a large body of work as been built for the χ^2 methods. The new algorithm allows the estimation of uncertainty of the fitted values, $\mathbf{p}$. Without this step it's impossible to study the results as we don't know how significant an estimation is. The estimation of the uncertainty is possible with a Monte Carlo simulation. A Monte Carlo methodology uses random sampling to study the significance of the data. For this method to work the random sampling must follow the statistic behaviour of our data. The set of variances, $\langle \widehat{\mathbf{b}}^{\mathbf{2}} \rangle$, are assumed to follow a normal distribution around the mean in each radial order, r, with a $\sigma_{r,i}$ deviation from the mean.

Since a distribution is associated with the variances we can implement a Monte Carlo method using the following method:

1. A new sample of variances is generated from the normal distribution of the mean of the variances

$$\langle b^2_{MC,i} \rangle = \mathcal{N}(\langle \widehat{b}^2_i \rangle, \sigma_{r,i}), \tag{3.48}$$

where the $\langle b^2_{MC,i} \rangle$ represents the new generated variance set and $\mathcal{N}$ represents the normal distribution with a mean $\langle \widehat{b}^2_i \rangle$ and standard deviation $\sigma_{r,i}$.

2. The iterative estimation algorithm is applied to the $\langle b^2_{MC,i} \rangle$ variances, resulting in a new set of $\mathbf{p_i}$ parameters;

3. Return to step 1;

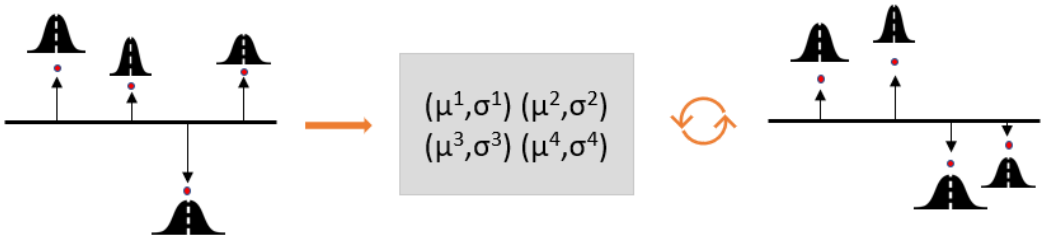

Figure 3.7: Sample generation process for the third radial order. From the initial distribution of the 4 variances we gather the mean and standard deviation of each points, these will then be used to generate a sample of each additional variance, according to a normal distribution following the seed variances taken from the initial data.

Since the study of the uncertainty is done by repeated generation of new values of $\mathbf{p}$ we are interested in the calculation of the error of the mean $\mathbf{p}$ estimation. The Monte Carlo algorithm proceeds by generating H $\mathbf{p}$ samples following the statistical distribution of the initial variances.

From the H turbulence parameters generated the uncertainty of the mean is then given by the standard deviation of the mean (Bevington and Robinson, 2003). For the Fried parameter the uncertainty is given by

$$\sigma_{r_0} = \frac{1}{H} \left[\sqrt{\sum_{i=1}^{H} (r_{0,i} - \overline{r_0})^2} \right], \tag{3.49}$$

where $\overline{r_0}$ is the mean of the Fried parameter for the H samples and $r_{0,i}$ is the Fried parameter resulting from step 2 of the sample generation method in each of the samples.

Chapter 4

The NAOMI system

4.1 The NAOMI system

FIGURE 4.1: AT positions across Paranal. Each AT is circled in red. Extracted from ESO.

The new adaptive optics module for interferometry (NAOMI, Figure 4.2) system is the current adaptive optics system for the Auxiliary Telescopes (AT, Figure 4.1) of the Very Large Telescope. NAOMI is installed on all four ATs.

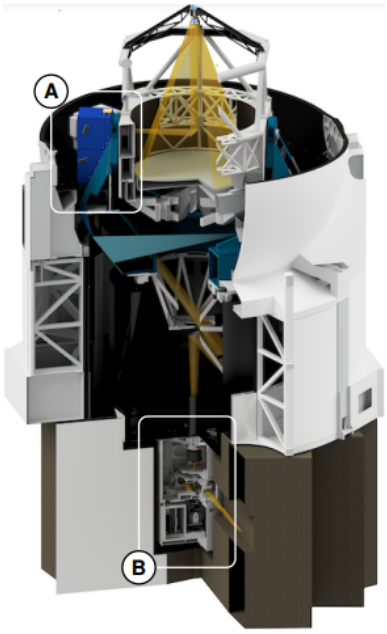

FIGURE 4.2: NAOMI system schematic: (A) represents the deformable mirror location, while (B) represents the wavefront sensor position. Extracted from (Woillez et al., 2019).

In Table 4.1 we sum up the characteristics of the adaptive optics loop in the NAOMI system (Woillez et al., 2019).

TABLE 4.1: Features of the NAOMI adaptive optics system. Adapted from Woillez et al., 2019 (Woillez et al., 2019)

diameter	1.8 m
obstruction ratio	7.7 %
loop frequency	500 - 50 Hz
pixel Scale	0.375 ”pix^{-1}
sub apertures	4x4
valid sub apertures	12
full loop delay	4.6 ms
Corrected modes	4-15

4.2 Simulation model

In this section a well tested adaptive optics simulation package was used to simulate NAOMI's features and parameterise the system. The simulation was done using the OOPAO (Object Oriented Python Adaptive Optics) package, developed by C.T. Heritier.

By propagating a generated screen through a telescope and wavefront object we can obtain a set of slope measurements. The slopes obtained from the wavefront sensor are then translated to Zernike coefficients using a control matrix. The estimation algorithm is

then applied to the temporal variances of the modal coefficients to obtain the turbulence parameters.

Through simulation the real data-set can be curated, defining the features that will encompass the analysed data.

4.2.1 Generation of phase screens

4.2.1.1 The atmosphere at Paranal

If we want to estimate the performance of the NAOMI system the phase screens utilised in the simulation must reflect the Paranal atmosphere. In order to do so we used correlated phase screens that follow the features seen in Table 4.2. These are generated using the algorithm proposed by Assémat et al. (2006) through the AOTools python package.

Table 4.2: Simulation conditions used in the generation of the phase screens.

Parameter	Value
Fried Parameter	14.6 cm
Outer-scale	18.9 m
Type of phase screens	Correlated
# Layers	9

The atmospheric layer altitude and wind-velocity conditions are taken from ESO's campaign to characterise the observatory and are presented in Figure 4.3. No noise was introduced in the screens.

4.2.1.2 Validation of phase screens

Before introducing the telescope and wavefront sensor we must study if the phase screens follow the expected coefficient variance of the model. The modal coefficients of a single atmospheric screen are obtained by orthogonal projection onto the Zernike polynomials,

$$P_{\text{screen},i} = \phi_{\text{screen}} \cdot \phi_{Z_i}, \tag{4.1}$$

where ϕ_{screen} represents the phase screen, ϕ_{Z_i} the phase of the Zernike polynomial and where $P_{\text{screen,i}}$ represents the projection of the two.

The Fried parameter and outer scale can be estimated by using the 0^{th} iteration of the algorithm discussed in Chapter 3. Since the screens don't possess noise and since the phase screen isn't propagated through a wavefront sensor cross-talk errors are absent. As such the iteration of the algorithm isn't needed.

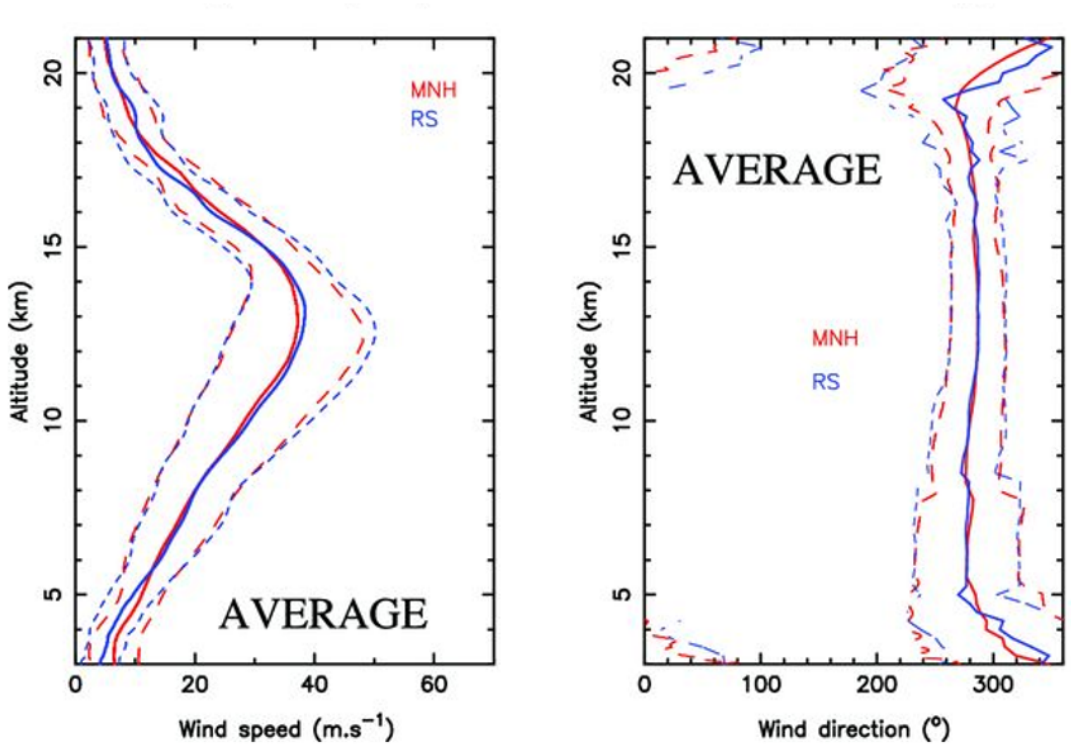

FIGURE 4.3: Wind-speed and wind-direction at the Paranal observatory. Extracted from (Masciadri et al., 2013).

In Figure 4.4 we see a convergence for the Fried parameter, while the outer scale parameter doesn't converge for a simulation with a large amount of screens, as is illustrated in Figure 4.5. Additionally, the final stable value of the Fried parameter doesn't correctly correspond to the values introduced in the simulation. The cause of this mismatch is not yet well understood, but it can be caused by sampling effects or screen size effects on the generation of the turbulence screens.

The results presented in Figure 4.4 and 4.5 were obtained from a single simulation. As such a larger number of simulation are warranted to develop a statistically significant sample on the generation of the phase screen.

4.2.1.3 Loop configurations

We can now introduce the atmosphere to a measurement pipeline. Two configurations are considered:

1. Open loop configuration - doesn't correct for the fluctuations in the phase of the screen, only measuring the slopes as the atmosphere evolves;

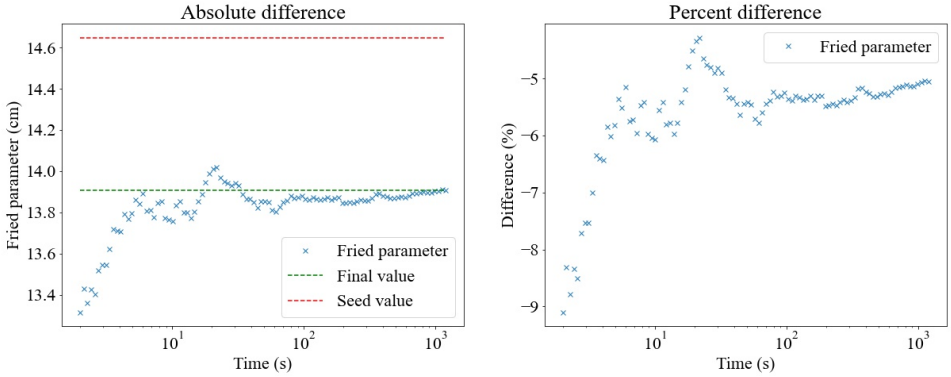

Figure 4.4: Convergence of the Fried parameter through projection of Zernike modes.

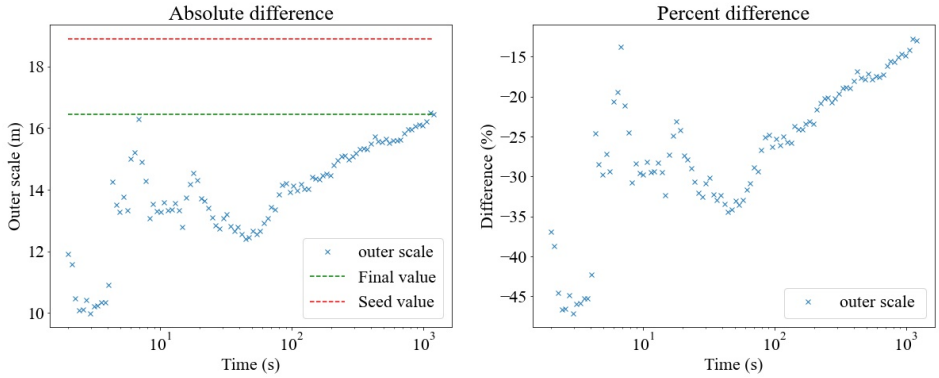

Figure 4.5: Convergence of the outer scale through projection of Zernike modes.

2. Closed loop configuration - the measured wavefront is corrected by a deformable mirror. The wavefront sensor now tracks residual changes in the wavefront. To obtain the Zernike coefficients of the atmosphere screen we must construct pseudo-open slopes, described in Section 3.3.1.

The first configuration was utilised in our simulation. The second configuration corresponds to the NAOMI system working principle. Using pseudo open slopes in the real data analysis we can expect an analogous behaviour to that of the simulated values.

4.2.2 Shack-Hartmann sensor

As a first step to understand the open loop configuration performance we aim to understand how a measurement of the wavefront sensor, given in slopes, can be translated to the desired modal basis. As discussed in Section 3.3 there is a need to obtain a matrix that allows the change in basis from the slopes space to the modes space, the gradient matrix, $\mathbf{G}$.

The telemetry samples already contain a gradient matrix, $\mathbf{G}_{\text{system}}$, obtained from the inverted control matrix that accounts for the first 14 controlled modes. For the additional modes needed for a cross-talk estimation we must extend the matrix through simulation. We do this by simulating the response of the Shack-Hartmann and obtaining a $\mathbf{G}_{\text{model}}$. The $\mathbf{G}_{\text{system}}$ will serve as reference to the $\mathbf{G}_{\text{model}}$.

4.2.2.1 Simulation of the gradient matrix

The response of a system is catalogued by introducing a single Zernike mode on the pupil of the telescope. This can be extended to any number of Zernike modes. The sensor response is then recorded, resulting in a relationship between the applied Zernike mode to a set of slopes in the sensor.

The response to a single mode, R_i, is then represented as

$$R_i = \begin{bmatrix} \frac{\delta Z_i|_1}{\delta x} & \frac{\delta Z_i|_1}{\delta y} & \cdots & \frac{\delta Z_i|_M}{\delta x} & \frac{\delta Z_i|_M}{\delta y} \end{bmatrix}^T . \tag{4.2}$$

The $\mathbf{G}$ matrix is then simulated by sweeping over a large number of modes, where 105 modes were recorded.

Figure 4.6 describes the results of the generation of the gradient matrix for some of the modes of operation. Agreement between the simulated gradient matrix and the system matrix was found, a median error of 1.3% is present between the two matrices. From these results we can confidently expand our matrix to higher modes.

4.2.2.2 Aliasing frequency

Following the discussion in section 3.3.2.1, any spacial frequency above $1.1\,\text{m}^{-1}$ is aliased, which will be roughly equivalent to any radial order above 5 being aliased (Conan et al., 1995). The remaining error, composed of aliasing, cross-talk and measurement noise contributions will then be corrected by the algorithm without explicitly separating the components.

As can be seen in equation (3.34), the cross-talk matrix depends on the remaining modes $\mathbf{G}_\mathbf{r}$, which will contain aliasing for any column above the 5^{th} radial order. Figure 4.7 illustrates the overlap of the cross-talk with aliasing, where only one order of cross-talk isn't overlapped with aliasing.

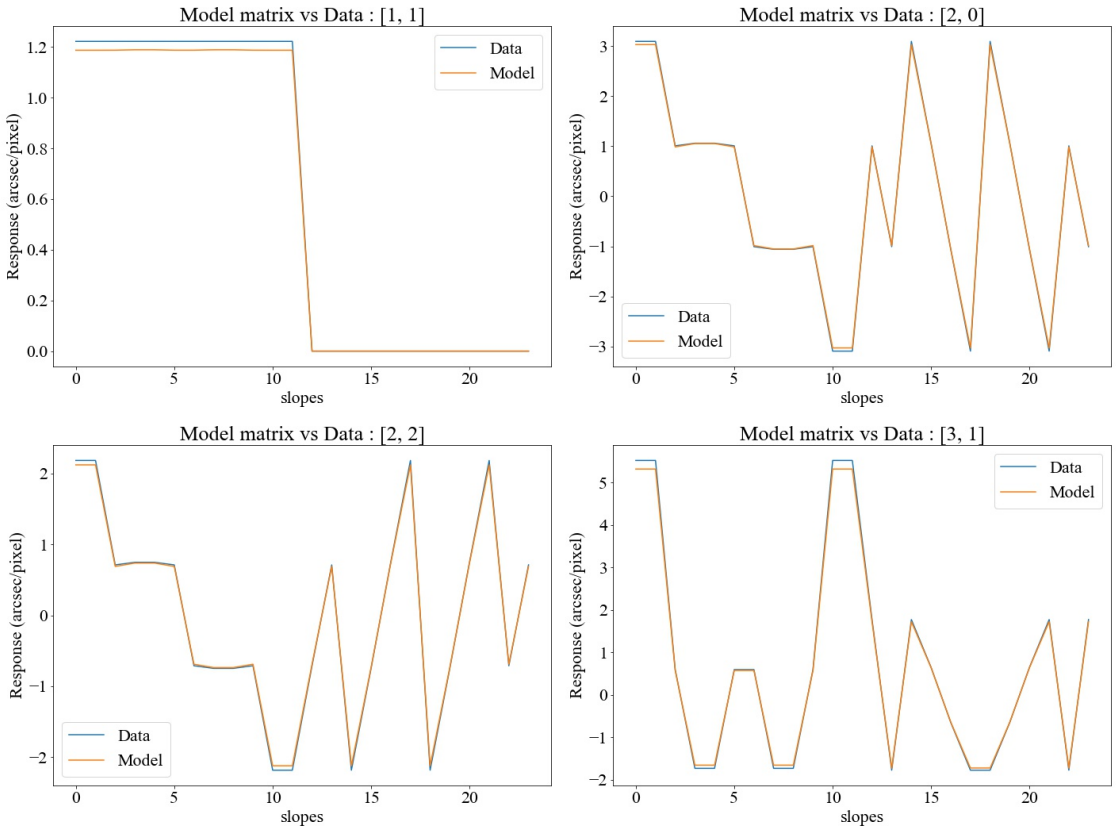

Figure 4.6: Comparison between the response of the gradient matrix obtained from simulation and data, using conventional slope ordering.

4.2.2.3 Minimum measurable frequency

The diameter of the telescope will determine the maximum distance of two points in the detection. The telescope diameter , D, of the ATs is 1.8 m. The minimum measurable spacial frequency is then

$$f_{\min} = \frac{1}{D} = 0.556\,\mathrm{m}^{-1}. \tag{4.3}$$

NAOMI is only sensitive to spatial scales roughly smaller than 2 meters. As is verified in Figure 2.4, the effects of the outer scale on the structure function become pronounced once the spatial scale is close to the outer scale. Since the outer scale varies between $(1-100)$m this leaves the system insensitive to most conditions. NAOMI is considered to be in the inertial regime of turbulence.

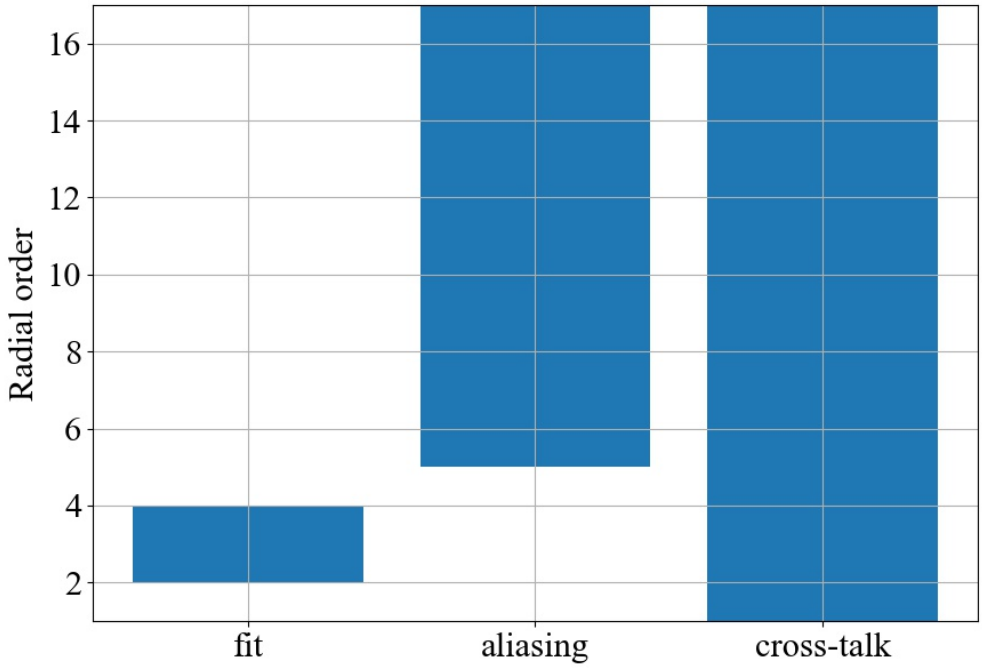

FIGURE 4.7: Overlap between cross-talk and aliasing in the estimation algorithm.

4.2.2.4 Mode reconstruction

Utilising the expanded gradient matrix we can now convert the measured slopes into Zernike coefficients. The modal coefficients are obtained from the slopes of the Shack-Hartmann sensor through equation (3.24). The second through fourth radial order modes were reconstructed.

The estimation algorithm described in Section 3.4.1 is applied to obtain the turbulence parameters of the system, where $\langle \widehat{\mathbf{b}^2} \rangle$ will be the modes obtained from the simulation.

4.3 Algorithm parameter optimisation

An optimisation of the algorithm parameters is now performed. The optimisation will be performed by individual tuning of the features of the algorithm:

- Number of iterations, k, of the algorithm;
- Convergence in time;
- Maximum order included in the $\mathbf{G_r}$ matrix;

- Maximum order of the fitted modes, $\langle \widehat{\mathbf{b}^2} \rangle$;
- Ideal initial guess for the algorithm;

4.3.1 Number of iterations of the algorithm

A study of the number of iterations in the estimation algorithm is necessary in order to understand the efficacy of our cross-talk correction.

The impact of the cross-talk error on the estimation of the turbulence parameters can be calculated by comparing the results of the algorithm's 0^{th} iteration of the algorithm, where the cross-talk error is not estimated, to those of the subsequent iterations. The evolution of the estimation for the following iterations indicates the convergence of the algorithm and the maximum correction available to our system.

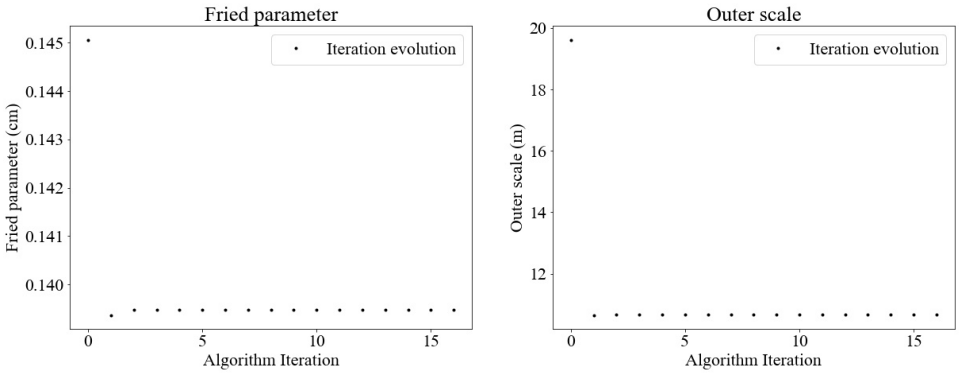

Figure 4.8: Evolution of the turbulence parameters in respect to the algorithm iteration

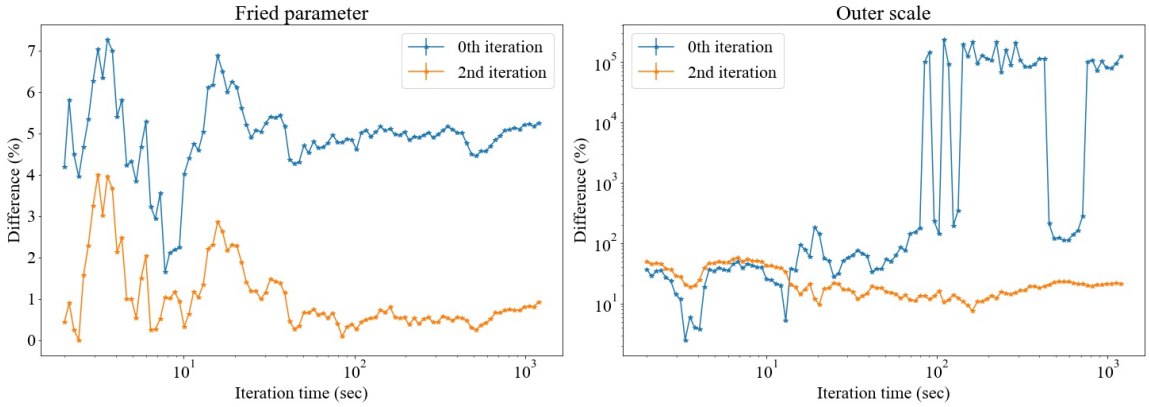

Figure 4.9: Comparison between the 0^{th} iteration and the 2^{nd} iteration.

Figure 4.8 represents the percent difference in the estimation of the turbulence parameters

$$\text{Difference}(\%) = \frac{|r_{0,\text{est}} - r_{0,\text{d}}|}{r_{0,\text{d}}} \tag{4.4}$$

where $r_{0,\text{est}}$ corresponds to the estimation of our algorithm and $r_{0,\text{d}}$ is the value obtained from Section 4.2.1.2. When analysing the outer scale, we substitute the r_0 estimations for $\mathcal{L}_0$ estimations.

We see that the Fried parameter changed from 5% error in the 0^{th} iteration to 0.6% error when compared to the phase screen decomposition. The outer scale error went from 55% to 16%. After the second iteration of the algorithm the values of the turbulence parameters stabilised. This indicates that an estimation of the cross-talk errors is needed in order to obtain sub % errors in the estimation of the Fried parameter.

An analysis of the behaviour of the 0^{th} estimation in time is portrayed in Figure 4.9. High variability in the estimation of the outer scale is seen. The difference of the outer scale to the screen value in a particular time horizon isn't well understood.

The choice of a minimum of two iterations of the algorithm appears correct, as the convergence stops for any higher iteration terms.

4.3.2 Convergence in time

Now we examine the question of time convergence in our data. Small time horizons for the simulation will result in inaccurate estimations. A study of the time of convergence allows us to dictate a minimum volume of data from our telemetry samples.

In this regard the temporal evolution of the Fried parameter,

$$\frac{r_0(t) - r_0(t - \Delta t)}{r_0(t_f)} \tag{4.5}$$

is studied, where $r_0(t)$ represents the Fried parameter at a time horizon, t, and $r_0(t_f)$ represents the final value of the Fried parameter. The time increment Δt is given by the loop frequency of the system, which is set to 500 Hz When the value of this difference becomes small, the temporal evolution of the Fried parameter is assumed to be converging and additional time evolution isn't needed. Figure 4.10 represents the results.

The convergence time coincides with the iteration value of 0.7% of equation (4.5). We present the results in Table 4.3.

The time for convergence in the outer scale is substantially larger than the one for the Fried parameter.

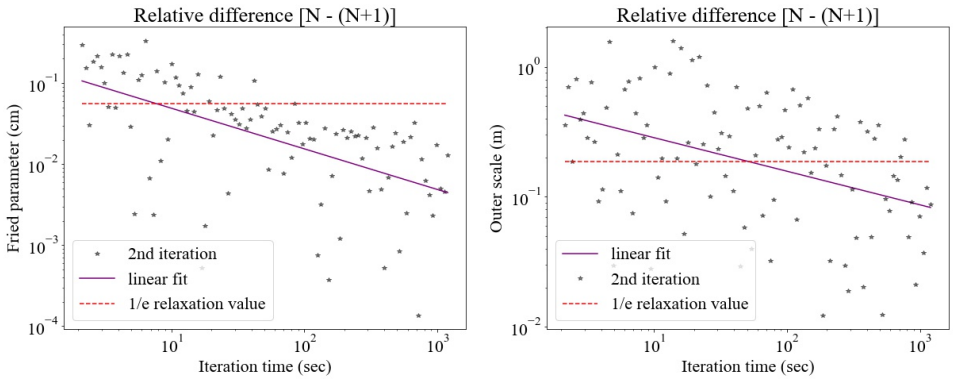

Figure 4.10: Residual evolution of both turbulence parameters.

Table 4.3: Convergence time for the turbulence parameters

Parameter	Convergence Time
Fried parameter	$(37 \pm 5)s$
Outer scale	$(241 \pm 65)s$

4.3.3 Cross-talk and aliasing maximum order

The cross-talk matrix is constructed from the corrected terms, $\mathbf{G_f^+}$, and the higher non-corrected terms, $\mathbf{G_r}$ (equation (3.34)). By letting the $\mathbf{G_r}$ matrix vary in size we are able to control the number of radial orders present. Thus the estimation of turbulence parameters can be made to vary as a function of the maximum radial order of $\mathbf{G_r}$. This behaviour is illustrated in Figure 4.11.

It was observed that low order corrections don't see a difference between the uncorrected and corrected terms, or in other words, the 0^{th} and 2^{nd} iteration are equal. As for the optimal correction term we see a clear stabilisation in the turbulence terms when the radial order crosses 8.

The exact reason for the stabilisation beyond 8 is not yet understood, but we verify it's existence and as such use it as the minimum cross-talk order.

4.3.4 Maximum radial order of the fitting

To validate the contribution of the cross-talk correction we truncate the fitted Zernike coefficients, thus changing the size of the $\mathbf{G_f^+}$ matrix. From the results of Table 4.4 it was determined that the optimal value for the fitting is the available 15 modes of operation, as the inclusion of the cross-talk heavy, 4^{th} radial order, modes is indeed beneficial to our results.

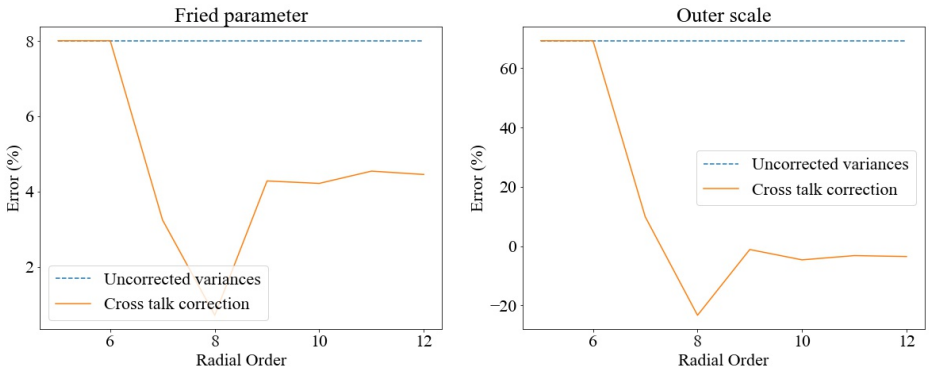

FIGURE 4.11: Turbulence parameters as a function of the cross-talk matrix maximum order.

TABLE 4.4: Fried parameter as a function of the G_f^+ matrix maximum order.

Feature	Max Radial Order	Value	Error
Fried parameter	3	(15.58 ± 0.04) cm	12 %
Fried parameter	4	(13.948 ± 0.003) cm	0.7 %
Outer scale	3	$(11 \times 10^5 \pm 2 \times 10^{12})$m	$9{\times}10^5$ %
Outer scale	4	(10 ± 3) m	11 %

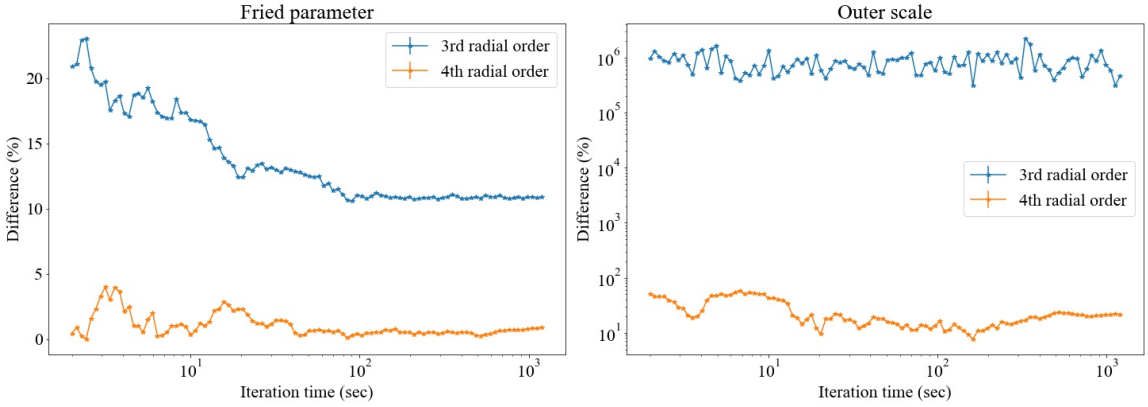

FIGURE 4.12: Comparison of estimations for maximum radial order of 3 and 4.

There was no possibility to increase the fit to further radial orders, as the controlled modes for the NAOMI system stop at 15 and further reconstruction in the real system is not possible.

To probe higher orders we made a simulation using a different SH sensor, this time containing a 8×8 sub-aperture configuration. All other variables stayed fixed, while the time horizon was changed to 200 seconds.

Since the number of lenslets increased from 16 to 64 we can now study increased radial order reconstructions. The maximum order varied from the third to the seventh radial order in this new reconstruction. Figure 4.13 represents the results for the 8×8 sensor AO

telemetry simulation.

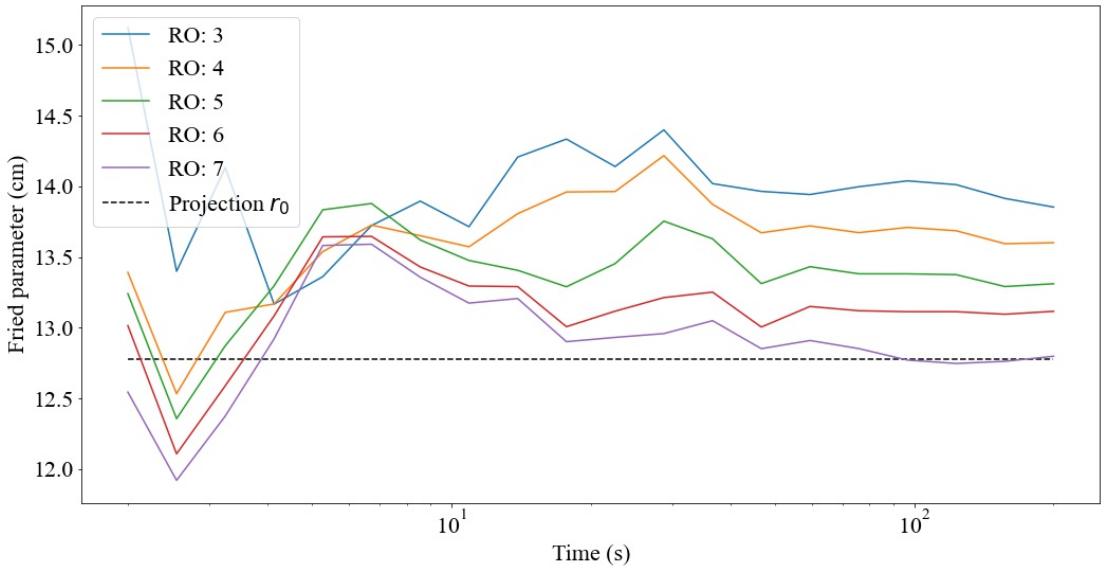

Figure 4.13: Evolution of the seeing estimate with radial order (8x8 sensor).

As the radial order increases the Fried parameter estimation decreases. As such, we expect an underestimation of the seeing when we study the real data from NAOMI. The underestimation ratio for the fourth radial order is 6% when compared to the seventh radial order for an estimation of 3 minutes.

4.3.5 Ideal initial guess

Since the minimisation of the χ^2 is done through the variation of the fitting parameters $\mathbf{p}$ it is important to study the behaviour of the χ^2 surface as a function of the turbulence parameters. A χ^2 surface that possesses multiple minima closely packed is problematic, as the minimisation performed by the algorithm is compromised. Different initial parameters in the minimisation of equation (3.47) can result in a different $\arg\min_{\mathbf{p}}$ depending on the topology of the problem.

In Figures 4.14 and 4.15 we present the χ^2 map of the fitted variances for a night with a seeing of $(0.659 \pm 0.001)''$. In the first Figure the outer scale is a fixed parameter, while in the second both turbulence parameters are allowed to vary. From the first figure it is seen that the topology of the problem has a single minimum. An initial $\mathbf{p}$ with a small value of r_0 is ideal for the algorithm, as the derivative of the χ^2 is larger for small values of the Fried parameter.

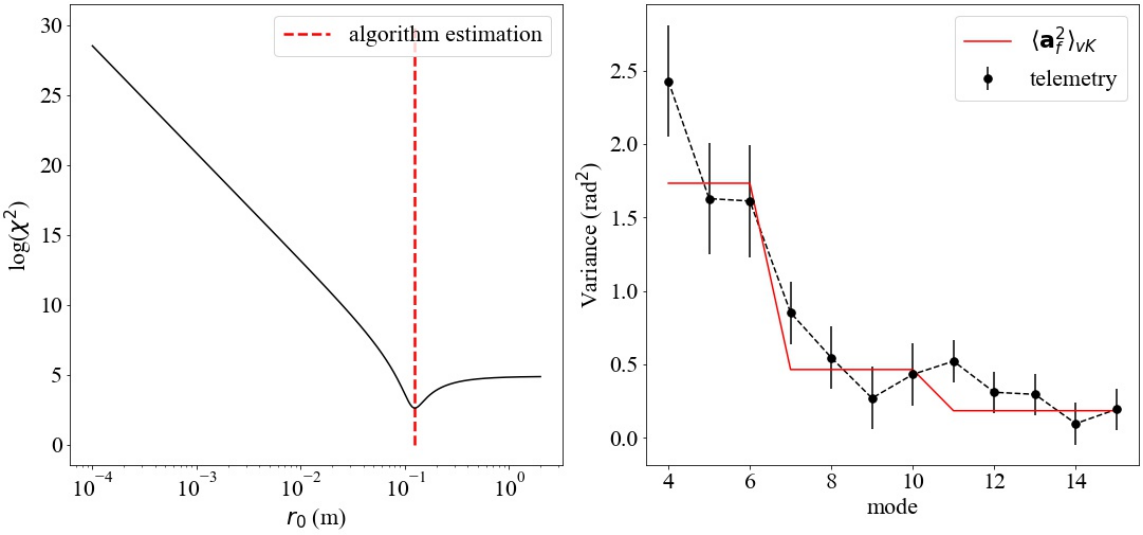

FIGURE 4.14: χ^2 map for the convergence of the Fried parameter. On the left the χ^2 value is analysed as a function of r_0. On the right the fit of the algorithm is presented. A single minima is verified in the curve.

The second figure reinforces the findings of the minimum measurable frequency. Although the same minimum is found on the Fried parameter (horizontal axis) no minimum is found in the outer scale (vertical axis). As such a large error on the estimation of the outer scale is expected of this system.

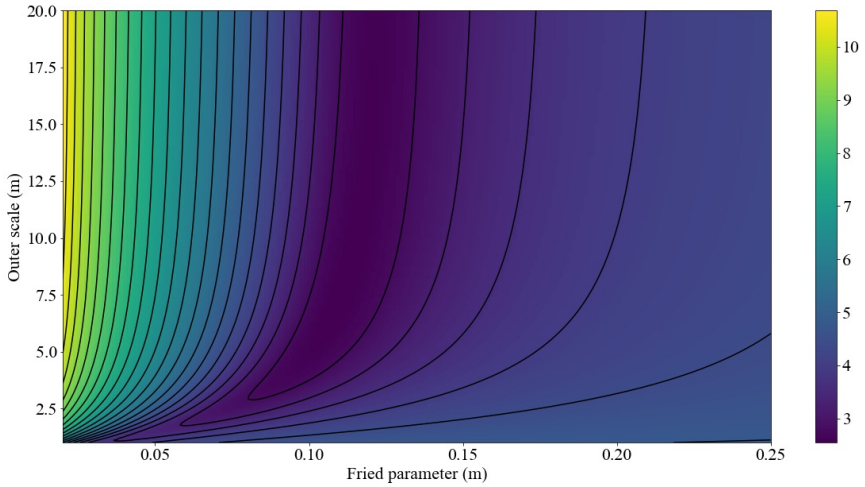

FIGURE 4.15: Map of the convergence of the $\log(\chi^2)$ for the outer scale and Fried parameter.

The data fusion of the four AT data is a future goal that hopes to improve the estimation of the outer scale.

4.3.6 Proposed parameters

We outline the optimised estimation features in Table 4.5.

Table 4.5: Optimised parameters used in the iterative algorithm.

Feature	Value
Maximum radial order of fit	4
Maximum order of remaining error	8
Minimum # of iterations	2
Minimum time horizon	(37 ± 5) s

From the considered parameters we obtain the evolution observed in Figure 4.16. Table 4.6 summarises the values of the estimations. We obtain low errors for the Fried parameter, even with a small time horizon, the outer scale however can't be estimated with accuracy.

Table 4.6: Results of turbulence estimation algorithm

Feature	Time Horizon	Phase screen values	Algorithm estimation	Error
Fried parameter	37 s	(13.87 ± 0.08) cm	(14.1 ± 0.3) cm	1 %
Outer scale	37 s	(12.7 ± 0.8) m	(11 ± 3) m	13 %

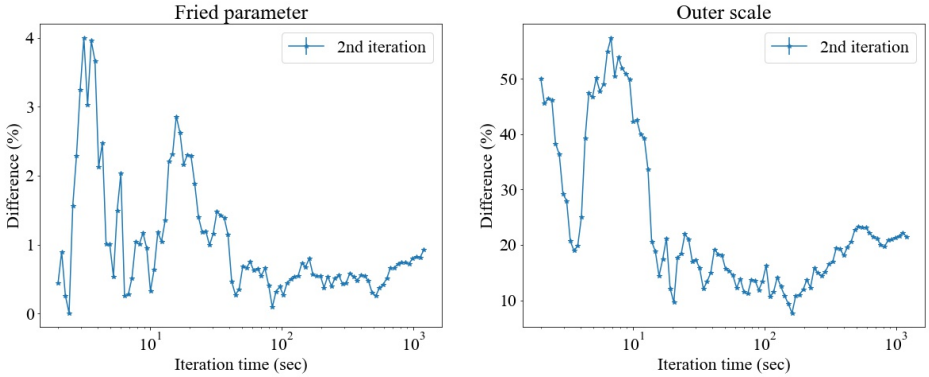

Figure 4.16: Percent difference of Paranal simulation turbulence parameters.

Chapter 5

Processing NAOMI on-sky telemetry

5.1 Data-set curation

Preceding the analysis of the real adaptive optics telemetry data, we seek to curate the data contained in the data sample.

5.1.1 Criteria for the selection of data

5.1.1.1 Loop frequency

The primary loop frequency of the NAOMI system is 500 Hz. 100 Hz and 50 Hz integration is only activated for samples with R magnitudes greater than 8 and as such result in a low Strehl ratio (always below 40% as can be seen in Figure 5.1). The Strehl ratio is useful to assess the quality of the image formation, varying from 100%-0%, where high Strehl ratios correspond to better quality. We opted to exclude such samples from our data, maintaining the frequency to 500Hz and avoiding low Strehl ratio samples. 92.44% of our data operates in such a loop frequency.

5.1.2 Time horizon of the observation

The duration of the data for samples with 500 Hz loop frequency is illustrated in Figure 5.2. Most samples have a shorter duration than the minimum time horizon of (37 ± 5) s, with 61% having a duration of 20 seconds.

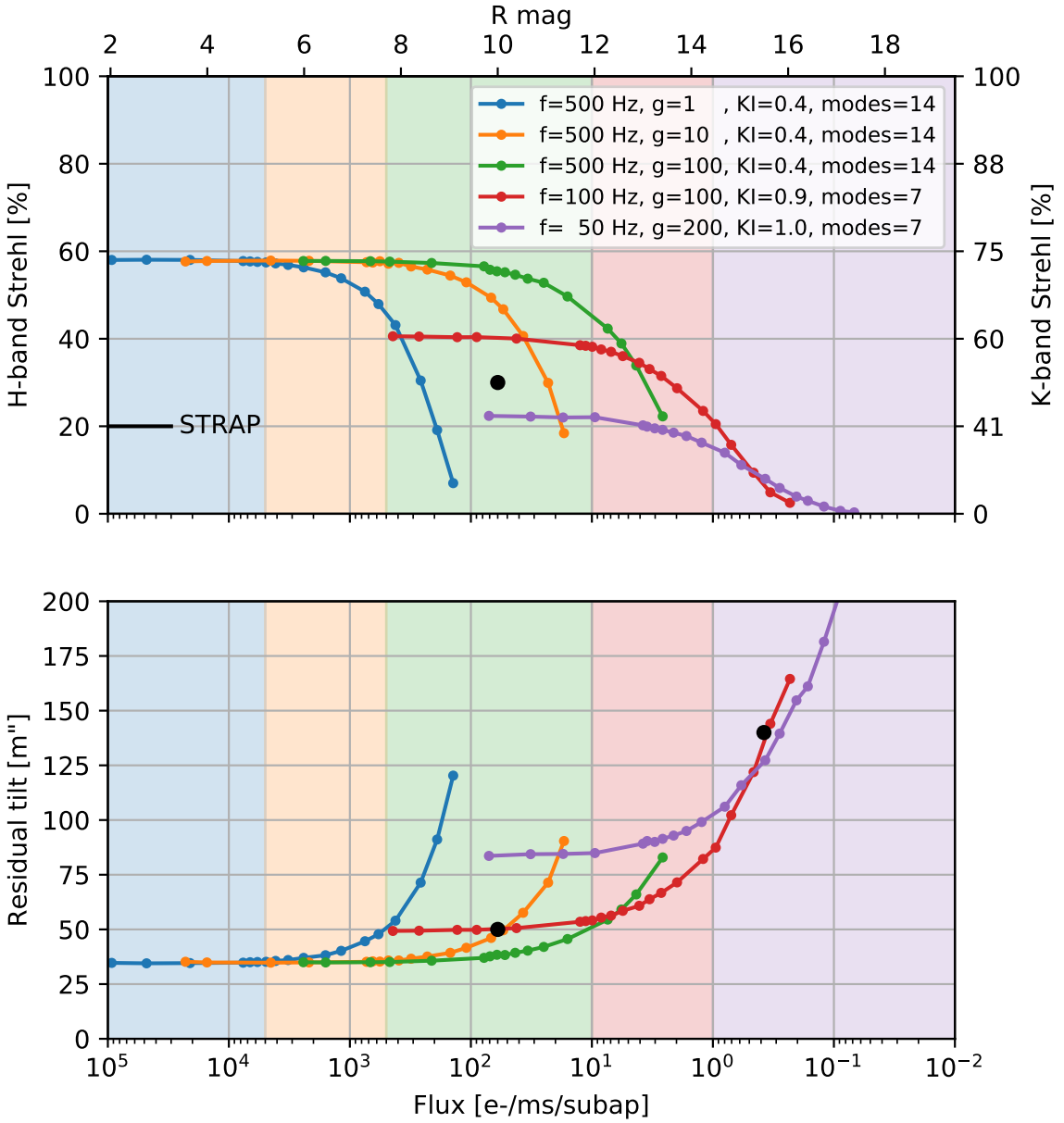

FIGURE 5.1: NAOMI response to loop frequency, extracted from Woillez et al. (2019).

According to the results of Section 4.3.6 the estimated time horizon corresponds to a 1% error in the estimation of the Fried parameter. The same analysis at a 20 seconds time horizon wields a 2% error. Taking into account the large amount of data available below the previously estimated time horizon we decide to include any sample with 20 seconds or longer into our selected data.

5.1.3 Sensor data

The Auxiliary Telescopes track the same target on-sky, as such up to four telemetry data samples can be generated for the same observation. This permits multiple estimations

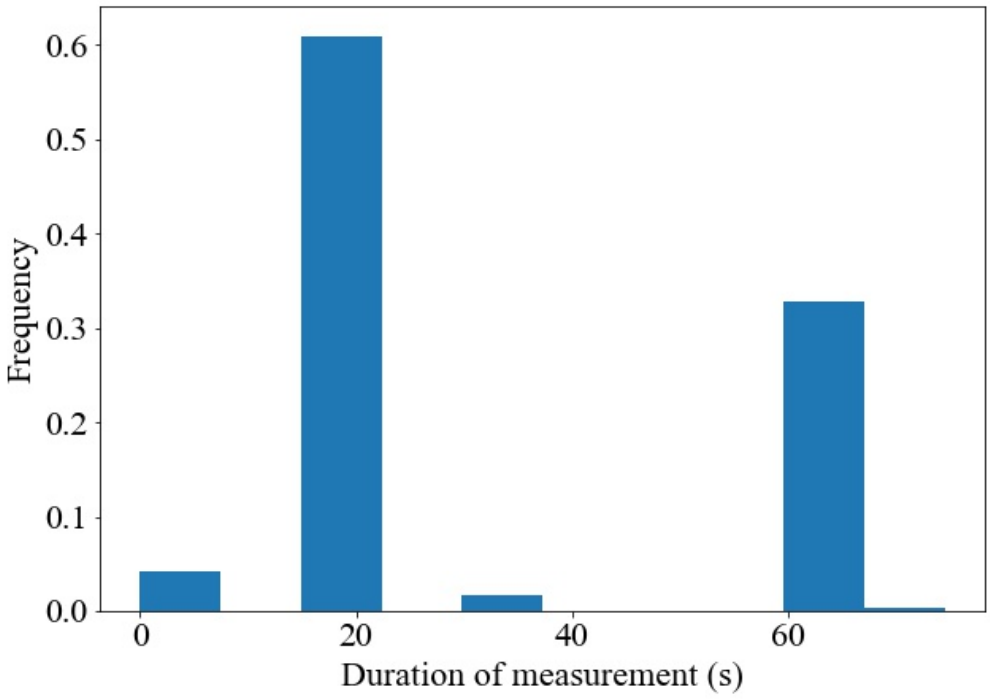

Figure 5.2: Distribution of observation duration at 500 Hz loop frequency.

of the same atmospheric conditions at the same time. The internal consistency of these results acts as validation tool of our algorithm.

Figure 5.3 represents the overlapping data in any given observation. Four data samples aren't always generated, with 25% of the observations containing at least two telemetry data samples.

5.1.4 Zenith distance

The zenith angle is available in the telemetry data. It is studied in Figure 5.4. The zenith distance allows the calculation of the air mass of the observation. A larger zenith distance results in an increase in the amount of atmosphere the light crosses before arriving at the measurement system. The reference values of the DIMM are given at zenith, therefore the data needs to be normalised.

5.1.5 Curated data

The curated data used in the estimations is then summarised in Table 5.1.

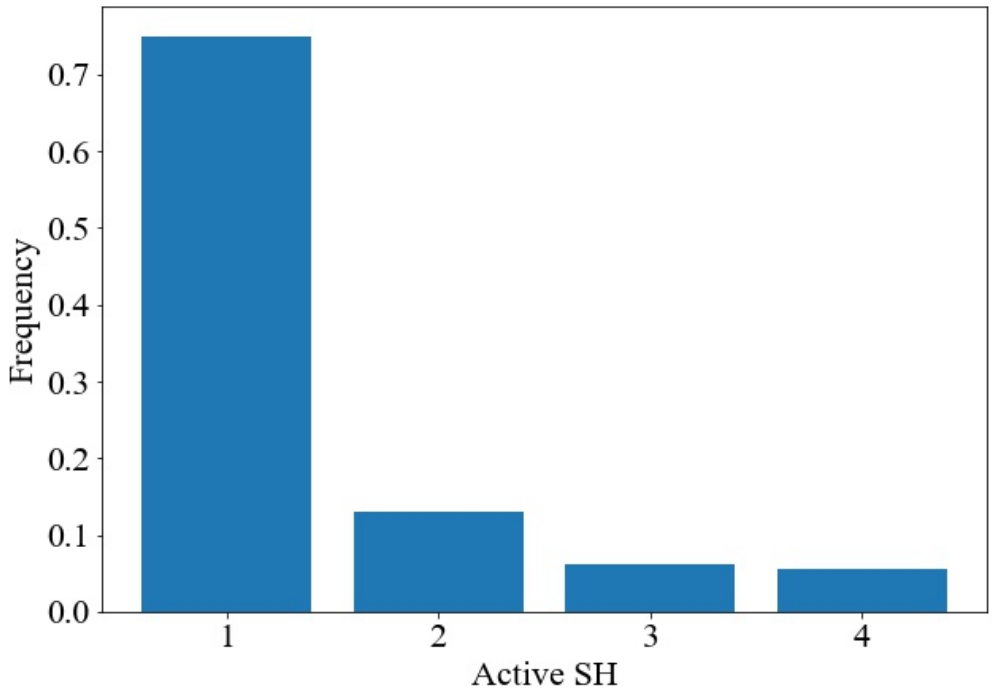

FIGURE 5.3: Number of overlapping data in any given observation for 20 seconds duration data with 500 Hz loop frequency.

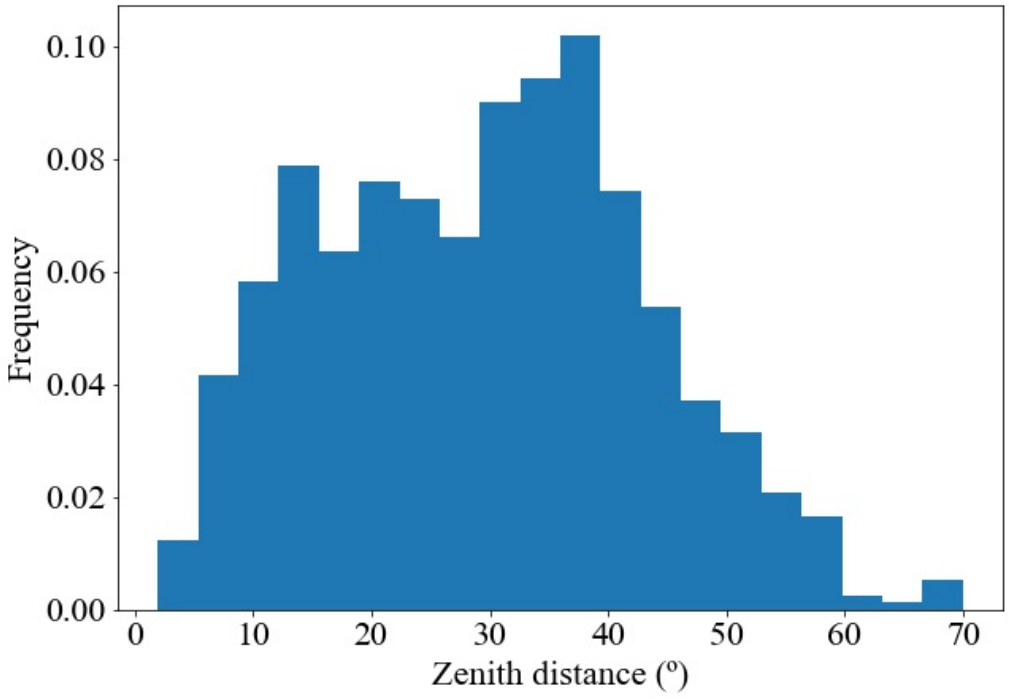

FIGURE 5.4: Zenith distance of measurements for the overlapping data.

Table 5.1: Features of the NAOMI telemetry data

Feature	Value
# of measurements	36932
500Hz loop frequency	92.44 %
Open/Closed Loop data	[10.02, 89.98] %
Data distribution	2018/11 - 2020/12
# of sensors	4
20 seconds of data	88.50 %

5.2 Real data analysis

The chosen data is now introduced into our algorithm allowing for the reconstruction of the seeing from the generated telemetry data.

5.2.1 Normalisation of the zenith angle

The zenith angle was normalised to coincide with the DIMM data. The theoretical relationship of the seeing with the altitude is $\cos(\gamma)^{3/5}$ in equation (2.8), where γ represents the altitude (90^{o} - zenith angle). This relation is presented in red in Figure 5.5.

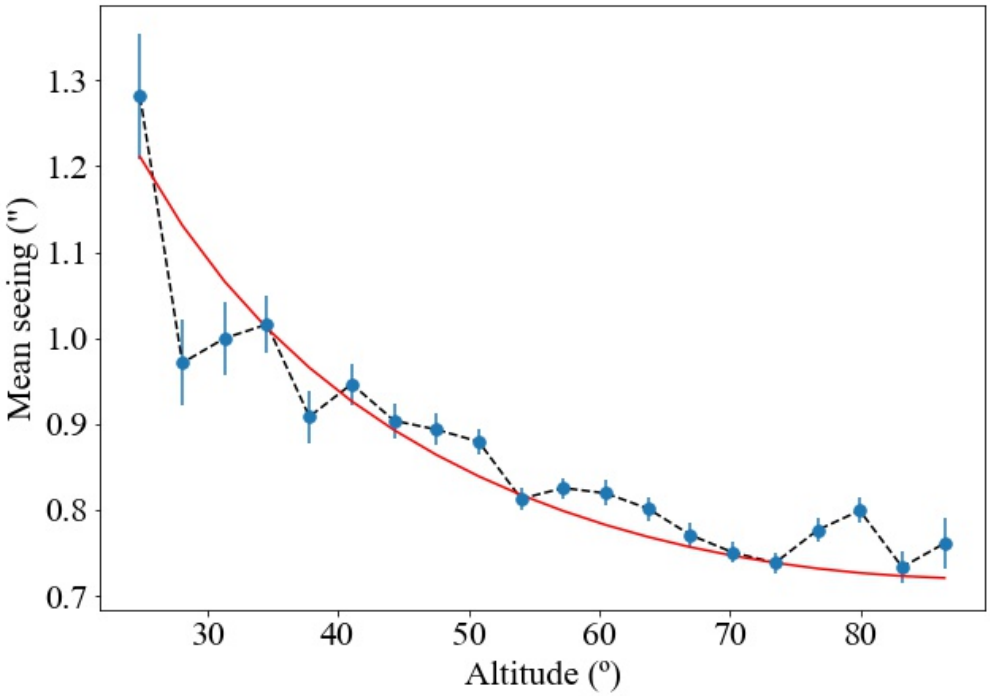

Figure 5.5: Distribution of the seeing across different observation angles.

The trend is well represented in our data. When the angle of observation is very small a deviation from the trend is observed.

5.2.2 Estimation of the seeing

The results for the initial telemetry data estimations are presented in Figure 5.6. The median seeing of the data-set is 0.665″, while 47 data points estimated a seeing smaller than 0.1″.

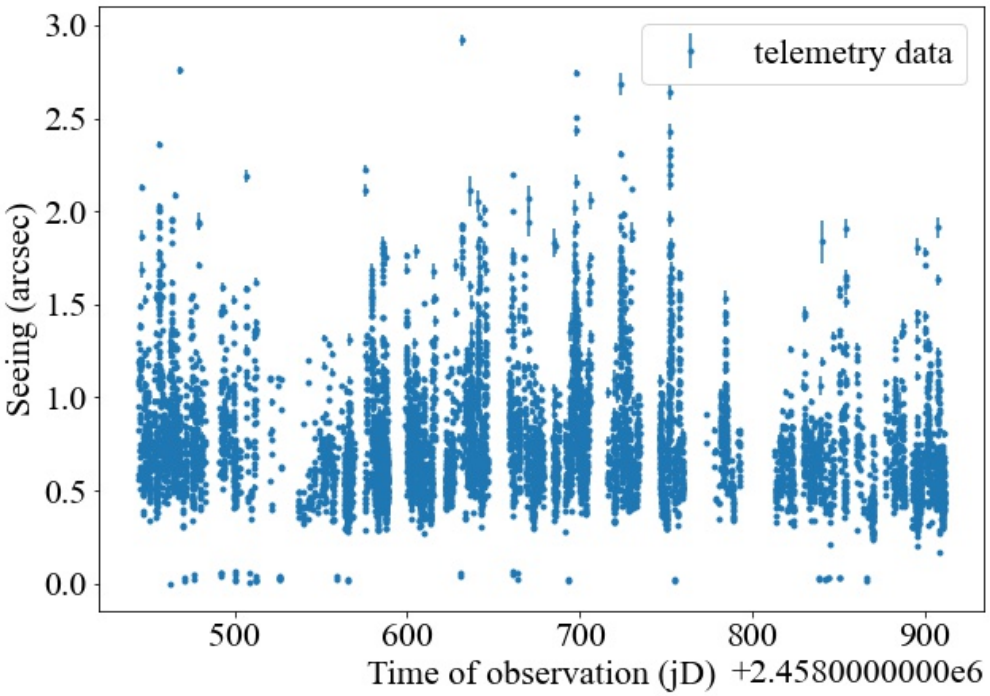

FIGURE 5.6: Estimation of the seeing for the telemetry data.

5.2.2.1 Uncertainty in the fit

Before discussing any further, an estimation of the uncertainty is necessary. The uncertainty of the seeing can be directly obtained from the Fried parameter estimation, since the seeing, α, is a function of the r_0 (Fried, 1965)

$$\alpha = 0.976\frac{\lambda}{r_0}, \tag{5.1}$$

since we assume all other quantities to be true values, we can use the uncertainty of the Fried parameter, $u(r_0)$, to calculate the uncertainty of the seeing, $u(\alpha)$. Error propagation analysis shows that

$$u(\alpha) = \frac{\alpha}{r_0} u(r_0), \tag{5.2}$$

where the uncertainty of the Fried parameter is obtained from the error of the mean as described in Section 3.4.

The percent uncertainty of the algorithm estimation is presented in Figure 5.7. The median uncertainty is 1.2%.

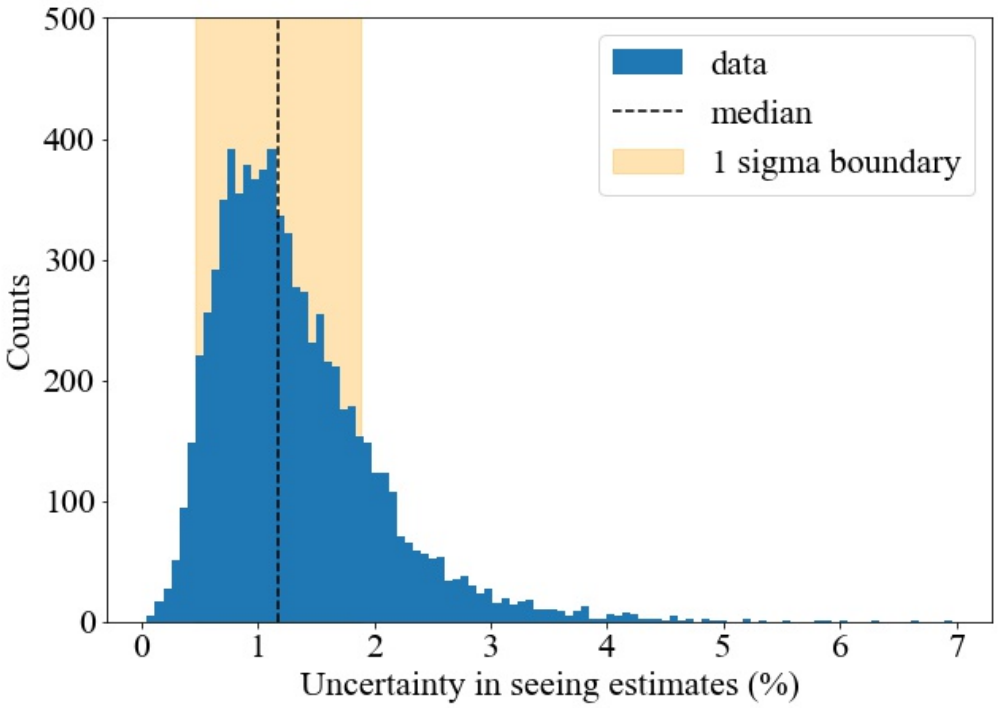

Figure 5.7: Distribution of the uncertainty estimates as a percentage of the seeing estimate. The uncertainty is obtained from the Monte Carlo approach described in section 3.4.

5.2.2.2 Seeing outliers

An analysis of the variance is done to tackle the low seeing outliers. The variances and convergence for one of the outliers is presented in Figure 5.8. An abnormally large variance was found in the fourth Noll mode. The Fried parameter didn't converge for the initial telemetry sample.

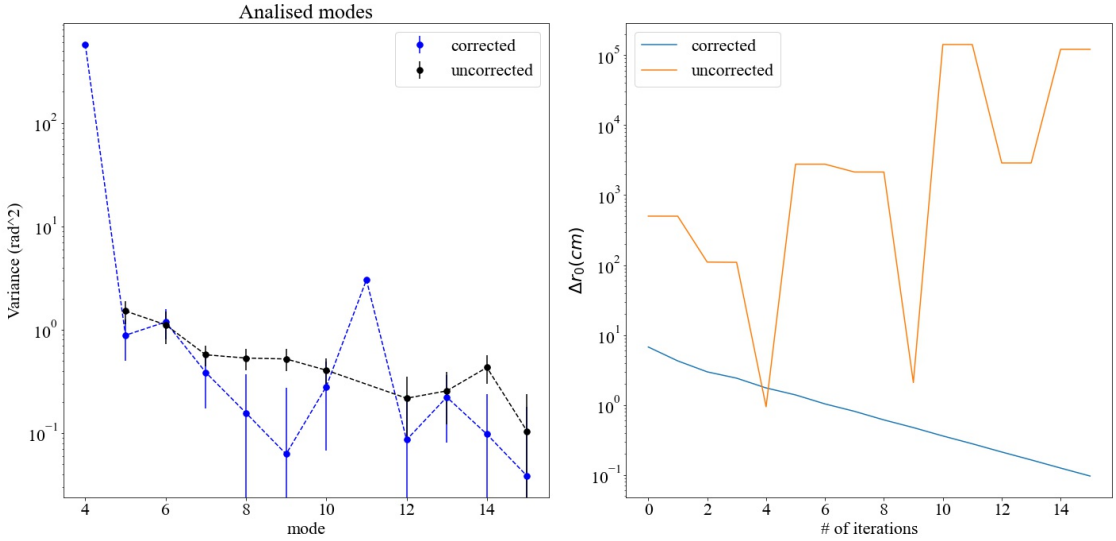

FIGURE 5.8: Variance for one of the outlier nights (left). Convergence with iteration (right).

The defocus mode corresponds to the fourth Noll mode. This mode is still affected in a large part by the wind-shake and vibrations of the telescope (Fusco et al. (2004)). These types of contributions aren't seen in the simulation. Future fitting of the variances should avoid including this mode if possible.

A total removal of the defocus is not ideal for NAOMI. We only have 15 available modes for the fit. Its default removal would result in a loss of 7% of the fitted modes. The choice should be made in a case by case basis, by removing abnormally high variances from the fit.

Once the bad points are removed from the fit a correct estimation for the seeing was obtained, with values converging slower than the previously seen data (15 iterations were performed in this study of the convergence). The convergence was studying the difference, Δr_0,

$$\Delta r_0 = r_{0,\mathrm{i}+1} - r_{0,\mathrm{i}}, \tag{5.3}$$

which is given by the change of the Fried parameter across an iteration of the algorithm, $r_{0,\mathrm{i}}$.

The algorithm fits a von Kármán model. If the variances aren't representative of the model the fit will suffer in quality and in the number of iterations needed for a convergence.

This difference can be caused by sporadic problems in the performance of the AO system. As is seen in the former example. It can also be caused by an incorrect estimation

of the noise. The noise was estimated as a fitting parameter of the algorithm, as is seen in the fitting equation presented in Section 3.4.

It can also be estimated through the auto-correlation of the signal in time (Fusco et al. (2004)). This was done for a small subset of data (5 data points taken at random from the total data-set). A comparison of the two noise estimations allows the evaluation of the quality of the estimation of noise. The results are presented in Figure 5.9.

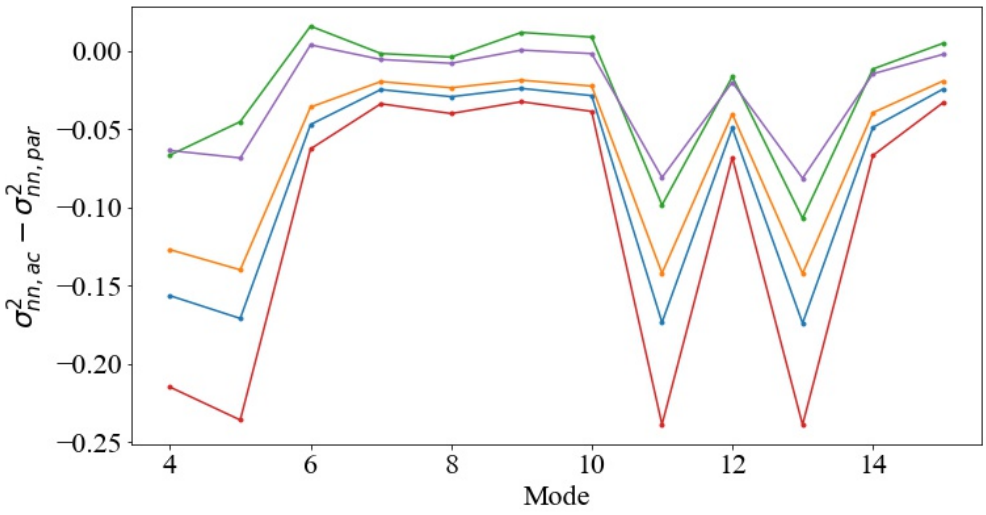

Figure 5.9: Comparison between noise measured using temporal auto-correlation, $\sigma^2_{nn,ac}$, and the one estimated by the algorithm, $\sigma^2_{nn,par}$. 5 different nights are presented. The noise estimated by the algorithm seems biased in the 4^{th}, 5^{th}, 11^{th},13^{th} Noll modes. The reason is not yet understood.

A difference between the two was found. The difference between the two algorithm estimations increased significantly for the 4^{th}, 5^{th}, 11^{th} and 13^{th} Noll modes. A larger study is needed to assess the cause and prevalence of this disparity.

The temporal auto correlation method for the estimation of the measurement noise wasn't implemented in the full sample due to time constraints. Future work will see the implementation of this method in our algorithm.

We can study the effects of this difference on the seeing for our sub-sample. Figure 5.10 represents the difference in seeing, α, estimated from the two systems of estimation of error

$$\Delta\alpha = \alpha_{\mathrm{ac}} - \alpha_{\mathrm{par}}, \tag{5.4}$$

where α_{ac} is the seeing estimate using the noise from temporal auto-correlation and α_{par} is the seeing resulting from our algorithm.

For the points studied the seeing of the auto-correlation is larger than the one estimated by the algorithm. The convergence with the number of iterations is similar (Figure 5.11). Due to the small sample size we can't make statistical claims of the results. A larger study must be performed to study the differences.

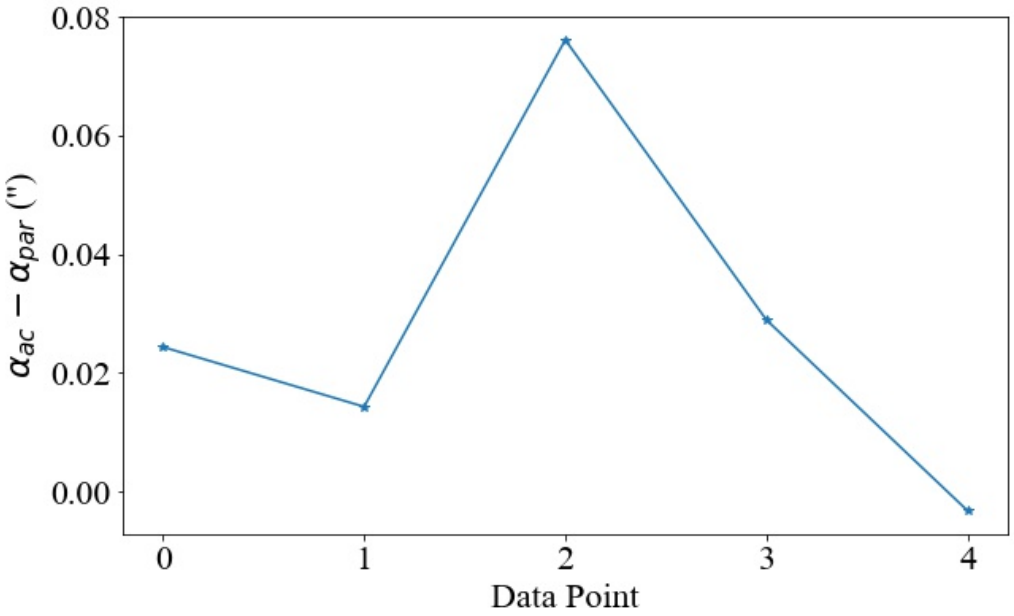

FIGURE 5.10: Difference between seeing estimates of the auto-correlation method and noise as a parameter of the fit.

Following this discussion, the outlier points with abnormal defocus variance are now removed from the sample.

5.2.3 Comparison with the DIMM

A comparison between the DIMM and telemetry data is now performed. Figure 5.12 represents the relationship between the two estimates. For each telemetry data point we compare it to the DIMM estimate available in the header. The colour-bar represents the density of points.

The correlation between the two data-sets is 0.71. The fitted linear relationship (with a fixed value of 0 at the origin) between the two sets of data is (0.8765 ± 0.0001) telemetry units per DIMM units.

The difference seen in the estimates is partially explained by the behaviour of the simulated values in Figure 4.13. The Fried parameter was shown to vary 6% between a fitting using 15 modes and one using 36 modes, with a larger Fried parameter being

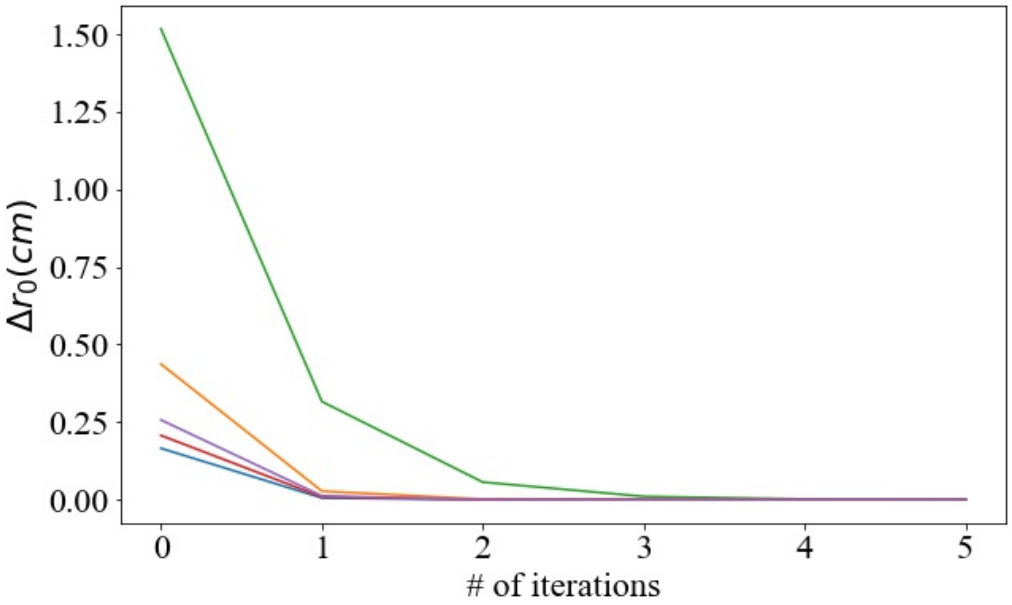

Figure 5.11: Convergence of the Fried parameter for the estimation of the noise through auto-correlation. Each line represents the algorithm convergence for a single data sample.

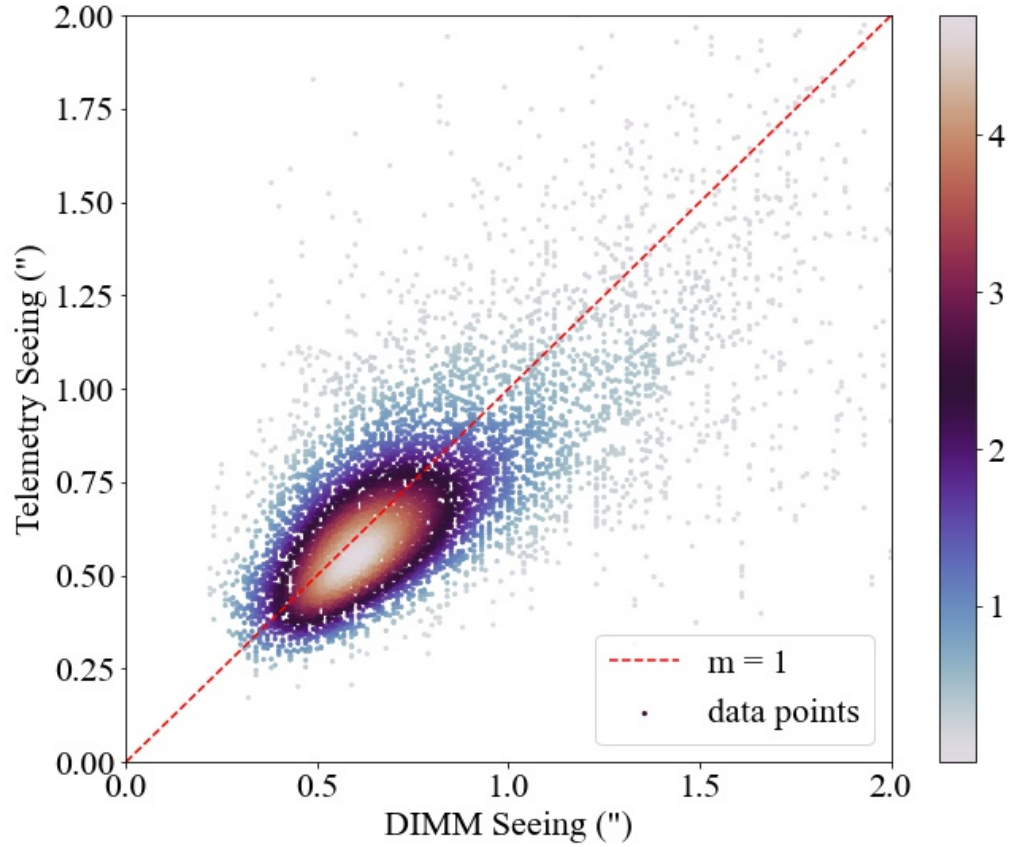

Figure 5.12: Comparison of results between DIMM and telemetry seeing estimates.

estimated for low orders. Since the seeing is inversely proportional to the Fried parameter we then expect an underestimation of the seeing for low orders of correction. This alone can't explain the 29% difference seen in the correlation.

The smaller seeing can be caused by the estimation of the noise. This approach was explored in section 5.2.2.2.

It can also be caused by the presence of the defocus mode. Since the defocus mode is still strongly affected by the wind-shake of the telescope we analyse the seeing estimates in relation to the wind-speed. Figure 5.13 represents the seeing for various brackets of wind-speed. When the wind-speed increases the difference between the estimates also increases. As shown in section 5.2.2.2 it is caused by the increase in variance of the defocus mode, via wind excitation of telescope vibrations.

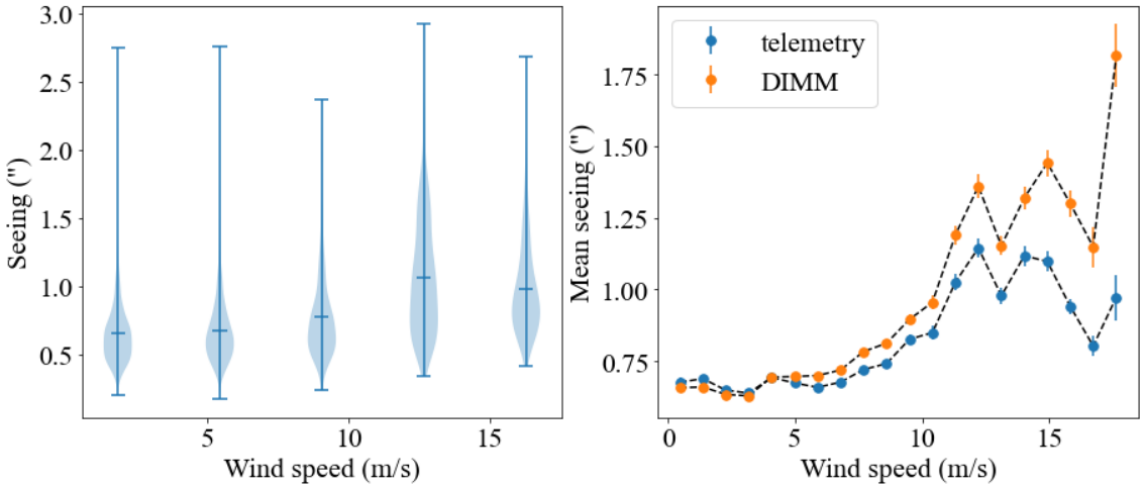

FIGURE 5.13: Distribution of the seeing across different wind speeds.

An analysis of the dispersion of results also agrees with the results of the wind-speed. The distributions of the results for the DIMM and telemetry estimates are presented in Figure 5.14. Each violin plot represents the distribution of the seeing in the particular estimate with the blue lines representing the median of each distribution.

The DIMM seeing has a larger maximum seeing. This is seen in Figure 5.13, where the telemetry fits smaller seeings when the velocity is larger.

5.2.4 The outer scale

An analysis of the outer scale estimates is now performed. It was seen in the simulation of the system that the outer scale couldn't be well estimated, even for 20 minutes time

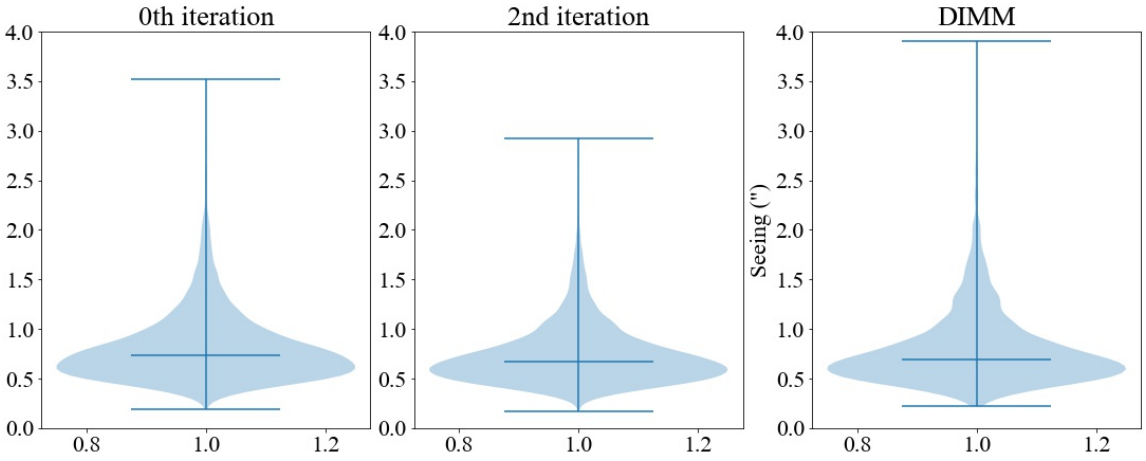

Figure 5.14: Violin plot of the seeing estimates for the DIMM, 2^{nd} and 0^{th} iteration of the algorithm.

horizon. This is also the case in the real data estimations, but to a much larger degree (Figure 5.15).

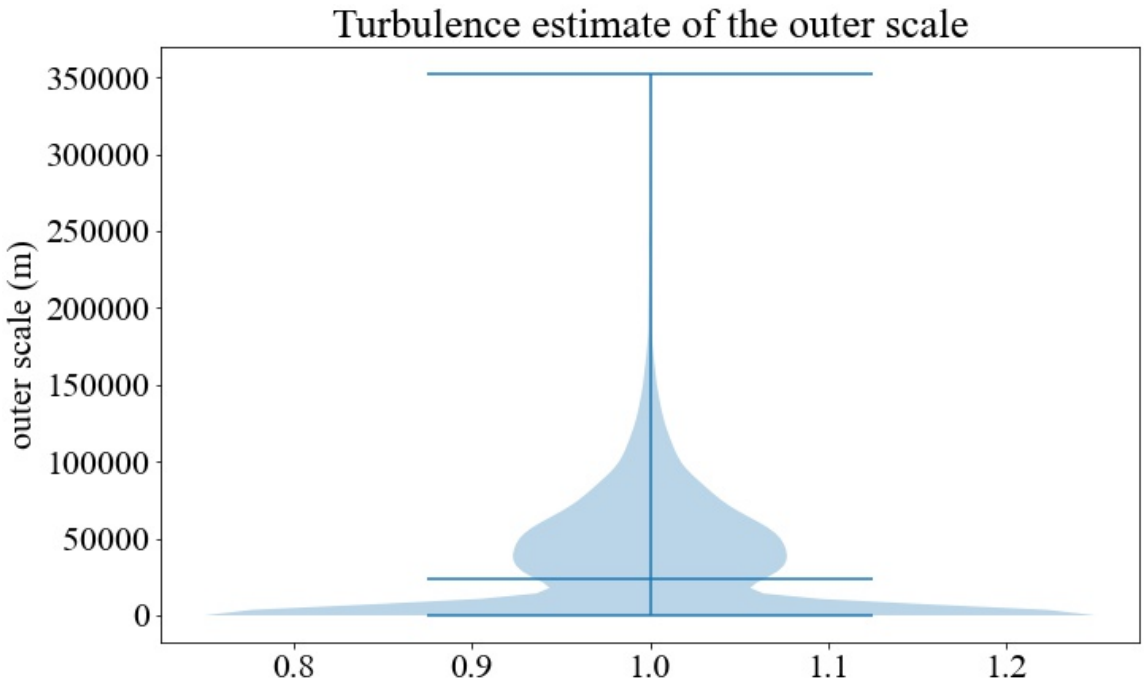

Figure 5.15: Distribution of the outer scale in the turbulence estimation.

The results of the outer scale are significantly different from the ones assessed by the simulation. It was shown in Andrade et al. (2019) that the SNR ratio affects the estimates. The simulation assumed no noise. This partially answers the disparity seen between results.

5.2.5 Agreement between AT's

The NAOMI system is installed in the four auxiliary telescopes. This allows the monitoring of the same star from different positions in the mountain. The individual performance of the NAOMI system can be obtained by analysing the agreement of the various AT's turbulence parameter estimations. This is done through the subtraction of the seeing measurements (Figure 5.16 and Table 5.2). We attain agreement between all 6 combinations of telemetry data, this is reinforced between the numerical results of the table 5.2, with all seeing differences being inserted in the matching regime, $\mu = 0$. The uncertainty of the measurement is given by the uncertainty of the mean.

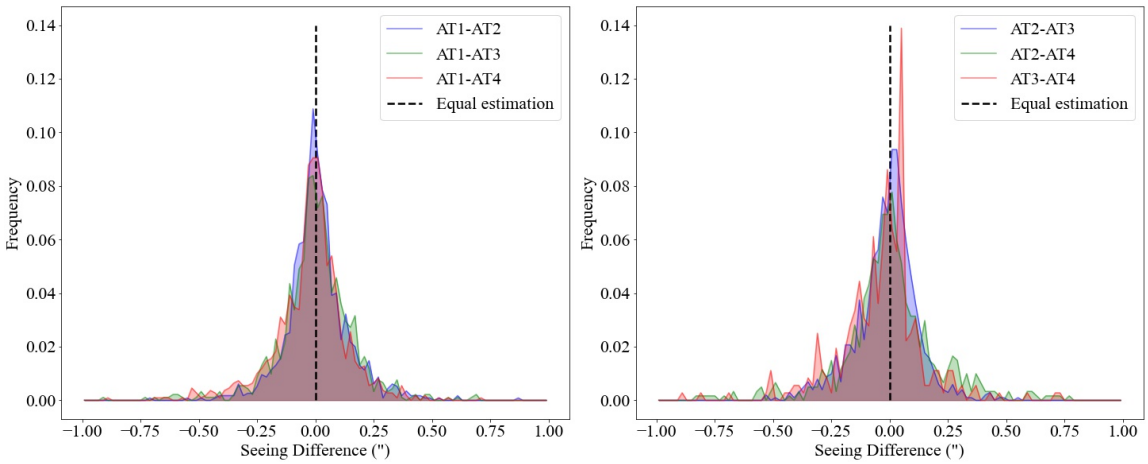

FIGURE 5.16: Comparison between SH estimates.

Data	Mean
$AT_1 - AT_2$	$(0.011 \pm 0.004)''$
$AT_1 - AT_3$	$(-0.000 \pm 0.006)''$
$AT_1 - AT_4$	$(-0.020 \pm 0.006)''$
$AT_2 - AT_3$	$(-0.013 \pm 0.004)''$
$AT_2 - AT_4$	$(0.010 \pm 0.005)''$
$AT_3 - AT_4$	$(-0.012 \pm 0.004)''$

TABLE 5.2: Comparison of AT's

The results for the ATs give us information on the behaviour of the seeing parameter across the observatory. By comparing the position of each AT in an observational run a transverse profile of the seeing across the mountain can be developed. The initial results of the comparison seems to indicate that the seeing doesn't vary significantly across the ATs. An additional study of the precise location of the ATs as a function of the seeing is needed.

Chapter 6

Conclusions and future recommendations

This dissertation aimed to answer a main question: Can a low order (4×4) Shack-Hartmann wavefront sensor estimate the turbulence parameters: Fried and outer scale?

To answer this question an iterative estimation algorithm was first validated on simulated data and then applied on telemetry data produced from the operation of the adaptive optics system of the Auxiliary Telescopes of the VLT, NAOMI.

The estimation algorithm was optimised using a simulation of the NAOMI system. Simulation results show the ideal number of iterations, minimum time horizon and number of modes to be included in the fitted variances and remaining error estimation. The χ^2 map of the algorithm was shown to converge to the expected value without bias and through its analysis the ideal initial guess for our algorithm was established. On the other hand the aliasing and cross-talk errors were shown to be mixed for any radial order above the fifth.

The correction of cross-talk, noise and aliasing was shown to be necessary for the correct estimation of the Fried parameter. The uncorrected variances were shown to incorrectly estimate the Fried parameter, with an error of 5%. By compensating the remaining error we were able to achieve sub-per cent accuracy in the estimation of the parameter.

The outer scale couldn't be estimated correctly, as the minimum spacial frequency detectable by the sensor was larger than the one associated with the outer scale, rendering the sensor and our algorithm insensitive to this parameter.

Following optimisation, the algorithm was applied to real on-sky data, which was curated to remove undesirable samples. The uncertainty of the estimation of the seeing was first assessed. A median uncertainty of 1.2% was found.

Tip and tilt modes weren't included in the estimation due to telescope vibrations. The defocus mode was included in the fit but it's still largely affected by telescope vibrations and was found to problematic in the fit, creating outliers in the variances. Bias in the estimation of the noise was shown to affect the estimation. A comparison with noise estimation obtained from temporal auto-correlation found that our algorithm produced smaller seeing estimates. This method wasn't applied to the full data-set due to time constraints.

Our algorithm was compared to the DIMM seeing estimates, which served as a reference. Disagreement between the two was found, with a correlation of 0.71 being found between the two estimates. Our algorithm estimated $(12.35 \pm 0.04)\,\%$ smaller seeing conditions.

Comparison of the seeing estimates between the four available telescopes showed consistency in our estimates. On average all telescopes estimated the same seeing conditions for the same observation, within the measurement uncertainty of $0.005''$. A rigorous analysis of the spacial distribution of the seeing wasn't possible. Finally we found seasonality in the seeing, with the seeing conditions worsening during Winter months, were the median seeing was $0.703''$, while the Summer months provided the best seeing conditions, with a median seeing of $0.584''$.

6.1 Future recommendations

The dissertation showed that the noise was order dependent and that therefore the iterative algorithm error estimate is limited. An ongoing work is the use of the auto-correlation method for error estimation, this approach has the advantages of a better error estimate and of a smaller number of fit parameters.

Further to the DIMM, a comparison with SLODAR and SCIDAR data would be an interesting next development. It would allow to better understand the seeing estimate differences between DIMM and our algorithm.

It was also shown that the Fried parameter can be estimated from a low order Shack-Hartmann system in 1.8 m diameter telescope but not the outer scale. The next immediate step is to apply the algorithm to a higher order system in a larger diameter telescope. An ideal test-bed is the CIAO system of the VLTI. This system samples the four 8 m telescope pupils with four 9×9 wavefront sensors. The larger telescope diameter implies a larger sensitivity to the outer scale. On the other hand the higher order system translates in less contamination of lower orders (more sensitive to the outer scale) by aliasing and cross-talk.

Finally, the simultaneous combination of the four Shack-Hartmann sensors at the ATs should be explored to estimate the outer scale. The larger spatial baseline of the ATs is both an advantage ("sampling" larger spatial scales) and a disadvantage, due to loss of correlation effects.

Appendix A

Function Definitions

The covariance of the coefficients, $\langle a_j a^*_{j'}(\mathbf{s})\rangle$, can be computed using:

$$\langle a_j a^*_{j'}(\mathbf{s})\rangle = 2^{14/3}\pi^{8/3}AR^{5/3}[(n+1)(n'+1)]^{1/2} \times f_{jj'}(s,\theta_0,k_0) \tag{A.1}$$

Here the parameters s, θ_0 and k_0 represent the radial and angular polar coordinates, the wave vector at which the function is evaluated and the function $f_{jj'}$ is given by:

$$f_{jj'}(s,\theta_0,k_0) = \begin{cases} \pm(-1)^{(n+n'-m-m')/2}\cos{(m+m')\theta_0} I_{m+m',n+1,n'+1}(2s,2\pi Rk_0) & m,m' \neq 0; \\ +(-1)^{(n+n'+2m+|m+m'|)/2}\cos{(m-m')\theta_0} I_{|m+m'|,n+1,n'+1}(2s,2\pi Rk_0) & -: j,j' \text{ are both odd}; \\ (-1)^{(n+n'-m-m')/2}\sin{(m+m')\theta_0} I_{m+m',n+1,n'+1}(2s,2\pi Rk_0) & +: j,j' \text{ are both even}; \\ -(-1)^{(n+n'+2m+|m-m'|)/2}\sin{(m-m')\theta_0} I_{|m-m'|,n+1,n'+1}(2s,2\pi Rk_0) & m,m' \neq 0;\ j \text{ even},j' \text{ odd}; \\ (-1)^{(n+n'-m)/2}\sqrt{2}\cos{(m\theta_0)} I_{m,n+1,n'+1}(2s,2\pi Rk_0) & m' = 0; j \text{ even}; \\ (-1)^{(n+n'-m)/2}\sqrt{2}\sin{(m\theta_0)} I_{m,n+1,n'+1}(2s,2\pi Rk_0) & m' = 0; j \text{ odd}; \\ (-1)^{(n+n')/2} I_0(2s,2\pi Rk_0) & m = m' = 0; \end{cases} \tag{A.2}$$

In which the integral term is given by:

$$I(\kappa,\mu,\nu,\rho,\lambda;a,x_0) = \frac{\left(\frac{a}{2}\right)^{\kappa}\Gamma\left(\frac{\mu+\nu+1}{2}\right)\Gamma\left(\frac{\mu+\nu}{2}+1\right)}{2\sqrt{2}\Gamma(\mu+\nu+1)\Gamma(\nu+1)\Gamma(\mu+1)\Gamma(\lambda+1)}$$
$$\times\Big[\sum_{m=0}^{\infty}\frac{(-1)^m\Gamma\left(\lambda+1-\frac{\kappa+\mu+\nu+\rho}{2}-m\right)\Gamma\left(\frac{\kappa+\mu+\nu+\rho}{2}+m\right))}{m!\Gamma(\kappa+m+1)}\left(\frac{a}{2}\right)^{2m} x_0^{\kappa+\mu+\nu+\rho-2\lambda-2+2m}$$
$$\times\,{}_4F_3\left(-m,-\kappa-m,\frac{\mu+\nu+1}{2},\frac{\mu+\nu}{2}+1;\mu+\nu+1,\mu+\nu+1;\frac{4}{a^2}\right)\Big]$$
$$+\sum_{m=0}^{\infty}\frac{(-1)^m\Gamma\left(-\lambda-1+\frac{\kappa+\mu+\nu+\rho}{2}-m\right)\Gamma\left(\lambda+m+1\right))}{m!\Gamma\left(\lambda+2+\frac{\kappa-\mu-\nu-\rho}{2}+m\right)}\left(\frac{a}{2}\right)^{2\lambda+2-\kappa-\mu-\nu-\rho+2m} x_0^{2m}$$
$$\times\,{}_4F_3\left(\lambda-1+\frac{\kappa+\mu+\nu+\rho}{2}-m,-\lambda-m,\frac{\mu+\nu+1}{2},\frac{\mu+\nu}{2}+1;\mu+1,\nu+1,\mu+\nu+1;\frac{4}{a^2}\right) \tag{A.3}$$

Here we define the generalised hypergeometric function, ${}_pF_q$:

$${}_pF_q\left[\begin{array}{cc}(a); & z\\ (b) & \end{array}\right] = \sum_{k=0}^{\infty}\prod_{n=1}^{p}\frac{(a_n)_k}{(b_m)_k}\frac{z_k}{k!} \tag{A.4}$$

Where we define the (a) and (b) through the Pochhammer series:

$$(a_n)_k = \frac{\Gamma(a_n+k)}{\Gamma(a_n)} \tag{A.5}$$

Here $\Gamma(x)$ represents the error function:

$$\Gamma(x) = \int_0^{\infty} x^{\alpha-1}\exp -x dx \tag{A.6}$$

Bibliography

Piezoelectric deformable mirrors. URL https://www.thorlabs.com/newgrouppage9.cfm?objectgroup_id=5056. [Cited on page 23.]

Paulo P. Andrade, Paulo J.V. Garcia, Carlos M. Correia, Johann Kolb, and Maria Inês Carvalho. Estimation of atmospheric turbulence parameters from shack-hartmann wavefront sensor measurements. *Monthly Notices of the Royal Astronomical Society*, 483: 1192–1201, 2 2019. ISSN 13652966. doi: 10.1093/mnras/sty3181. [Cited on pages 3, 6, 24, 36, and 69.]

François Assémat, Richard Wilson, and Eric Gendron. Method for simulating infinitely long and non stationary phase screens with optimized memory storage. *Optics Express*, 14(3):988–999, February 2006. doi: 10.1364/OE.14.000988. [Cited on page 43.]

Remy Avila. Theoretical properties of the autocovariance of wavefront curvature induced by atmospheric turbulence and their potential for $C_n^{\ 2}$ profiling. , 507(1):L11–L15, October 2021. doi: 10.1093/mnrasl/slab080. [Cited on page 6.]

Philip R. Bevington and D. Keith Robinson. *Data reduction and error analysis for the physical sciences*. 2003. [Cited on pages 38 and 39.]

T. Butterley, R. W. Wilson, M. Sarazin, C. M. Dubbeldam, J. Osborn, and P. Clark. Characterization of the ground layer of turbulence at Paranal using a robotic SLODAR system. , 492(1):934–949, February 2020. doi: 10.1093/mnras/stz3498. [Cited on pages 18 and 19.]

Jean-Marc Conan, Gérard Rousset, and Pierre-Yves Madec. Wave-front temporal spectra in high-resolution imaging through turbulence. *Journal of the Optical Society of America A*, 12:1559, 7 1995. ISSN 1084-7529. doi: 10.1364/JOSAA.12.001559. [Cited on pages 34 and 46.]

Richard Davies and Markus Kasper. Adaptive Optics for Astronomy. , 50:305–351, September 2012. doi: 10.1146/annurev-astro-081811-125447. [Cited on page 21.]

Niek Doelman. The minimum of the time-delay wavefront error in adaptive optics. , 491 (4):4719–4723, February 2020. doi: 10.1093/mnras/stz3237. [Cited on page 6.]

Dainis Dravins, Lennart Lindegren, Eva Mezey, and Andrew T. Young. Atmospheric Intensity Scintillation of Stars, I. Statistical Distributions and Temporal Properties. , 109:173–207, February 1997. doi: 10.1086/133872. [Cited on page 13.]

O. J. D. Farley, J. Osborn, T. Morris, T. Fusco, B. Neichel, C. Correia, and R. W. Wilson. Limitations imposed by optical turbulence profile structure and evolution on tomographic reconstruction for the ELT. , 494(2):2773–2784, May 2020. doi: 10.1093/mnras/staa795. [Cited on page 19.]

Romain J. L. Fétick, Benoit Neichel, Laurent M. Mugnier, Aurélie Montmerle-Bonnefois, and Thierry Fusco. Turbulent and adaptive optics corrected point-spread functions as convolutive orders of the phase power spectral density. , 481(4):5210–5215, December 2018. doi: 10.1093/mnras/sty2595. [Cited on page 6.]

D. L. Fried. Statistics of a geometric representation of wavefront distortion. *JOSA, Vol. 55, Issue 11, pp. 1427-1435*, 55:1427–1435, 11 1965. ISSN 0030-3941. doi: 10.1364/JOSA.55.001427. URL https://opg.optica.org/viewmedia.cfm?uri=josa-55-11-1427&seq=0&html=truehttps://opg.optica.org/abstract.cfm?uri=josa-55-11-1427https://opg.optica.org/josa/abstract.cfm?uri=josa-55-11-1427. [Cited on pages 7, 8, and 62.]

T. Fusco, G. Rousset, D. Rabaud, E. Gendron, D. Mouillet, F. Lacombe, G. Zins, P. Y. Madec, A. M. Lagrange, J. Charton, D. Rouan, N. Hubin, and N. Ageorges. Naos on-line characterization of turbulence parameters and adaptive optics performance. *Journal of Optics A: Pure and Applied Optics*, 6:585–596, 6 2004. ISSN 14644258. doi: 10.1088/1464-4258/6/6/014. [Cited on pages 24, 64, and 65.]

A. Guesalaga, B. Neichel, C. M. Correia, T. Butterley, J. Osborn, E. Masciadri, T. Fusco, and J. F. Sauvage. Online estimation of the wavefront outer scale profile from adaptive optics telemetry. *Monthly Notices of the Royal Astronomical Society*, 465:1984–1994, 2 2017. ISSN 13652966. doi: 10.1093/MNRAS/STW2548. [Cited on page 24.]

A. Guesalaga, B. Ayancán, M. Sarazin, R. W. Wilson, S. Perera, and M. Le Louarn. FASS: a turbulence profiler based on a fast, low-noise camera. , 501(2):3030–3045, February 2021. doi: 10.1093/mnras/staa3823. [Cited on page 15.]

Jan Herrmann. Cross coupling and aliasing in modal wave-front estimation. *Journal of the Optical Society of America*, 71:989–992, 1981. ISSN 00303941. doi: 10.1364/JOSA.71.000989. [Cited on page 34.]

Paul Hickson, Lu Feng, Joschua A. Hellemeier, Zhixia Shen, Suijian Xue, Yongqiang Yao, Bin Ma, Hualin Chen, and Rui Yang. Optical turbulence at Ali, China - results from the first year of lunar scintillometer observations. , 494(4):5992–6000, June 2020. doi: 10.1093/mnras/staa1101. [Cited on page 16.]

Laurent Jolissaint, Sam Ragland, Julian Christou, and Peter Wizinowich. Determination of the optical turbulence parameters from the adaptive optics telemetry: critical analysis and on-sky validation. *Applied Optics*, 57:7837, 9 2018. ISSN 1559-128X. doi: 10.1364/AO.57.007837. [Cited on page 24.]

A. N. Kolmogorov. The Local Structure of Turbulence in Incompressible Viscous Fluid for Very Large Reynolds Numbers. *Proceedings of the Royal Society of London Series A*, 434(1890):9–13, July 1941. doi: 10.1098/rspa.1991.0075. [Cited on page 6.]

V. Kornilov, A. Tokovinin, N. Shatsky, O. Voziakova, S. Potanin, and B. Safonov. Combined MASS-DIMM instruments for atmospheric turbulence studies. , 382(343):1268–1278, December 2007. doi: 10.1111/j.1365-2966.2007.12467.x. [Cited on page 14.]

Douglas J. Laidlaw, James Osborn, Timothy J. Morris, Alastair G. Basden, Eric Gendron, Gérard Rousset, Matthew J. Townson, and Richard W. Wilson. Automated wind velocity profiling from adaptive optics telemetry. , 491(1):1287–1294, January 2020. doi: 10.1093/mnras/stz3062. [Cited on page 19.]

CG Little. A diffraction theory of the scintillation of stars on optical and radio wavelengths. *Monthly Notices of the Royal Astronomical Society*, 111(3):289–302, 1951. [Cited on page 13.]

Li-Yong Liu, Yong-Qiang Yao, Jia Yin, Hong-Shuai Wang, Jun-Rong Li, Yun-He Zhou, Xian-Long You, Peng Tang, Xi-Yu Zhao, De-Qiang Ma, and Jian Dong. Site testing campaign for the Large Optical Telescope at the Ali site. *Research in Astronomy and Astrophysics*, 20(6):084, June 2020. doi: 10.1088/1674-4527/20/6/84. [Cited on page 13.]

Ryan Lyman, Tiziana Cherubini, and Steven Businger. Forecasting seeing for the Maunakea Observatories. , 496(4):4734–4748, August 2020. doi: 10.1093/mnras/staa1787. [Cited on page 14.]

F Martin, R Conan, A Tokovinin, A Ziad, H Trinquet, J Borgnino, A Agabi, and M Sarazin. Optical parameters relevant for high angular resolution at paranal from gsm instrument and surface layer contribution. *Astronomy and Astrophysics Supplement Series*, 144(1): 39–44, 2000. [Cited on page 10.]

P. Martinez, J. Kolb, A. Tokovinin, and M. Sarazin. Atmospheric image blur with finite outer scale or partial adaptive correction. *Astronomy and Astrophysics*, 516, 2010. ISSN 14320746. doi: 10.1051/0004-6361/201014413. [Cited on page 7.]

E. Masciadri, F. Lascaux, and L. Fini. MOSE: operational forecast of the optical turbulence and atmospheric parameters at European Southern Observatory ground-based sites - I. Overview and vertical stratification of atmospheric parameters at 0-20 km. , 436(3): 1968–1985, December 2013. doi: 10.1093/mnras/stt1708. [Cited on pages xi and 44.]

E. Masciadri, G. Lombardi, and F. Lascaux. On the comparison between MASS and generalized-SCIDAR techniques. , 438(2):983–1004, February 2014. doi: 10.1093/mnras/stt2194. [Cited on page 13.]

Ian S. McLean. Electronic imaging in astronomy. *Electronic Imaging in Astronomy*, 2008. doi: 10.1007/978-3-540-76583-7. [Cited on page 35.]

Guang ming Dai. Modal wave-front reconstruction with zernike polynomials and karhunen–loève functions. *Journal of the Optical Society of America A*, 13:1218, 6 1996. ISSN 1084-7529. doi: 10.1364/JOSAA.13.001218. [Cited on pages 22, 27, and 32.]

Hajime Ogane, Masayuki Akiyama, Shin Oya, and Yoshito Ono. Atmospheric turbulence profiling with multi-aperture scintillation of a Shack-Hartmann sensor. , 503(4):5778–5788, June 2021. doi: 10.1093/mnras/stab105. [Cited on page 14.]

Yoshito H. Ono, Carlos M. Correia, Dave R. Andersen, Olivier Lardière, Shin Oya, Masayuki Akiyama, Kate Jackson, and Colin Bradley. Statistics of turbulence parameters at maunakea using the multiple wavefront sensor data of raven. *Monthly Notices of the Royal Astronomical Society*, 465:4931–4941, 3 2017. ISSN 13652966. doi: 10.1093/MNRAS/STW3083. [Cited on pages 19 and 24.]

J. Osborn, T. Butterley, M. J. Townson, A. P. Reeves, T. J. Morris, and R. W. Wilson. Turbulence velocity profiling for high sensitivity and vertical-resolution atmospheric characterization with Stereo-SCIDAR. , 464(4):3998–4007, February 2017. doi: 10.1093/mnras/stw2685. [Cited on page 16.]

J. Osborn, R. W. Wilson, M. Sarazin, T. Butterley, A. Chacón, F. Derie, O. J. D. Farley, X. Haubois, D. Laidlaw, M. LeLouarn, E. Masciadri, J. Milli, J. Navarrete, and M. J. Townson. Optical turbulence profiling with Stereo-SCIDAR for VLT and ELT. , 478(1): 825–834, July 2018. doi: 10.1093/mnras/sty1070. [Cited on pages xi, 9, and 20.]

Chun Qing, Tao Luo, Cuicui Bi, Xuebin Li, Shengcheng Cui, Qike Yang, Changdong Su, Su Wu, Xianmei Qian, Xiaoqing Wu, and Wenyue Zhu. Optical turbulence and wind speed distributions above the Tibetan Plateau from balloon-borne microthermal measurements. , 508(3):4096–4105, December 2021. doi: 10.1093/mnras/stab2608. [Cited on page 15.]

Roberto Ragazzoni. Pupil plane wavefront sensing with an oscillating prism. *Journal of Modern Optics*, 43(2):289–293, February 1996. doi: 10.1080/09500349608232742. [Cited on page 21.]

F. Roddier. The effects of atmospheric turbulence in optical astronomy. *Progess in Optics*, 19:281–376, January 1981. doi: 10.1016/S0079-6638(08)70204-X. [Cited on page 14.]

F. (Francois) Roddier. *Adaptive optics in astronomy*. Cambridge University Press, 1999. ISBN 052155375X. [Cited on pages 13, 22, 23, and 25.]

William D Rogatto, Joseph S Accetta, and David L Shumaker. The infrared & electro-optical systems handbook. electro-optical components, volume 3. Technical report, INFRARED INFORMATION AND ANALYSIS CENTER ANN ARBOR MI, 1993. [Cited on page 15.]

A E Roy and D Clarke. Radio telescopes bt - astronomy: Principles and practice. *Astronomy: Principles and Practice*, 1977. URL https://books.google.com/books/about/Astronomy.html?id=v2S6XV8dsIAC. [Cited on page 13.]

Matthias Schöck, David Le Mignant, Gary A. Chanan, Peter L. Wizinowich, and Marcos A. van Dam. Atmospheric turbulence characterization with the keck adaptive optics systems i open-loop data. *Applied Optics*, 42:3705, 7 2003. ISSN 0003-6935. doi: 10.1364/AO.42.003705. [Cited on page 24.]

EJ Seykora. Solar scintillation and the monitoring of solar seeing. *Solar Physics*, 145(2): 389–397, 1993. [Cited on page 16.]

H. W. Shepherd, J. Osborn, R. W. Wilson, T. Butterley, R. Avila, V. S. Dhillon, and T. J. Morris. Stereo-SCIDAR: optical turbulence profiling with high sensitivity using a modified SCIDAR instrument. , 437(4):3568–3577, February 2014. doi: 10.1093/mnras/stt2150. [Cited on page 19.]

European Southern, Observatory Headquarters, Garching Karl-Schwarzschild-Straße, Dario Dorigo, Alberto Micol Eso, Julio Navarrete, Marc Sarazin, Ignacio Vera, Sequeiros Eso, and Myha Vuong. *European Organisation for Astronomical Research in the Southern Hemisphere Programme: PIP Astronomical Site Monitor Data User Manual Change Record from previous Version Astronomical Site Monitor Data User Manual*. 2015. URL www.eso.org. [Cited on page 13.]

Avinash Surendran, Padmakar S. Parihar, Ravinder K. Banyal, and Anusha Kalyaan. Development of a Lunar Scintillometer as part of the national large optical telescope site survey. *Experimental Astronomy*, 45(1):57–79, March 2018. doi: 10.1007/s10686-017-9567-9. [Cited on page 16.]

Naruhisa Takato and Ichirou Yamaguchi. Spatial correlation of zernike phase-expansion coefficients for atmospheric turbulence with finite outer scale. *Journal of the Optical Society of America A*, 12:958, 5 1995. ISSN 1084-7529. doi: 10.1364/JOSAA.12.000958. [Cited on pages 27 and 37.]

Yusufjon Tillayev, Azimjon Azimov, and Aktam Hafizov. Astronomical Seeing at Maidanak Observatory during the Year 2018. *Galaxies*, 9(2):38, May 2021. doi: 10.3390/galaxies9020038. [Cited on page 13.]

A. Tokovinin. From differential image motion to seeing. *Publications of the Astronomical Society of the Pacific*, 114:1156–1166, 10 2002. ISSN 0004-6280. doi: 10.1086/342683/XML. URL https://iopscience.iop.org/article/10.1086/342683https://iopscience.iop.org/article/10.1086/342683/meta. [Cited on pages xi, 12, 13, and 28.]

A. Tokovinin. Turbulence profiles from the scintillation of Stars, Planets, and Moon. In *Revista Mexicana de Astronomia y Astrofisica Conference Series*, volume 31 of *Revista*

Mexicana de Astronomia y Astrofisica Conference Series, pages 61–70, October 2007. [Cited on page 14.]

A. Tokovinin, J. Vernin, A. Ziad, and M. Chun. Optical Turbulence Profiles at Mauna Kea Measured by MASS and SCIDAR. , 117(830):395–400, April 2005. doi: 10.1086/428930. [Cited on page 19.]

A. Tokovinin, M. Sarazin, and A. Smette. Testing turbulence model at metric scales with mid-infrared visir images at the vlt. *Monthly Notices of the Royal Astronomical Society*, 378:701–708, 2007. ISSN 13652966. doi: 10.1111/J.1365-2966.2007.11803.X. [Cited on page 6.]

A. Tokovinin, E. Bustos, and A. Berdja. Near-ground turbulence profiles from lunar scintillometer. , 404(3):1186–1196, May 2010. doi: 10.1111/j.1365-2966.2010.16367.x. [Cited on pages 16 and 17.]

V. V. Voitsekhovich. Outer scale of turbulence: comparison of different models. *Journal of the Optical Society of America A*, 12:1346, 6 1995. ISSN 1084-7529. doi: 10.1364/JOSAA.12.001346. [Cited on pages 11 and 13.]

J. Woillez, J. A. Abad, R. Abuter, E. Aller Carpentier, J. Alonso, L. Andolfato, P. Barriga, J. P. Berger, J. L. Beuzit, H. Bonnet, G. Bourdarot, P. Bourget, R. Brast, L. Caniguante, E. Cottalorda, P. Darré, B. Delabre, A. Delboulbé, F. Delplancke-Ströbele, R. Dembet, R. Donaldson, R. Dorn, J. Dupeyron, C. Dupuy, S. Egner, F. Eisenhauer, G. Fischer, C. Frank, E. Fuenteseca, P. Gitton, F. Gonté, T. Guerlet, S. Guieu, P. Gutierrez, P. Haguenauer, A. Haimerl, X. Haubois, C. Heritier, S. Huber, N. Hubin, P. Jolley, L. Jocou, J. P. Kirchbauer, J. Kolb, J. Kosmalski, P. Krempl, J. B. Le Bouquin, M. Le Louarn, P. Lilley, B. Lopez, Y. Magnard, S. McLay, A. Meilland, A. Meister, A. Merand, T. Moulin, L. Pasquini, J. Paufique, I. Percheron, L. Pettazzi, O. Pfuhl, D. Phan, W. Pirani, J. Quentin, A. Rakich, R. Ridings, M. Riedel, J. Reyes, S. Rochat, G. Santos Tomás, C. Schmid, N. Schuhler, P. Shchekaturov, M. Seidel, C. Soenke, E. Stadler, C. Stephan, M. Suárez, M. Todorovic, G. Valdes, C. Verinaud, G. Zins, and S. Zúñiga-Fernández. Naomi: the adaptive optics system of the auxiliary telescopes of the vlti. *Astronomy Astrophysics*, 629:A41, 9 2019. ISSN 0004-6361. doi: 10.1051/0004-6361/201935890. URL https://www.aanda.org/articles/aa/full_html/2019/09/aa35890-19/aa35890-19.htmlhttps:

//www.aanda.org/articles/aa/abs/2019/09/aa35890-19/aa35890-19.html. [Cited on pages xii, 28, 42, and 58.]